SURFACE STRAIN EFFECT ON ELECTRONIC MODULATIONS OF LOW–DIMENSIONAL TRANSITION METAL CHALCOGENIDES AND TRANSITION METAL

CHAN CHEUK HEI

PhD

The Hong Kong Polytechnic University

2025

The Hong Kong Polytechnic University

Department of Applied Biology and Chemical Technology

Surface Strain Effect on Electronic Modulations of Low-dimensional Transition Metal Chalcogenides and Transition Metal

Chan Cheuk Hei

A thesis submitted in partial fulfilment of the requirements for the degree Doctor of Philosophy

August 2025

Certificate of originality

I hereby declare that this thesis is my own work and that, to the best of my knowledge and belief, it reproduces no material previously published or written, nor material that has been accepted for the award of any other degree or diploma, except where due acknowledgement has been made in the text.

_____ (Signed)

Chan Cheuk Hei (Name of student)

Abstract

The low–dimensional materials, such as transition metal (TM), transition metal chalcogenide (TMC), and graphene, are important in different fields of science and studies. These semiconducting materials generally possess specific properties different from bulk materials, such as the appropriate thickness of band gap, strong spin–orbit coupling, and semiconducting characteristics. For the transition metal, the high stability, specific d–state, and synergistic effect are the symbolic properties. Benefitting from the specific properties, these materials are commonly used as components of catalysis, energy storage, new types of energy, and different industrial processes. However, some disadvantages limit the development of these materials, including safety issues, environmental friendliness, high cost, and low efficiency. To overcome the obstacles, scientists invented various methods to improve the performance of these materials. Among various methods, strain engineering is a relatively common and high–efficiency strategy to change the properties of materials. Strain engineering induces strain to the targeted materials, and then deforms the geometry of the material, which enables scientists to tune the properties of low–dimensional materials.

For the TMC, MoS_2 and $MoSe_2$ are chosen as the samples, whereas Pt and Pd are chosen as the samples of TM. These samples are common materials to intensively apply in the fields of catalysis, new types of energy supply, and storage. The studies provide valuable data as a reference for understanding the strain and ripple effect and then guide the development of the next stage. The program, Atomsk, is used to modify geometry and simulate the strain as well as the ripple on the samples. The software, BIOVIA Materials Studio (MS), is applied to validate the modification of the model from

Atomsk, and then perform the DFT calculations by the program, CASTEP.

Through the DFT calculations, the total energies after geometry optimization, single–point energies, work functions (WF), density of states (DOS), band gaps, and the band structures are calculated and analyzed. The calculated data demonstrate the instability of the models under the strain and ripple effect. The strain and ripple effect significantly change the interatomic distance, bond angle, and orbital overlapping of the models. The structural change brings the property modification of each model and then enhances the electronic performance. The ripple effect is more effective than the simple strain effect to tune the properties of TM and TMC. However, the trend of the property change reflects the difficulty in controlling the ripple effect. In contrast, the strain effect can tune the properties of TMC and TM under a relatively stable condition.

The calculated results provide valuable information to investigate the strain and ripple effects of the TM and TMC. The data can be applied as a reference for future work, which reduces the time and resource consumption of further studies. These results will assist in deciding the direction of future work and further development of these materials toward varying applications.

Keywords

Ripple effect, Strain effect, Transition metal, Transition metal chalcogenide, property modification, low–dimensional material

Abbreviations

Low dimension	LD
1–dimension	1D
2–dimension	2D
3–dimension	3D
Transition metal	TM
Transition metal chalcogenide	TMC
Transition metal dichalcogenide	TMD
Density Functional Theory	DFT
Material Studio	MS
Density of State	DOS
Partial Density of State	PDOS
Local–density approximation	LDA
Generalized gradient approximation	GGA
Exchange–correlation energy	XC energy
Homogeneous electron gas	HEG
Perdew–Burke–Ernzerhof	PBE
Broyden–Fletcher–Goldfarb–Shanno	BFGS
Limited memory Broyden–Fletcher–Goldfarb–Shanno	L–BFGS
Molybdenum diselenide	$MoSe_2$
Molybdenum disulfide	MoS_2

List of figures

Figure 11.	The d–band center trends of the (a) Pt and (b) Pd at the convex side with different amplitudes of ripple from the center part to the edge part. The d–band center trends of (c) Pt and (d) Pd at the concave side with different amplitudes of ripple from the center part to the edge part.
Figure 12.	The energy differences of Pt with (a) the uniaxial tensile and compressive strains, and (b) the biaxial tensile and compressive strains.
Figure 13.	The work functions of Pt with (a) the uniaxial tensile and compressive strains, and (b) the biaxial tensile and compressive strains.
Figure 14.	(a) The PDOS of Pt-5d orbitals with 2 to 10% uniaxial tensile strains, and (b) with 2% to 10% uniaxial compressive strains.
Figure 15.	The PDOS of Pt-5d orbitals with 2 to 10% biaxial (a) tensile and (b) compressive strains.
Figure 16.	The d–band center trends of Pt changed with the (a) uniaxial tensile and compressive strains, and (b) biaxial tensile and compressive strains.
Figure 17.	The single–point energies of Pd with (a) uniaxial tensile and compressive strains, and (b) biaxial tensile and compressive strains.
Figure 18.	The work functions of strained Pd with (a) uniaxial and (b) biaxial tensile and compressive strains.
Figure 19.	The PDOS of Pd–4d orbitals with 2 to 10% uniaxial (a) tensile strains, and (b) compressive strains.
Figure 20.	The PDOS of Pd–4d orbitals with 2 to 10% biaxial (a) tensile strains, and (b) compressive strains.

Figure 21.	The d–band center trends of Pd changed with the (a) uniaxial tensile and compressive strains, and (b) biaxial tensile and compressive strains.
Figure 22.	The single–point energy changes of MoS_2 and $MoSe_2$ with different amplitudes of ripple.
Figure 23.	The work functions of MoS_2 and $MoSe_2$ with different amplitudes of ripple.
Figure 24.	The band gaps of MoS_2 and $MoSe_2$ under the 1 Å to 8 Å height of ripple.
Figure 25.	The band structures of MoS_2 under the (a) 1 Å and (b) 4 Å height of ripple.
Figure 26.	The band structure of $MoSe_2$ under 1 Å of ripple.
Figure 27.	The DOS changes of MoS_2 under the 1 Å to 8 Å height of ripple.
Figure 28.	The DOS changes of $MoSe_2$ under the 1 Å to 8 Å height of ripple.
Figure 29.	The PDOS of s, p, and d orbitals of MoS_2 with (a) 1Å of ripple, and (b) 8 Å of ripple.
Figure 30.	The PDOS of s, p, and d orbitals of $MoSe_2$ with (a) 1Å of ripple, and (b) 8 Å of ripple.
Figure 31.	(a) The single–point energy difference of MoS_2 under the uniaxial tensile strain through the x–, the y–axis, and biaxial tensile strain through the x– and y–axis. (b) The single–point energy difference of MoS_2 under the uniaxial compressive strain through x–, y–axis, and the biaxial compressive strain through the x– and y–axis.
Figure 32.	The single–point energy difference of $MoSe_2$ under the uniaxial tensile strain through x–, the y–axis, and the biaxial tensile strain

	through x– and the y–axis. (b) The single–point energy difference of $MoSe_2$ under the uniaxial compressive strain through x–, the y–axis, and the biaxial compressive strain through x– and the y–axis.
Figure 33.	(a) The work function trend of MoS_2 under the uniaxial tensile strain through x, y axis, and biaxial tensile strain through the x– and y–axis. (b) The work function trend of MoS_2 under the uniaxial tensile strain through the x–, the y–axis, and the biaxial tensile strain through the x– and the y–axis.
Figure 34.	The work function trend of $MoSe_2$ under the uniaxial tensile strain through the x–, y–axis, and the biaxial tensile strain through the x– and the y–axis.
Figure 35.	The bandgap trend of MoS_2 with different types of (a) tensile strain, and (b) compressive strain.
Figure 36.	The band gap of $MoSe_2$ with different types of (a) tensile strain, and (b) compressive strain.
Figure 37.	The band structure of MoS_2 of (a) 2%, and (b) 10% of biaxial tensile strain. The band structure of MoS_2 of (c) 2%, and (d) 10% of biaxial compressive strain.
Figure 38.	The band structures of $MoSe_2$ of (a) 2%, and (b) 10% of biaxial tensile strain. The band structures of $MoSe_2$ of (c) 2%, and (d) 10% of biaxial compressive strains.
Figure 39.	The DOS of MoS_2 with different biaxial tensile strains on the x– and y–axis.
Figure 40.	The PDOS of s, p, and d orbitals of MoS_2 with 2% biaxial tensile strain.

Figure 41.	DOS of $MoSe_2$ with different biaxial tensile strains on the x– and y–axis.
Figure 42.	The PDOS of s, p, and d orbitals of $MoSe_2$ with (a) 2% tensile strain, and (b) 10% tensile strain.

Acknowledgement

First and foremost, I would like to express my sincere appreciation to my supervisor, Prof. Huang Bolong, for his precious and continuous guidance, feedback, advice, and support throughout my PhD studies and research work on this thesis. His guidance and encouragement gave me the motivation to preserve more and more knowledge and strength. Without his support, it will be unattainable for me to finish my research work in my PhD studies.

I am also indebted to Prof. Yu Wing–yiu, Michael, for his academic support during my final year of research.

Besides my supervisor, I am also grateful to my senior, Ms. Sun Mingzi, who has provided technical support to my calculations and assisted me in overcoming the challenges. Her advice expanded my critical thinking and understanding in my research work.

In addition, my sincere gratitude also goes to my groupmate on my research team, for the unwavering support and academic communication. The communication and discussion with them helped me to determine the problem and find a method to solve the problem.

Also, I want to present my gratitude to the Department of Applied Biology and

Chemical Technology (ABCT). Their academic support is helpful for me to fulfill the requirements of the coursework and credit.

Last but not least, I would like to heartfeltly appreciate my friends, my family, and everyone who gave me the unwavering support and encouragement throughout my research life of my PhD program. Their support and encouragement help me to face depression and control my emotions. Without their accompany, my research work, coursework, and other relevant work would not be able to be completed. Any words and actions from them are invaluable, irreplaceable, and motivate me to progress in my whole life.

Table of Contents

Chapter 1
Introduction

1. Introduction

Nowadays, material science is one of the important research topics, which involves different applications concerning our daily lives. The low–dimensional materials possess different desired properties, including mechanical, electrical, optical, optoelectronic, magnetic, thermal properties, etc. Due to the specific nature different from the bulk material, these materials, such as the transition metal chalcogenide (TM C), demonstrate varying potential applications in different fields.

In order to broaden the applications, improve the properties and stabilize these materials, more and more research is being conducted to optimize the method for various materials. Doping,[1] alloying,[2] defect inducing,[3] structure combining[4], strain engineering,[5] and other methods are commonly used to tune the material properties and fulfill the demand. Among these methods, strain engineering is a relatively simple method to effectively change material properties.

1.1 Low–dimensional materials

Low dimensional (LD) materials are where at least one of the dimensional materials is small enough (at the nanoscale). In other words, LD materials contain the 0–dimensional (0D) materials, 1–dimensional (1D) materials and 2–dimensional (2D) materials.[6] The properties of LD materials are different from the 3–dimensional (3D)

materials because of the quantum confinement effect.[7] Once the dimensions of the material are reduced to the nanoscale, the movement of electrons are confined in other directions; thus, low–dimensional materials demonstrate specific properties. 0D materials have an atomic–like structure, where the electrons cannot move in these materials.[8] 1D materials have a hollow tube–like structure, where the electrons are limited to move through the non–nanoscale direction.[9] 2D materials have a plane–like structure, where the electrons can only transfer on the 2D planar.[10] **Figure 1** shows the structures and examples of the LD materials. The limitations of the electronic movement change the electronic structure of these materials from their bulk form. For some specific materials, such as the semiconductor, transition metal, the LD form of these materials demonstrates unique properties in the field of optics, thermal, magnetic, and mechanics.

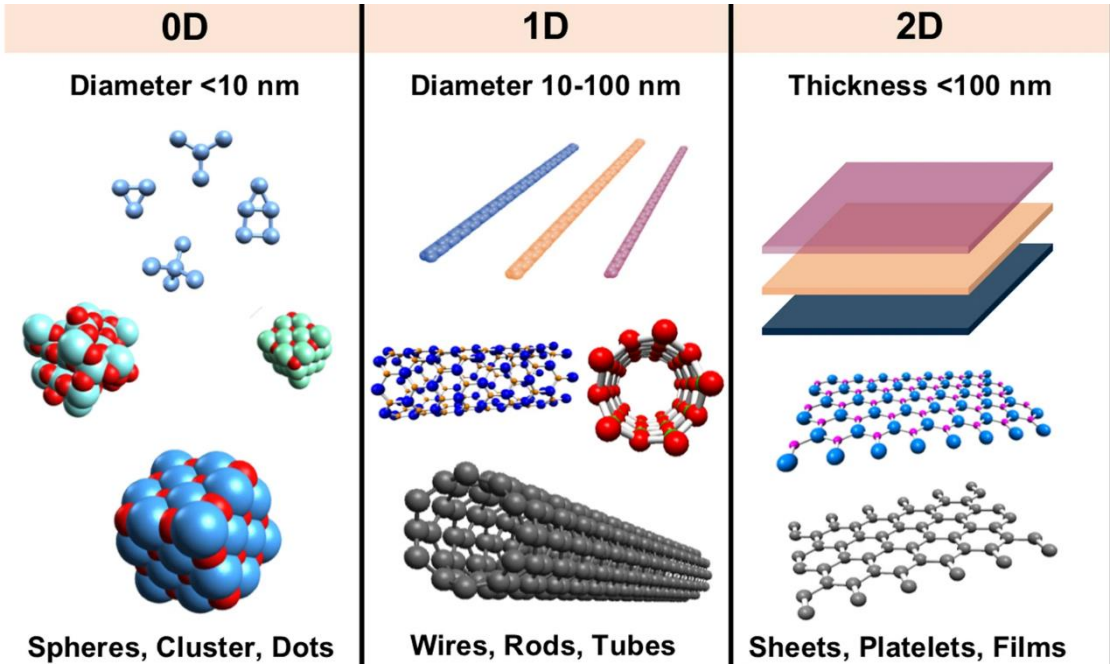

Figure1. The structure and example of 0D, 1D, and 2D material.[11]

In addition to the quantum confinement, the LD materials possess a high surface area,

and thus, these materials possess extremely high surface area–to–volume ratio compared to bulk materials. The high surface area increases the contact of the reactants on the surface during the reaction, where the efficiency of these materials is higher than the bulk material with the same volume. In living organisms, the large surface area–to–volume ratio certainly enhances the exchange rates of nutrients and waste, and the adsorption of sunlight.[12] Compared to bulk materials, LD material possesses better flexibility and strength, enabling it to endure more stress without fracture or rupture. Benefitted from these advantages over the traditional bulk materials, LD materials are gradually used for the emerging applications, such as the supercapacitors, new–type batteries, quantum counterparts, and biofilms.[13]

Benefitted from the specific properties different from bulk materials, LD material attracted the attention of scientists, and countless efforts were made to study these materials. The study of LD materials facilitates interdisciplinary research and explores more potential of these materials in different fields.

1.2 Transition metal and Transition metal chalcogenide

Transition metal chalcogenide (TMC) is one type of common semiconductor, where it consists of a transition metal atom (M) and several chalcogenide atoms (X).[14] Generally, TMC can exist in two forms, transition metal dichalcogenide (TMD) and transition metal trichalcogenide (TMT), with the chemical formulas of MX_2 and MX_3, respectively. Molybdenum disulfide (MoS_2) is the most common TMC and is considered representative of the whole family of TMC.[15] **Figure 2** shows the typical structure of TMC. Owing to their semiconducting characteristics, TMCs are commonly used to produce different electronic devices and components, such as the light–emitted

diode (LED), the electrical chip of the graphics processing unit (GPU), and the electrolyte for electrocatalytic reaction.[16] In addition, the appropriate thickness of the direct bandgap (around 1–3 eV) is one of the critical properties that make it a suitable optoelectronic component. Moreover, the strong spin–orbit coupling characteristic directly affects the magnetic and electronic properties of TMC.[17] As a result, TMC is widely applied in different fields and improves the performance of the products.

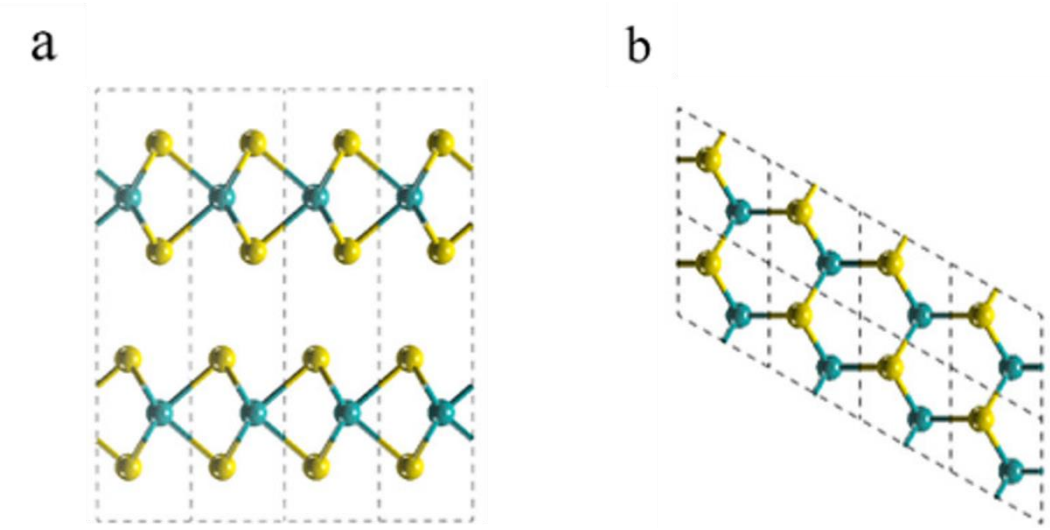

Figure 2. The typical structures of TMC on the (a) side, and (b) top. [18]

Besides the TMC, the low–dimensional transition metals (TM) are another type of common material that is applied in electrocatalysis. The previous studies commonly focused on the strain and ripple effect on the surface of semiconductors, where these effects on the TM are seldom investigated. Owing to the high stability, specific d–state, and synergistic effect with other metal atoms, TM is generally applied for different electrocatalytic reactions to accelerate the reaction.[19] Besides, the variable oxidation states and the corrosion resistance of TM bring extra attention from researchers in various fields. For instance, the variable oxidation states lead to different colors, magnetic properties, and the reactivity of TM. In general, the pure form of TM is

corrosion–resistant because of the stability of formed metal oxide layers on the surface. The high corrosion resistance enhances the protection ability of TM, which can be used as a protection layer to resist corrosion.[20, 21]

Environmentally friendly, energy supply and storage, carbon neutralization, safety, and other issues have gradually become important in recent years. TM and TMC possess the unexplored potential in the field of material science, which is a critical component of these issues. For instance, TM is commonly applied as the electrocatalysts for different electrocatalytic reactions, such as the hydrogen evolution reaction (HER), oxygen reduction reaction (ORR), oxygen evolution reaction (OER), etc. (**Figure 3**)[22-24] These reactions involve the core of the fuel cell, and the new types of energy solutions. On the other hand, TMC possesses a specific electronic structure, which can be used as the energy supply of clean energy, such as solar energy. Nevertheless, more and more studies and efforts are continuously made to further develop and expand their applications concerning energy supply. One of the possible methods is strain engineering, which is relatively simpler than the other methods to change the properties of the LD TM and TMC.

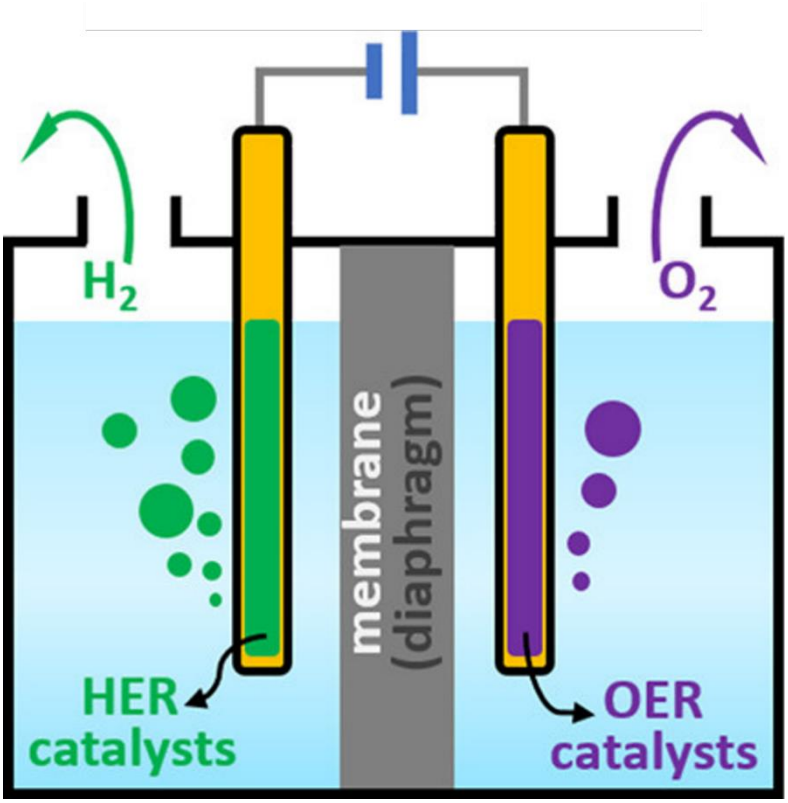

Figure 3. The illustration of conventional water electrolyzes for HER and OER with TM. [25]

1.3 Strain engineering

Strain is a type of deformation in the material due to external stress, whereas surface strain refers to deformation on the surface of the material.[26] Surface strain can be defined by this equation:

$$\varepsilon = \frac{l_f - l_0}{l_0}$$

where ε is the strain, l_f is the final surface length of materials and l_0 is the original surface length of materials. Under stretching, the material will be elongated and the value of $l_f - l_0$ becomes positive, implying that tensile strain is produced in the

material.[26] On the other hand, under the compression on the material, the value of $l_f - l_0$ becomes negative, where the compressive strain is produced. **Figure 4** demonstrates the illustration of LD material with tensile, compressive, and no strain. The modulation of the orbital and electronic structure significantly changes the properties of materials, particularly for LD materials.

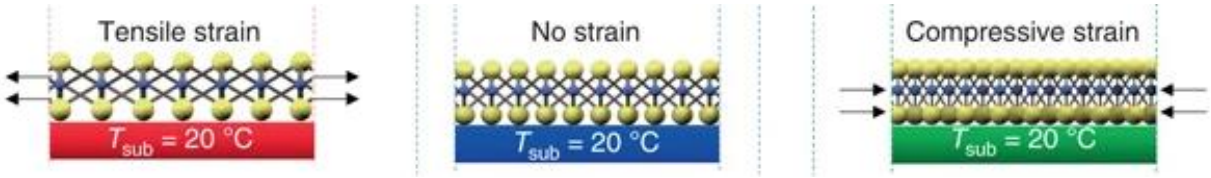

Figure 4. The illustration of LD material with tensile strain, no strain, and compressive strain. [27]

The induction of these strains on the surface of the material elongates or compresses the interatomic distance and then changes the overlapping of the orbitals and the electronic structure. The elongation and the compression on the surface of LD materials sometimes change the thickness of these materials. The thickness change causes the partial 3D and partial 2D structures in the LD materials, resulting in the specific electronic structure and the orbital overlapping.

Strain engineering is a method to modulate material properties through the introduction of surface strain. Various methods can be used to induce strain into the material, including stretching,[28] compressing,[28] bending,[29] lattice mismatch,[30] heating,[31] the tip of atomic force microscopy (AFM),[32] and other methods. Moreover, different properties, including optoelectronics, electronics, bandgap, phase transition, and piezoelectricity, can be modulated easily through strain engineering.[33] Although strain engineering is effective in modulating the structure and tuning

properties of LD material, it is not available to modulate the properties of bulk material. For example, the LD graphene can be elongated 25% compared to the original form, whereas only 1% strain causes the fracture of the bulk graphene. In this case, strain engineering effectively modulates the bandgap and the crystal momentum of TMC and thus tunes the electronic and optical properties. Besides the modulation of TMC, the strain effect enables tuning the d orbitals of TM through the modification of the interatomic distance of TM atoms. The interatomic distance effectively changes the electrocatalytic properties of TM.

1.4 Recent Research Progress

Benefitting from the quantum confinement effect and the specific properties of TMC itself, LD TMCs have attracted the interest of various scientists. Compared to 0D and 1D materials, the application of 2D materials is much more intensive in different fields. For example, TMC thin film can be used as the electrolyte in the electrocatalytic reaction due to the extremely large surface–to–volume ratio.[34] In addition, the sensing capacity of the 2D TMC–based gas sensor has obviously improved because of its high sensitivity and high reliability.[35]

Johari and Vivek investigated the band structure change of the TMC under the strain effect, including the MoS_2, $MoSe_2$, $MoTe_2$, WS_2, WSe_2, and WTe_2.[36] They applied the DFT to calculate the band gaps of different TMC under different strains. The theoretical calculations show that the tensile strain and compressive strain are able to reduce the band gap of TMC, where compressive strain is less effective than tensile strain for the band gap reduction. In addition, the uniaxial strain is less effective than the biaxial strain to reduce the band gap of TMC. Moreover, the 10% biaxial tensile

strain is the most effective way to reduce the band gap of TMC, where the band gaps of all TMCs are reduced to the minimum. Besides the band gap, the magnetism, optoelectronics, and other electric properties of TMC are tunable through strain engineering. Chittari et al.[37] used the ab initio calculations to study the 2D transition metal trichalcogenide (TMT). Through the calculations, they found that the antiferromagnetic and ferromagnetic order of these TMT are tuned by strain engineering. (**Figure 5a**) Lu et al.[38] applied the DFT calculations to predict the piezoelectricity of different TMC. (**Figure 5b**) The results showed that around 10% of the tensile strain enhanced the piezoelectric coefficient of these piezoelectric TMC by over 100%. At the original state, the piezoelectric coefficient of $ReSe_2$ is –120 pm/V, whereas the piezoelectric coefficient of Au_2Se_2 is 326 pm/V with 5% tensile strain.

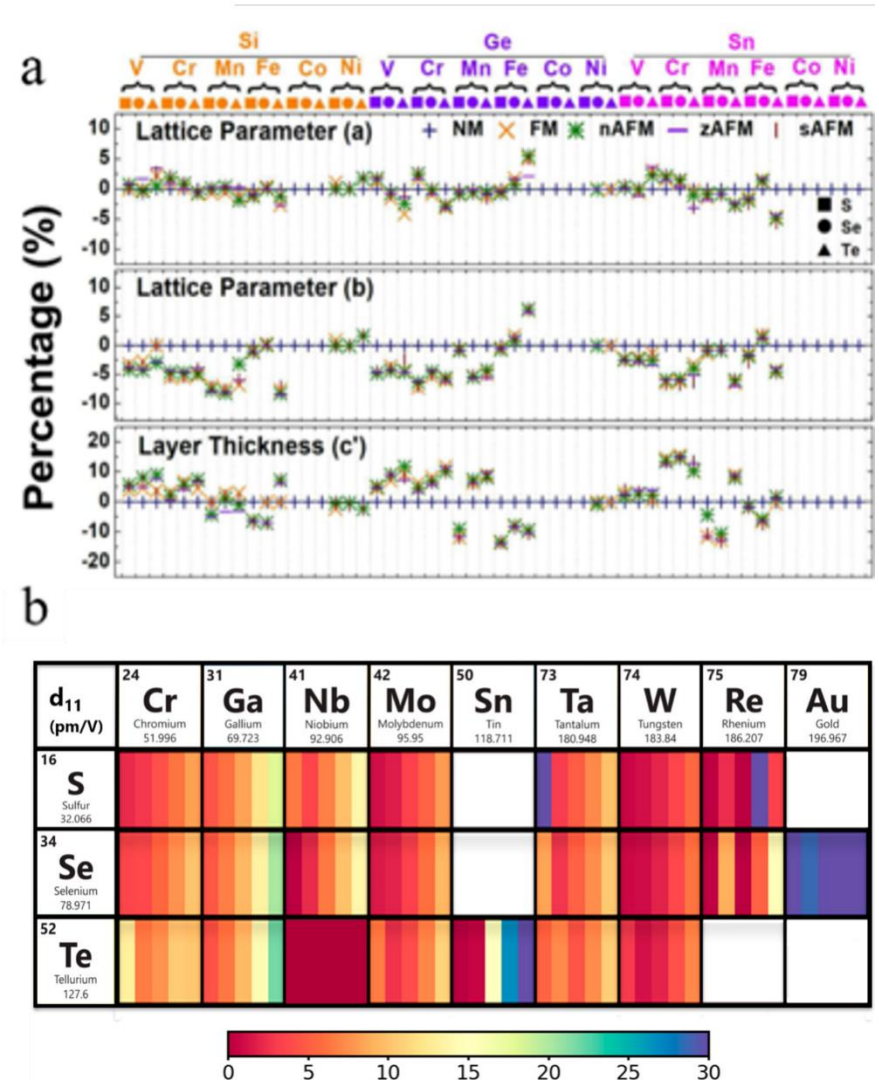

Figure 5. (a) The calculations of antiferromagnetic and ferromagnetic order of the 2D TMT within DFT–D2.[37] (b) The piezoelectric coefficients of the calculated monolayer TMC with different strains.[38]

TM commonly possesses various excellent properties, such as variable oxidation states, excellent electrical conductivities, and good catalytic properties. The excellent properties of TM have extensively expanded the application of TM in different fields. For example, owing to the d–d electron transitions, TM form colorful compounds as the raw material of industrial dyes, pigments.[39] Moreover, TM is commonly applied to synthesize different industrial products, such as stainless steel, electrical wire, and

alloys. Furthermore, TM exists in the body of organisms in a different form. For instance, iron is involved in the formation of hemoglobin, which carries oxygen to transport to different parts of the organism in the blood.

To study the strain effect on TM, different researchers attempted to determine the relationship between TM and the strain effect. Zhong et al.[40] combined the theoretical calculations and the experimental measurements to investigate the relationship between the surface strain effect and the HER reaction of Pt–based metallic compounds. According to the results, they plot a volcano trend concerning the compressive strain and the HER activity of the Pt–based metallic compound. In addition, Huang et al.[41] tuned the surface strain on the Pd/C catalyst for the CO_2 reduction. At –0.8 V, for the CO production, they finally reached the maximum Faradaic efficiency of 91.1%. They also found that the tensile strain upshifts the d–band center of Pd, which enhances the electrocatalytic rate.

1.5 Research Value and Purpose

Although a large amount of time and resources are invested in investigating the properties of TMC and TM under different conditions, some properties of TMC and TM remain unknown. Moreover, most of the experiments focus on a single property change of a specific target under the strain effect. Furthermore, it is difficult to completely determine the relationship through experimental measurement, because it requires the investment of massive resources and time.[42] In contrast to experimental measurement, the first–principles computational calculations requires less investment of time and resources. However, the target selection still needs a lot of time. Besides the time consumption, the results calculated by the first–principles computational

method may deviate from the normal range.[43]

Various research studies on the properties of LD materials, TMs and TMCs, and the property changes under strain engineering. The literature demonstrates the potential and performance of LD TMC and TM, which is worth studying the properties further. Moreover, different experimental and theoretical results indicate that strain engineering can effectively modify the properties of LD TMC and TM. Therefore, we aim to:

1. To study the surface strain effect on LD TMC and TM on the electronic structures and lattice distortions.
2. To understand how the strain influences the properties of TMC and TM regarding different properties of materials, including the electrical conductivity, band structure, carrier mobility, and crystal momentum.
3. Establishing the correlation between the strain effect and the lattice structure further facilitates the modulation of the strain effect.
4. To apply the underlying mechanism of the strain effect to materials with similar structures beyond TM and TMC.
5. To find the most effective method for property modification by the comparison of different strain effects and ripple effects.

The modification of the morphology of the TM and TMC models will be performed by the program, Atomsk. To achieve the purposes of this thesis, the computational calculations will be performed by the software named Materials Studio.[44] The details of the methodology of these theoretical methods are discussed in the next section.

The results in this thesis should help to determine the relationship between the strain effect, TM, and TMC, where the relationship can be qualified as an equation. Moreover, the qualification of the relationship can provide a guide to further developing the strain engineering technique. The results certainly assist in controlling the strain induction for the property modulations of these materials. Developing and implementing the strained materials expand the application of LD TM and TMC, which can undoubtedly benefit the development of the energy supply and storage device and, thus, significantly enhance the quality of our daily life.

Chapter 2

Methodology

2. Methodology

2.1 Atomsk

Atomsk is a free and open–source program that supports the creation, modification, and operation of atomic–scale simulation data files. It is compatible with various programs and file formats in computational material science, including visualization and analysis software, Ab initio calculation software, classical force–field simulation software, and TEM image simulation software.[45]

In cases, the BIOVIA Material Studio can only move the atoms one by one in the modification of the morphology. As a result, the application of Atomsk is necessary for the modification of the morphology of different model sets. Atomsk provides the functions to generate the lattice structure and modify its morphology. In this case, Atomsk is used to induce the strain with different deformations and ripples with different amplitudes. For the strain, the 2 – 10% elongation or compression is induced to the surface of the TM and TMC. For the ripple, the following equation is applied to simulate the deformation of the ripple on the sample:

$$A = a \cos bx \tag{1}$$

Equation (1) is applied to construct the uniaxial ripple of TMC and TM. In Eq. (1), a represents the amplitude of the ripple, which ranges from 1 – 8 Å. The b represents the periodicity of the ripple, which ranges from 1 – 2, where 1 and 2 imply the half – rippled and full – rippled model.

For the strain, the model of TM and TMC are constructed to simulate the elongation and compression by the following equation:

$$\varepsilon = (1 + x\%)\, l \tag{2}$$

$$\varepsilon = (1 + y\%)\, l \tag{3}$$

$$\varepsilon = (1 + x\%)\, l + (1 + y\%)\, l \tag{4}$$

Equations (2) and (3) represent the uniaxial tensile and compressive strain, where Equation (2) corresponds to uniaxial strain on the x–axis, and Equation (3) corresponds to uniaxial strain on the y–axis. Equation (4) represents the biaxial strain on both x– and y–axis of model. The value of x and y represents the strain, which ranges from –10 to 10. The value of –2, –4, –6, –8, and –10 corresponds to the compressive strain, whereas the values of 2, 4, 6, 8, and 10 correspond to tensile strain. In the Equation (4), x and y are also ranged from –10 to 10, which have the same value.

2.2 BIOVIA Materials Studio

BIOVIA Materials Studio (MS) is one of the common software that provides a user‐friendly and easy operation environment to researchers for modeling, simulation and calculation. BIOVIA MS allows researchers to further study the relationship between the atomic and molecular structure of a material and its properties and behavior, where the calculations and predictions are performed. MS supports the modelling of different types of materials, including the catalysts, polymers, composites, metals, alloys,

pharmaceuticals, batteries, etc., in the field of the industries are engineering.[46, 47]

MS offers the “in silico first” approach to the user for the optimization of the performance of material in a relatively low–cost environment before experimental measurement. [48] In addition, MS possesses several advantages for exploring, predicting, and calculating the properties of materials. First, MS can assist in accelerating the innovation process. Through the utilization of MS, researchers can have an in–depth understanding of the properties of materials with a relatively easy method. And then, the usage of MS can effectively reduce the R&D cost. The simulations and calculations by MS can reduce the experimental measurements for testing the optimized condition. Through virtual screening, researchers can minimize the experiments to determine the target materials. Moreover, the usage of MS significantly improves R&D efficiency. MS allows automating and sharing best practices within Pipeline Pilot, which assists researchers in optimizing the condition with necessary tasks and attempts. Finally, the application of MS facilitates data–driven decisions. The calculation data provides extra information to support the experimental results and supplement the necessary explanations. [49, 50]

2.2.1 The CASTEP calculation

The CASTEP package is one of the calculation methods embedded in MS, which can be used to simulate and calculate the properties of various materials. These materials, such as ceramics, metals, semiconductors, and other materials, can be calculated by the plane–wave DFT method.[51]

CASTEP is typically applied for the studies of the surface of material, the structural properties of materials, band structures, Density–of–State (DOS), and other properties. Besides these properties, CASTEP is also capable of performing other calculations, including the single–point energies, elastic constants, geometry optimizations, molecular dynamics simulations, searching and confirmation of the transition states.[52, 53]

In this case, the model is built by MS, and then the morphology of all models is modified through the software Atomsk, including the strained and rippled TM, TMC models. Geometry optimizations will performed on the modified models to determine the stable form and the relevant information.

2.2.2 The settings of the CASTEP

In this thesis, the settings of the CASTEP used for different models are the same. For the task, geometry optimization is chosen to find the most stable form of the material after relaxation. For the functional, the local density approximation (LDA) and the Perdew–Burke–Ernzerhof (PBE) functional are chosen. The cutoff energy is set as ultra–fine quality with 320 eV. For the k–point setting, the Gamma quality with 1 x 1 is chosen for the calculation. The pseudopotential is set as the ultrasoft quality. The SCF tolerance is set as the ultra–fine quality. The orbital occupancy is set as 72%. The Broyden–Fletcher–Goldfarb–Shanno (BFGS) algorithm is chosen to optimize the numerous values.

2.3 Density Functional Theory

Density Functional Theory (DFT) is a common computational calculation method that applies to the quantum mechanical modelling to study, estimate, and calculate the electronic–related properties of the many–body system.[54] DFT is commonly applied for physics, chemistry, and material science, where the calculations can be used to estimate the properties of the many–body system. For the calculation, the function can be used as the input, i.e., the functionals of the spatially dependent electron density, and then output the numeric value. In other words, the DFT calculations enables the estimation and prediction of the material behaviours based on the electronic structure, where the calculations do not require the properties of the target material.[55]

The classic electronic structure theory, particularly for the Hartree–Fock Method and post–Hartree–Fock Method, is based on the complex wave function of an N–electron system. Each electron contains 3D coordination, which causes the classic theory to require considering the 3N coordination.[56] To solve the problem of the classic theory, DFT applies the electronic density to replace the N–electron system, where the electronic density only requires considering the 3D variables of the electronic density. [57]

2.3.1 The Schrödinger Equation

The Schrödinger equation can be expressed by this equation:

$$i\hbar \frac{\partial}{\partial x}\Psi(x,t) = [-\frac{\hbar^2}{2m}\frac{\partial^2}{\partial x^2} + V(x,t)]\Psi(x,t)$$

where the Ψ (x, t) is the wave function that assigns multiple numbers to different positions x at different times, t. The m represents the mass of the particle. V (x, t) is the potential of the environment between the particles. i is the imaginary unit, and ħ is the reduced Planck constant.[58]

In classical physics, Newton's second law describes the movement of objects, whereas this equation is the quantum counterpart of the classic law. In quantum mechanics, Schrödinger equation is the basic part, which is necessary for the quantum–related study. This equation describes the quantum state of the physical system, which is expressed as a time–dependent partial differential equation. In addition, it is available to apply to the microsystem, macrosystem, and even the universe.[59]

The Schrödinger equation can be classified as the time–dependent Schrödinger equation and the time–independent Schrödinger equation. The time–dependent Schrödinger equation describes the relationship between time and the wave function in a quantum system.[60] The time–dependent Schrödinger equation can be expressed by this equation:

$$i\hbar \frac{d}{dx} |\Psi(t)\rangle = \hat{H} |\Psi(t)\rangle$$

In this equation, t represents the time, $|\Psi(t)\rangle$ represents the state vector in a quantum system, and the $\hat{H}$ is the observable Hamiltonian operator.

In contrast, the time–independent Schrödinger equation describes the physical

properties of a stationary state quantum system, where the solution of the time–independent Schrödinger equation can be determined by the wave function of the stationary state quantum system.[61] The time–independent Schrödinger equation can be expressed by this eqaution:

$$\hat{\mathrm{H}}\,|\Psi(t)\rangle = E|\Psi(t)\rangle$$

In this equation, E represent the energy in the quantum system.

Schrödinger equation contains several properties, including linearity, unitarity, the change of the basis, and the probability current.

The Schrödinger equation is a linear differential equation, which implies that if two state vectors in the Schrödinger equation are the solutions, then the solution for Schrödinger equation can be found from the linear combination of the two vectors solution .[62]

$$|\Psi\rangle = a\left|\Psi_1\right\rangle + b\left|\Psi_2\right\rangle$$

In this equation, the Ψ_1 and the Ψ_2 are the solution vectors, whereas a and b are any complex numbers. In addition, any number of solution vectors can be used to extend the sum of the equation. Owing to the linearity property, the solution of the Schrödinger equation can be found from the superpositions of quantum states. In other words, the weighted sum over a basis of states is applied to find the solution. Commonly, the basis of energy eigenstates is generally chosen to determine the solutions of the time–

independent Schrödinger equation.[63]

Unitarity is the common characteristic of the time–dependent Schrödinger equation. The unitarity ensures that the inner product between vectors to maintained in the Hilbert space.[64] If the initial state is $\left|\Psi(0)\right\rangle$, then for the unitarity operator $\widehat{U}(t)$, the state at the later time t, can be expressed by this equation,

$$|\Psi(t)\rangle = \widehat{U}(t)\left|\Psi(0)\right\rangle$$

Sometimes, the Schrödinger equation is expressed by the quantities changing with the function of positions. However, in the Hilbert space, the Schrödinger equation possesses a valid representation in any arbitrary complete basis of ket. [65] Besides, the bases located outside the physical Hilbert space can also be applied for the calculation, where the bases can be described by a nonrelativistic, spinless particle in the position–space and momentum–space Schrödinger equations.[63] For the nonrelativistic, spinless particle, the complex square–integrable functions on 3D Euclidean space generate the Hilbert space.[66] In this space, the Hamiltonian contains the different terms, including potential energy and the momentum operator, which causes the sum of the kinetic energy.[67]

For the probability current, the Schrödinger equation maintains the consistency with the local probability conservation.[68] The consistency ensures that the normalization of the normalized wavefunction is preserved after time evolution, which implies that the time evolution operator is a unitary operator in the matrix mechanics.

2.3.2 The Hartree–Fock Method

The Hartree–Fock Method is commonly used to estimate the wave function and the energy of the stationary state.[69] Sometimes, this method supposes that the single Slater determinant or the single permanent of N spin–orbitals can be applied to approximate the exact N–body wavefunction in a system. The theoretical background of DFT is based on the Schrödinger equation, which involves the approximation of wave functions. One of the common solutions for approximations is the Hartree–Fock Method.[70] The approximation of the Hartree–Fock Method brings a problem: this method neglects the electron correlation, where it assumes the electrons move independently of each other. To overcome this shortcoming, the post–Hartree–Fock method is applied for DFT.

The post–Hartree–Fock Method is improved to include the electron correlation of the wave function of the multi–electron system.[71] The post–Hartree–Fock Method contains different approaches. Among these approaches, the Møller–Plesset perturbation theory perturbs the Fock operator to treat the correlation.[72] Besides the Møller–Plesset perturbation, other approaches, including the multi–configurational self–consistent field, configuration interaction, quadratic configuration interaction, and complete active space SCF (CASSCF), expand the true wave function of the multi–electron system.[73-75] In addition, other approaches apply the correlation function to multiply the wave function of Hartree–Fock for the modification. This approach is explicitly a multiple–electron function, where the approach cannot be resolved into the individual function of each single electron.

2.3.3 Hohenberg–Kohn Theorems

The Hohenberg–Kohn Theorem is one of the fundamentals of DFT, where the ground state energy in an electronic system can be applied to describe the functional of the electron density n(r).[76] The first Hohenberg–Kohn Theorem defines the statement: In any interacting many–particle system with a given fixed inter–particle interaction, the functional of the electron density n(r), can be used the ground state as the input. In other words, the ground state wave function can be applied as a functional of the ground state electron density.[77]

The first Hohenberg–Kohn Theorem provides the statement and proves the relationship between the ground state energy and electron density n(r). However, the first theorem lacks a description of the actual form of the functional.[78] Therefore, the second Hohenberg–Kohn Theorem is provided to supplement the description of the important property of the functional. According to the second theorem, the minimized energy of the overall functional is the true electron density, which can be applied to find the solution of the Schrödinger equation. After the determination of the minimized energy of the overall functional, the variation of the electron density can be applied to minimize the energy and then determine the electron density on the ground state. The determination of the electron density in the ground state can be applied to calculate the properties of the target.[79]

2.3.4 Kohn–Sham Equations

Kohn–Sham equation is a set of mathematical equations that are applied to simplify the problem concerning the electronic movement and activity in the atoms and

molecules.[80] This equation uses the virtual non–interacting electrons to determine the most stable arrangement of electrons. At the atomic and molecular scale, this equation effectively assists in the prediction of the properties of materials.

The Kohn–Sham equation is a non–interacting Schrödinger equation of a fictitious system (the "Kohn–Sham system") for the DFT. This system consists of non–non–interacting particles, such as electrons, where the density of these particles is the same as any given system of interacting particles.[81]

In the Kohn–Sham theory, the noninteracting kinetic energy functional, T_S, can be introduced to the equation. After the functional differentiation, the Kohn–Sham orbitals are obtained, where the Kohn–Sham orbitals are the solution for the Kohn–Sham orbitals.[82]

In the Kohn–Sham equation, the local effective potential can be expressed as v_s (r) or v_{eff} (r). It can also called Kohn–Sham potential, where it defines the Kohn–Sham equation.[83] In the Kohn–Sham system, the particles are non–interacting fermions, where the single Slater determinant can exactly solve the Kohn–Sham equation.[84] The orbital in the determinant is the Kohn–Sham orbital; In this case, a linear combination of the atomic orbitals can be used to express the set of Kohn–Sham orbitals.[85]

Kohn–Sham equation can use the following equation to express:

$$\left(-\frac{\hbar^2}{2m}\nabla^2 + v_{eff}(r)\right)\emptyset_i(r) = \varepsilon_i\emptyset_i(r)$$

In this equation, the ε_i is the orbital energy of the Kohn–Sham orbital $\emptyset_i$. For the Kohn–Sham with N–particles, the following equation determine the electronic density:

$$p(r) = \sum_{i}^{N}\left|\emptyset_i(r)\right|^2$$

2.3.5 Pseudopotential

Pseudopotential, or called effective potential, is an approximation to simplify the description of a complex system, which is commonly applied as the potential for the bandgap calculation.[86] The pseudopotential is the expansion of the Orthogonalized Plane Wave method, which can be applied to atomic physics, such as the neutron scattering.[87]

The potential between the motion of the core electron, such as the non–valence electron, of an atom and its nucleus causes the complex effect; therefore, the Schrödinger equation uses the improved effective potential term to replace the original Coulombic potential of the core electrons for the calculation.[88] The pseudopotential is applied to solve the complex effects of the core electrons by replacing the full potential of the core electrons. Through the pseudopotential, the pseudo–wavefunction with fewer nodes is applied to describe the valence electrons. The pseudopotential allows the application of far fewer Fourier modes; therefore, the plane–wave basis set is used for the

calculation.[89]

The atomic reference state derives the first–principles pseudopotential, for which the pseudo– and all–electron eigenstates are required to possess equal energies, amplitudes, and the density outside the selected core cut–off radius. When the cut–off radius is larger, the pseudopotential becomes softer. In other words, the convergence of the calculations will be faster.[90] However, the softer pseudopotential will cause lower transferability, which implies that the reproducibility of the realistic features in different conditions and environments will be reduced.[91]

In conclusion, the pseudopotential is aimed at several purposes, including reducing the scale of the basic sets, reducing the number of electrons, as well as including relativistic and other effects. In addition, pseudopotentials use the small–core approximations to assume that the core and the wave function do not have a significant overlap. In this case, when the overlap between the wave function and core is non–negligible, the nonlinear core corrections or the “semicore” electron inclusion will be used to handle this condition.[92, 93]

In the early development of the pseudopotential, the application of pseudopotential for the atom and solid was based on the attempt to fit atomic spectra. However, the application of this condition only achieves limited success. In 1958, Walter Harrison and James C. Phillips successfully applied the pseudopotential to fit different models, including aluminum (Al), silicon (Si) and germanium (Ge). These calculations involve the nearly free electron Fermi surface and the covalent energy gaps. The successful cases from them largely assist in enhancing the present popularity of

pseudopotential.[94]

2.3.6 LDA Functional

Local–Density Approximation (LDA) functional is a common approximation, which is applied for the exchange–correlation (XC) energy. This functional only changes with the value of the spatial electronic density at different point.[95] Although lots of methods are able to yield the local approximation of XC energy, the homogeneous electron gas (HEG) model leads to the most accurate cases of the derivation of the local approximation. In other words, the success derived local approximation is commonly based on the synonymous functionals from the HEG model and then applied to the real cases.[96]

LDA is commonly used in the ab–initio DFT studies of solid–state physics to explain the electronic and magnetic interactions of different materials. The systematic complexity of DFT calculations leads to the high sensitivity of the synthesis parameters, where the first–principles analysis is necessary for the calculation.[97] For the doped semiconducting oxides, calculating the Fermi level and band structure commonly requires a simulation package with the LDA, such as CASTEP and DMol3. Sometimes, the underestimation of the bandgap from the LDA causes a false calculation result and predictions of these materials. In 1998, combining the Rayleigh theorem with the LDA functional can calculate the bandgap of materials with satisfactory performance.[98]

2.3.7 GGA Functional

The generalized gradient approximation (GGA) functional is another approximation

that is commonly used in DFT calculations, which is the simplest one–point functional.[99] In the DFT with the GGA functional, the value of the XC potential is based on the electron density n(r) and the gradient of the potential, which form a complex function in 3D space. [100] In this function, at a given point, the gradient of the electron density n(r) partially explains the inhomogeneous distribution of electron density n(r) and some non–local effects. The following equation expresses the GGA functional:

$$E_{XC}^{GGA}[n_{\uparrow}, n_{\downarrow}] = \int \varepsilon_{XC}(n_{\uparrow}, n_{\downarrow}, \nabla n_{\uparrow}, \nabla n_{\downarrow})\, n(r) d^3r$$

The utilization of GGA assists in enhancing the performance of the calculations of ground–state energy and molecular geometry. In general, the accuracy of meta–GGA functional is higher than the GGA functional, which is the natural development after the appearance of GGA.[101] The GGA DFT only includes the electron density and the related first derivative in the XC potential. The meta–GGA functional improves the disadvantage of GGA, where the original form of meta–GGA includes the second derivative of the electron density in the exchange–correlation potential.[102]

2.3.7.1 Perdew–Burke–Ernzerhof Functional

The Perdew–Burke–Ernzerhof (PBE) functional is one of the common types of GGA functionals that is widely applied to DFT calculations.[103] John Perdew, Kieron Burke, and Matthias Ernzerhof developed the PBE functional in 1996.[104] They designed this method to address the problems of XC energy calculation. By including the gradient of electron density, PBE calculations provide a more accurate result for a broad range of materials compared to the LDA functional calculation.

In computational calculations, the PBE functional balances computational efficiency and calculation accuracy. In some cases, the catalytic system and model possess high complexity and then resulting in the difficulty of the calculation.[105] The PBE functional provides satisfactory performance in terms of time consumption, efficiency, and the accuracy of the energy and structural calculations for these systems.

2.3.8 Broyden–Fletcher–Goldfarb–Shanno Algorithm

Broyden–Fletcher–Goldfarb–Shanno (BFGS) algorithm is an algorithm that is applied to solve different unconstrained nonlinear optimization problems.[106] This algorithm was developed by Charles George Broyden, Roger Fletcher, Donald Goldfarb, and David Shanno in 1970.[107-110] BFGS precondition the gradient with curvature information to determine the descent direction.[111] Through the Hessian matrix of the loss function, the BFGS algorithm gradually improves the approximation and then determines the descent direction. The result is only obtained from the gradient evaluations through the generalized secant method.

Along with the development of BFGS, the matrix inversion becomes unnecessary for the curvature matrix, and the computational complexity reduces with the update of BFGS. In general, the most common BFGS method is the Limited Memory BFGS (L–BFGS), where this version limits the memory of the algorithm. This method is common used when the systems exist large amount of variables.[112]

The optimization problem of the BFGS algorithm is the minimization of the differentiable scalar function f(x). In this case, there are no limitations on x to take the

value. For the beginning, the BFGS algorithm assumes x_0 is the initial point of the optimal value, and then proceeds iteratively at each stage to obtain an improved value.[113]

From the beginning value x_0 and the initial Hessian matrix, the BFGS algorithm applies and repeats the following processes to optimize the value and determine the solution of the value of x_k:

1. Through the equation $B_k p_k = -\nabla f(x_k)$, the direction p_k will be obtained.
2. Conduct the one–dimensional optimization (line search) throughout the direction p_k obtained in step 1. The optimization will find the appropriate stepsize α_k in this direction. If this line search is exact, then the $\alpha_k = \arg\min f(x_k + \alpha p_k)$. In fact, when the Wolfe conditions are satisfied for the α_k, then the line search is inexact.
3. Set the $s_k = \alpha_k p_k$, and then let the $x_{k+1} = x_k + s_k$
4. Calculate the equation: $y_k = \nabla f\left(x_{k+1}\right) - \nabla f(x_k)$
5. Finally, solve the equation: $B_{k+1} = B_k + \frac{y_k y_k^T}{y_k^T s_k} - \frac{B_k s_k s_k^T B_k^T}{s_k^T B_k s_k}$

The f(x) should be the minimized objective function. The norm of the gradient $\|\nabla f(x_k)\|$ is applied to check for the convergence test.

Chapter 3

The surface strain and ripple effect of transition metals Pt and Pd

3. The surface strain and ripple effect of transition metals Pt and Pd

3.1 The brief introduction and background of Pt and Pd

Up to now, there has been very little research conducted on the surface strain and ripple effect on the transition metal. In this section, Pt and Pd are selected as the target to investigate the strain and ripple effect. After the structural optimization, different electronic properties, including density–of–states (DOS), work function (WF), as well as the d–band center, were studied.

Due to the electrocatalytic property, Pt is commonly used as an electrocatalyst, especially for the ORR and HER in different energy–related devices. The ability of Pt effectively enhances the efficiency of these electrocatalytic reactions and facilitates the development of new–type energy. Besides the electrocatalytic reactions, Pt converts harmful substances, for example, the carbon monoxide (CO), nitrogen oxides (NO_2), and other air pollutants, into less toxic substances.[114] These reactions reduce the toxicity of air pollutants and effectively improve the environment. Like Pt, Pd is commonly applied to electrocatalytic reactions and the conversion of harmful substances. For instance, in a fuel cell, Pd can help to catalyse the hydrogen oxidation reaction (HOR).[115, 116] In addition, Pd enables the conduct of various organic conversion reactions, such as the Suzuki and Heck, and cross–coupling reactions.[117] The surface property allows Pt and Pd to strongly adsorb the reactant during the catalytic reaction, which further benefits the electrocatalytic and organic applications of Pt and Pd.

Although Pt and Pd are common electrocatalysts due to their excellent properties and advantages, some disadvantages limit their application, such as cost, stability, scarcity, durability issues, selectivity, and environmental concerns. Generally, the high cost limits the extensive–scale application of Pt and Pd, especially in backward countries. Although Pt and Pd typically possess high stability, they will degrade over time for different reasons, such as the harsh electrochemical environment, sintering, and the contamination of impurities. These factors significantly reduce stability and durability. In some cases, the selectivity of Pt and Pd causes the formation of undesired by–products. Additionally, the mining and extraction of Pt and Pd cause environmental issues and ethical concerns. Consequently, an effective strategy is necessary to enhance the efficiency and overcome the disadvantages of Pt and Pd.

3.2 The ripple effect on the surface of the transition metal

3.2.1 The morphology and energy evolution of the rippled Pt and Pd

All the original models of Pt and Pd are constructed by the MS. Each model contains 2 layers with 8 x 8 atoms. **Figure 6** shows the morphology of Pt and Pd after the modification by Atomsk. The morphology of full‐rippled Pt and Pd is bridge–shaped. The convex part is the bridge deck, whereas the concave part is the underside of the bridge. The half‐rippled Pt and Pd is a half‐bridge. As mentioned in Chapters 2.1 and 2.2, MS does not support the modification of atoms by pack. As a result, the models of Pt and Pd are constructed by the program, Atomsk. Through the Atomsk, Pt and Pd are constructed as full– and half–rippled with different amplitudes. In the full–rippled model, the analysis will be focused on the surface, and the position of the center to the

edge from the convex and concave sides. This position analysis allows us to investigate the continuous difference between the center and edge of models, which is the maximum morphology difference region in the models. The half–rippled models provide more positions to analyze the strain, DOS, and other properties. The property change of the convex and concave sides will be compared to determine the ripple effect to Pt and Pd.

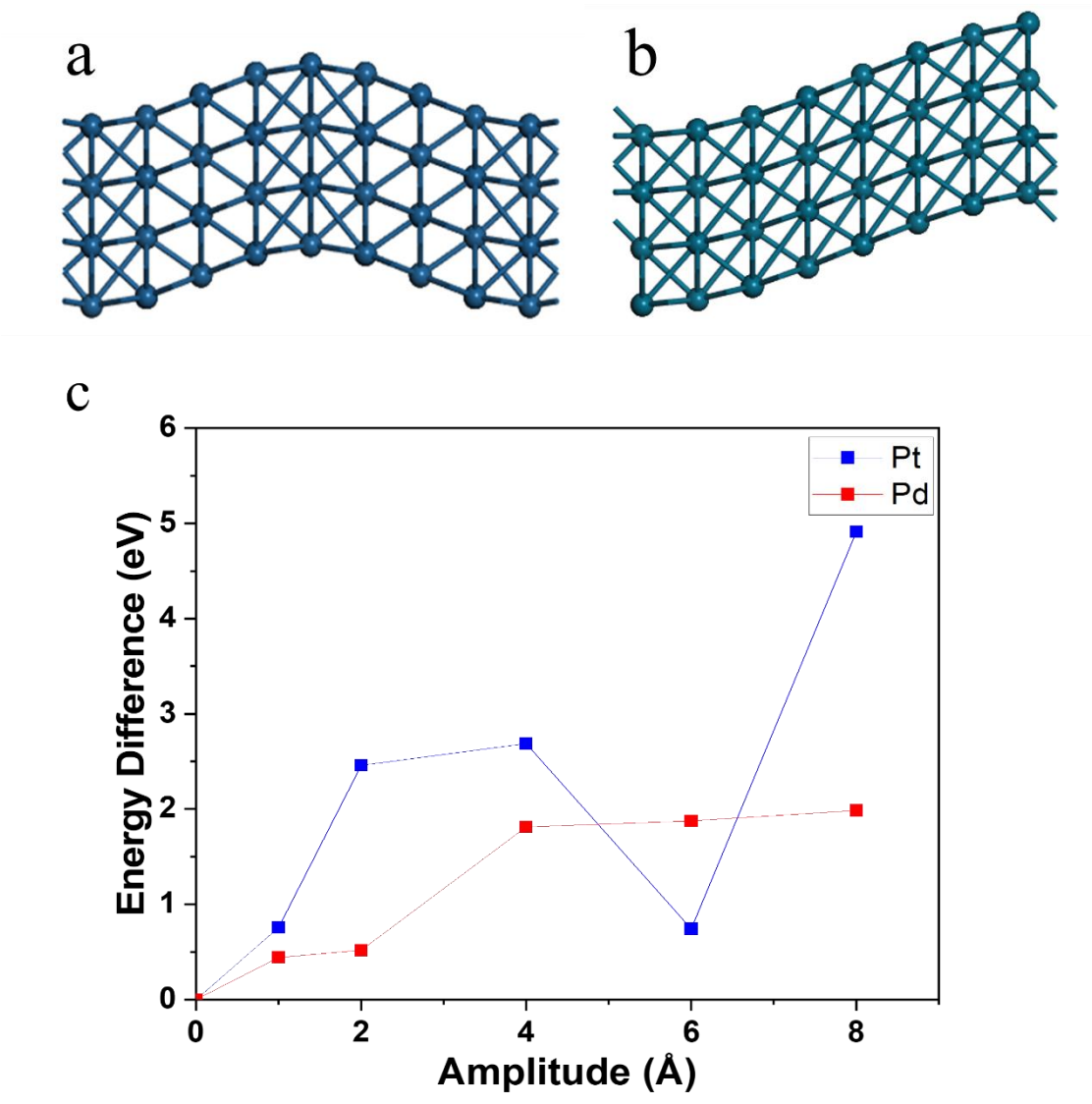

Figure 6. (a) The full–rippled Pt and (b) the half–rippled Pd. (c) The single–point energies of Pt and Pd with different amplitudes of ripple.

In general, the calculations of single–point energy refers to the overall energy of the system; in this case, it is the TM and TMC model, at a fixed geometry without any movement of atoms and the relaxation of the whole structure. The results of the single–point energy provide critical thermodynamic information. Additionally, the data on single–point energy also aids in obtaining information for further calculations and validation with experimental data.

Figure 6 shows the trend of the energy of rippled Pt and Pd with different amplitudes. The single–point energy of Pt and Pd demonstrates an increasing trend with the increasing amplitude of ripples. Energy represents stability, which is dependent on the change of morphology after the relaxation of the model.

The energy difference of Pt shows an overall increasing trend with ripple lengths of 1–8 Å. For Pt, the 1 Å of ripple increases the single–point energy of around 0.5 eV. When the amplitude of ripples increases from 1 Å to 2 Å, the single–point energy of Pt increases by around 2 eV. After that, the 4 Å of ripple causes less increase in single–point energy. The 6 Å of ripple should cause a further increase of the single–point energy in Pt; however, the 6 Å of ripple causes a reduction of the single–point energy. Under the 6 Å of ripple, the single–point energy reduces from the predicted range, which is close to the level of 1 Å of ripple. Finally, the 8 Å of ripple causes an increase in the single–point energy, where the single–point energy increases from around 0.5 eV to 5 eV.

Only the single–point energy of 6 Å height of ripple deviates from the prediction. After relaxations, the arrangement of atoms changes, and then the bond length and the bond

angle also change. The ripple introduction generates the continuous compressed crests and tensile troughs. As the amplitude of the ripple increases, the number of atoms in the compressed region increases. However, the energy accumulation from 1 Å to 6 Å is not linear due to the energetic penalties partially cancelled by the tensile and compressive strain. Besides, the high surface stress, soft shear modes, and strong orbital hybridization significantly release the extra elastic cost at 6 Å. These factors change the average coordination and d-band width of 6 Å rippled Pt, where these results are close to 1 Å rippled Pt. Compared to other models, the morphology of the relaxed 6 Å–rippled Pt model is close to the original 6 Å–rippled Pt model, where other relaxed models show a relatively significant change from the original model. This difference potentially causes the deviation of the 6 Å–rippled model from the prediction.

For Pd, the 1 Å of ripple causes around a 0.5 eV increase of the single–point energy. When the amplitude of ripple increases to 2 Å, the single–point energy slightly increases. Once the amplitude of ripple increases to 4 Å, the single–point energy increases to around 2 eV. The 6 Å of ripple only increases the single–point energy very slightly. Finally, the 8 Å of ripple only causes a slight increase in the single–point energy to the level slightly higher than 2 eV.

The trend of single–point energy in Pt demonstrates an overall increasing trend under the 1 Å to 8 Å of ripples. The single–point energy represents the stability of the material. From the 1 Å to 2 Å of ripple, the morphosis change of Pt after the relaxation is significantly different from the original, non–rippled Pt. Under the 4 Å of ripple, the single–point energy of Pt only has slightly increased, which implies that the morphosis of 2 Å rippled and 4 Å rippled Pt are similar, and their stability of them are close.

However, the 6 Å ripple reduces the stability of Pt to the level of 1 Å rippled Pt, which implies that the stability of 6 Å rippled Pt is the same as 1 Å rippled Pt. Once the amplitude of ripple reaches 8 Å, the single–point energy increases around 5 eV compared to the original no–rippled Pt. The highest single–point energy implies the lowest stability of the 8 Å rippled Pt, and the geometry of 8 Å rippled Pt undergoes a significant change after relaxation. In conclusion, the overall increasing trend of the single–point energy represents the instability, and the significant geometry change under the gradually strengthening ripple, except for the 6 Å rippled Pt.

Compared to the trend of the rippled Pt, the ripple–induced single–point energy of Pd enhancement is less effective. The 1 to 8 Å ripple induction causes the around 0.5 to 5 eV energy change of Pt, whereas the same ripple induction only causes the around 0.5 to 2 eV energy change. Similar to Pt, ripple induction also causes instability, and a significant geometry change in Pd. However, the degree of the increasing trend of Pd demonstrates that Pd is less sensitive to changes in ripple. Under the ripple induction, Pt is more sensitive to the ripple than Pd, which implies that the ripple induction is more effective in modifying the properties of Pt than Pd.

3.2.2 The work function of Pt and Pd

The work function (WF) is the minimum thermodynamic work, such as energy, required to remove an electron from a solid to the vacuum that is outside the solid intermediately.[118] The WF (Φ) can be defined by the following equation:

$$\Phi = E_{vac} - E_F$$

where the E_{vac} represents the energy of the vacuum level, and the E_F represents the energy of the Fermi level.[119]

WF represents the ability of electrons to move between the electrocatalyst and the reactants. In general, lower WF implies that the electrons can easily transfer between the electrocatalyst and the reactant. In contrast, higher WF enhances the difficulty of the electronic movement during the electrocatalytic reaction.

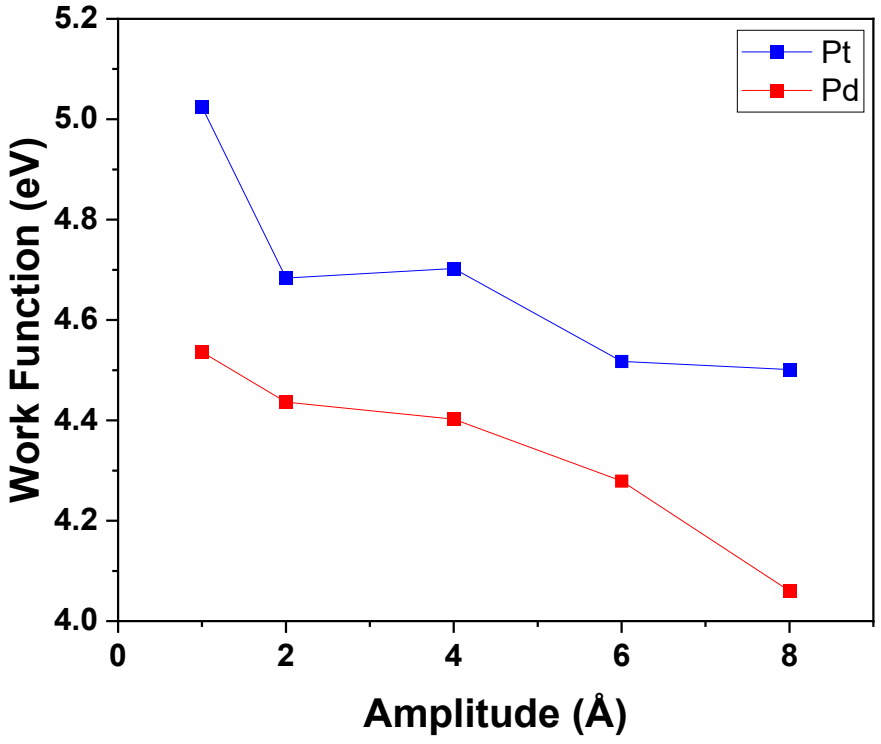

Figure 7. The work function trends of Pt and Pd with different amplitudes of ripple.

Under the ripple, the WF of Pt and Pd is reduced with the increase of the amplitude of the ripple (**Figure 7**). The WF of Pt with 1 Å ripple is around 4.5 eV, whereas the WF of Pd with 1 Å ripple is around 5.1 eV. Once the amplitude of ripple increases to 8 Å, the WF of Pt and Pd reduces to around 4.5 and 4 eV, respectively. The increase in

amplitude of ripples reduces WF.

The change of WF implies that the electrons on the surface of Pt and Pd become easier to withdraw, promoting the ability of charge transfer reaction. The higher amplitude of ripples alters the geometry and surface of Pt and Pd, and thus, changes the electronic structure as well as the surface properties. The WF reaches the minimum with the 8 Å of ripple, which implies that the ripple effectively reduces the WF, and then enhances the efficiency of electronic transfer between the Pt, Pd, and the intermediates.

3.2.3 The bond length and angle changes at different positions

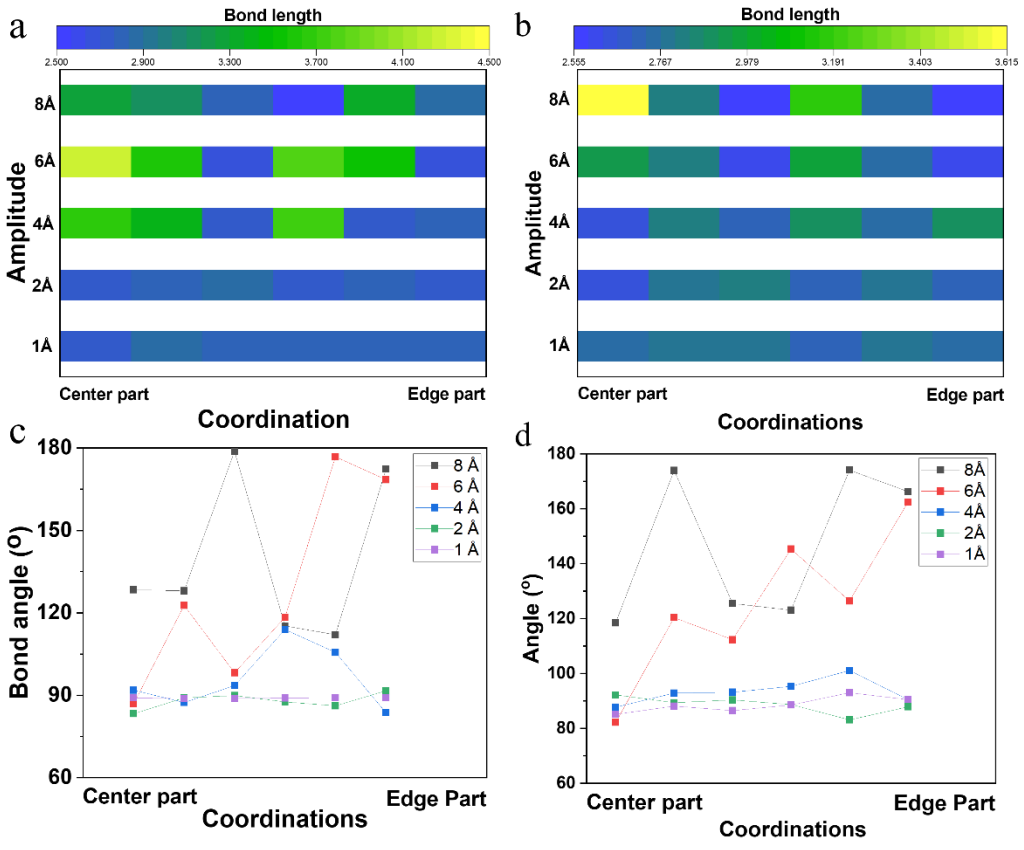

Figure 8. The bond length trends of (a) Pt and (b) Pd with different amplitudes of ripples from the center part to the edge part. The bond angle trends of (c) Pt and (d) Pd

with different amplitudes of ripples from the center part to the edge part.

At the low amplitudes of ripple, there is no noticeable alternation in bond length and angle from the center part to the edge part, where the bond length and bond angle are close to the original form (**Figure 8**). Bond length and angle relate to the interatomic distance and the orbital overlapping; the almost unchanged bond length and angle imply that the interatomic distance and orbital overlapping also remain unchanged.

On the other hand, the higher amplitude causes an obvious change in the bond length and angle. The obvious alternation in the bond length and the angle appears at the center and edge of Pt and Pd. The significant modification of bond length and angle at the center and edge parts implies that the ripple causes a substantial change in the interatomic distance and orbital overlapping at these positions.

3.2.4 The continuous change of the PDOS of Pt and Pd at different positions

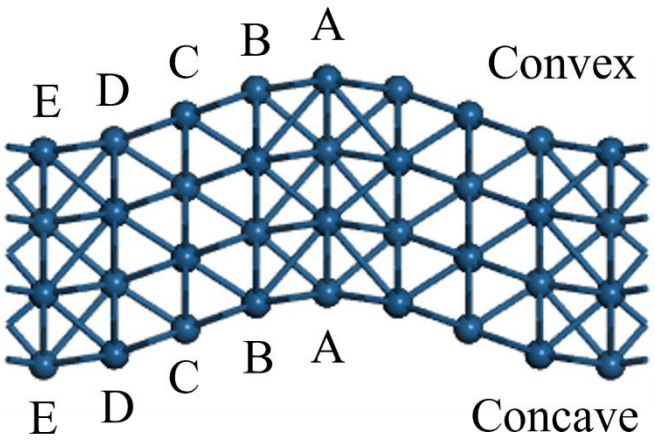

Figure 9. The scheme of point A to point E through the center part to the edge part at

the convex and concave parts of Pt and Pd.

Each TM model possesses 64 atoms (8 atoms x 8 rows) on the surface. After the relaxation, the atoms on the same row are located at the same height, which implies that the properties of each atom on each row are the same. As a result, the following analysis and discussion of PDOS and the d–band center of TM will be followed by the points labelled in **Figure 9**.

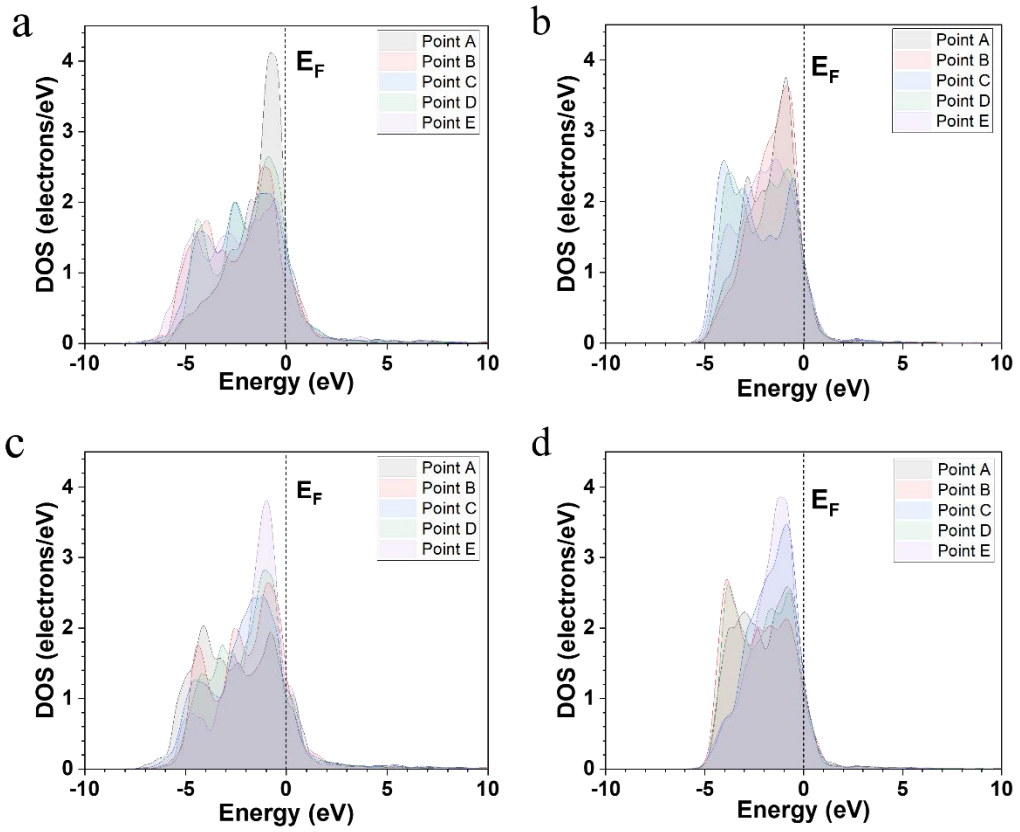

Figure 10. The PDOS trends of the surface at different convex positions for (a) Pt and (b) Pd and at different concave positions for (c) Pt and (d) Pd under 8 Å ripple. Point A to point E represents the position from the center part to the edge part.

Figure 10 shows the partial density of states (PDOS) changes of Pt and Pd on different

positions of the highest ripple. The bond length and angle changes indicate that the interatomic distance undergoes a significant change under 8 Å ripple. In contrast, the lower amplitude of ripple slightly changes the bond length and angle of Pt and Pd, which implies that the orbital overlapping and interatomic distance almost remain unchanged. Therefore, the PDOS analysis is focused on the Pt and Pd with 8 Å ripple.

The PDOS trends of **Figure 10a–b** are opposite to **Figure 10c–d**, which implies that the ripple causes the opposite effects on the convex and concave sides. For Pt, the peak intensity of point A is the highest, and the peaks are most concentrated near the Fermi level.

3.2.5 The d–band center change of Pt and Pd at different positions

The d–band center is an important concept to catalysis, in particular for the surface of TM. The d–band center corresponds to the average energy level of the electrons in the d–orbital of TM. Through the following equation, the d–band centers are calculated:

$$d - band\ center = \frac{\int_{-\infty}^{E_f} \rho E dE}{\int_{-\infty}^{E_f} \rho dE} \quad (5)$$

where p is the d–band density, E is the d–band energy, pdE is the number of states, and E_f is the Fermi level.

The d–band center provides information on TM, including electrocatalytic activity and adsorption strength. The information is essential for various applications, such as the

design of new materials, the understanding of heterogeneous electrocatalysis, and the study of surface science. These applications involve the development of fuel cell, new types of energy, and energy storage, which are the most important fields of study.

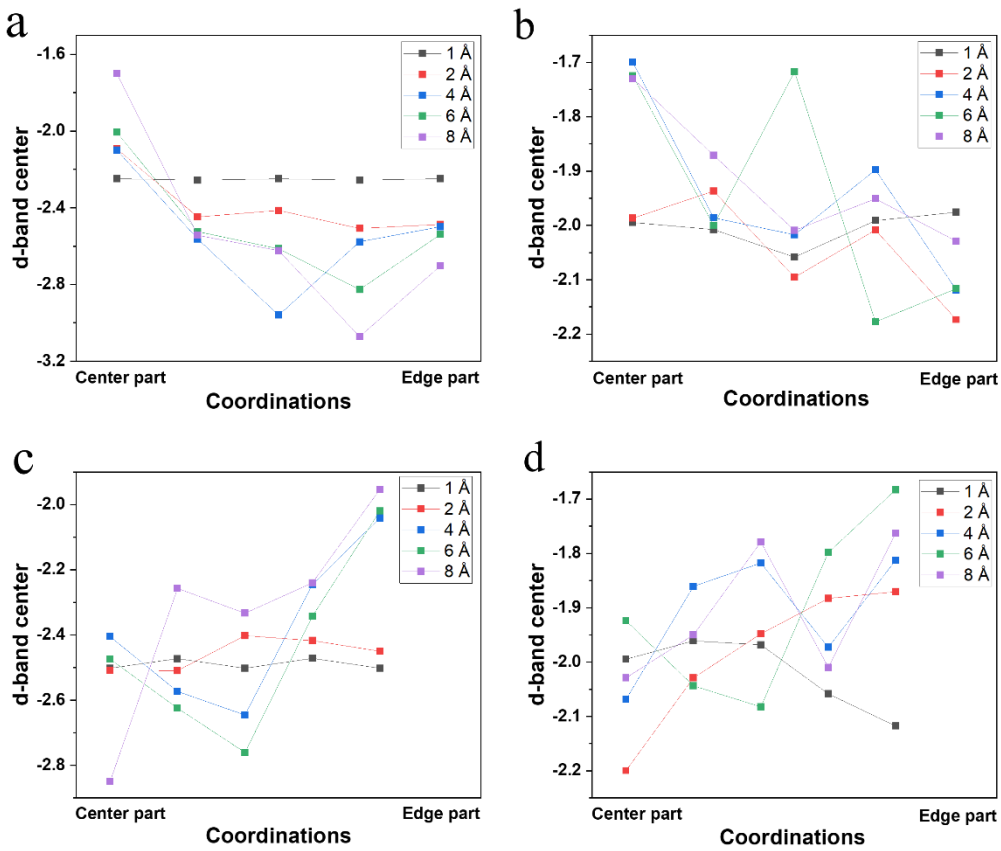

Figure 11. The d–band center trends of the (a) Pt and (b) Pd at the convex side with different amplitudes of ripple from the center part to the edge part. The d–band center trends of (c) Pt and (d) Pd at the concave side with different amplitudes of ripple from the center part to the edge part.

During the electrocatalytic reaction, three processes are involved, including the adsorption process, the chemical reaction, and the desorption process. These processes are related to the electrocatalytic efficiency of the reaction. Therefore, a descriptor is necessary to provide the prediction for electrocatalytic activity. Among the descriptors of the electrocatalytic reaction, the d–band theory is an efficient descriptor to describe

the mechanism of the electrocatalytic reaction. The theory describes the binding mechanism and strength of the intermediates and the adsorbate during the catalytic processes.

The location of the d–band center is useful to determine the electrocatalytic rate of the electrocatalysts. According to the theory, the location of the d–band center is affected by strain induction or coordination. Once the tensile strain is induced into the TM, the interatomic distance of the TM increases, and then reduces the overlapping of the wave functions. Therefore, the band width becomes narrow because of tensile strain, and the population of d–band increases, due to the band width narrowing. Finally, d–band upshifts towards the Fermi level to ensure the degree of d–band filling. The upshifting of the d–band obviously affects the electron occupation in the bonding and the antibonding. When the antibonding is higher than the Fermi level, the possibility of electrons occupying the antibonding reduces, and the electron has more chances to occupy the bonding. As a result, the bonding between the adsorbates and TM increases during the electrocatalytic reactions. The stronger the bonding, the more likely the reaction can be completed and thus enhances the efficiency of the chemical reaction.

However, the excess strength of the bonding makes desorption after the chemical reaction difficult and reduce the efficiency of the electrocatalytic reaction. As a result, further experiments and calculations are necessary to construct a volcano trend of Pt and Pd. The volcano trend helps to determine the optimized ripple for optimal conditions. The data will benefit the development of the next generation of electrocatalysis, offering improved efficiency, quality, and safety.

The trends of WF of Pt/Pd decrease with increasing ripple amplitude because of the introduction of local curvature and strain from the rippling. The changes in local atomic environments and strain from the rippling cause the change in the d–band center at different points on the surface (**Figure 11**). Along with the increase in ripple amplitude, the trends of WF and the d–band center become more apparent, which are consequences of surface strain and modified atomic arrangement due to rippling. Owing to the increasing ripple amplitude, the surface atoms experience stronger strain and lower coordination. As a result, the d–band centers and the WF of Pt/Pd upshift and decrease, respectively. These trends indicate that the surface of Pt/Pd becomes more reactive, and the electrons are less tightly bound to the surface. Therefore, the electrons will be more easily released from the surface of Pt/Pd.

As mentioned above, the modifications of the WF and the d–bands influence the adsorption energy, catalytic activity, and the electron transfer processes, which are critical for the electrocatalysis of Pt/Pd. Through ripple engineering, the d–band center and WF are modified simultaneously, which optimizes the surface properties of Pt/Pd. The ripple effect demonstrates the potential for the further development of Pt/Pd. Ripple engineering has proven its ability to tune surface properties by simple morphology modification, without altering the composition. Meanwhile, the increased reactivity also brings some unexpected side effects, such as selectivity and long–term stability. As a result, DFT calculations and experimental measures are necessary for the next stage of study. According to the results, the ripple effect is expected to apply not only to Pt/Pd but also to other TM catalysts.

3.3 The strain effect on the surface of the transition metal

Besides the ripple effect, the strain effect can also change the surface properties of TM and thus influence the electronic structure. Compared to the ripple effect, the strain effect causes a more uniform and linear deformation to the surface of the transition metal. Similar to the ripple effect, the strain effect also elongates and compresses the interatomic distance. The changes of interatomic distances modify the electronic structure of TM. However, the interatomic distance alterations in 2D, rather than the 3D change, are from the ripple effect. The calculation results of the strain effect on Pt and Pd will be compared with the results of the ripple effect of Pt and Pd.

3.3.1 The strain effect on the surface of Pt

The strain effect evenly and uniformly changes the interatomic distance of Pt, including the elongation and the compression. The changing of the bond length also leads to the changing of the orbital overlapping, and thus change the electronic properties of Pt. Theoretically, the strain also causes the same effect on each atom of TM due to the uniform distribution. In this session, the strain effect on the TM will be investigated to determine the actual effect of strain, including the relationship between strain and TM and the property change.

3.3.1.1 The single point energy of strained Pt

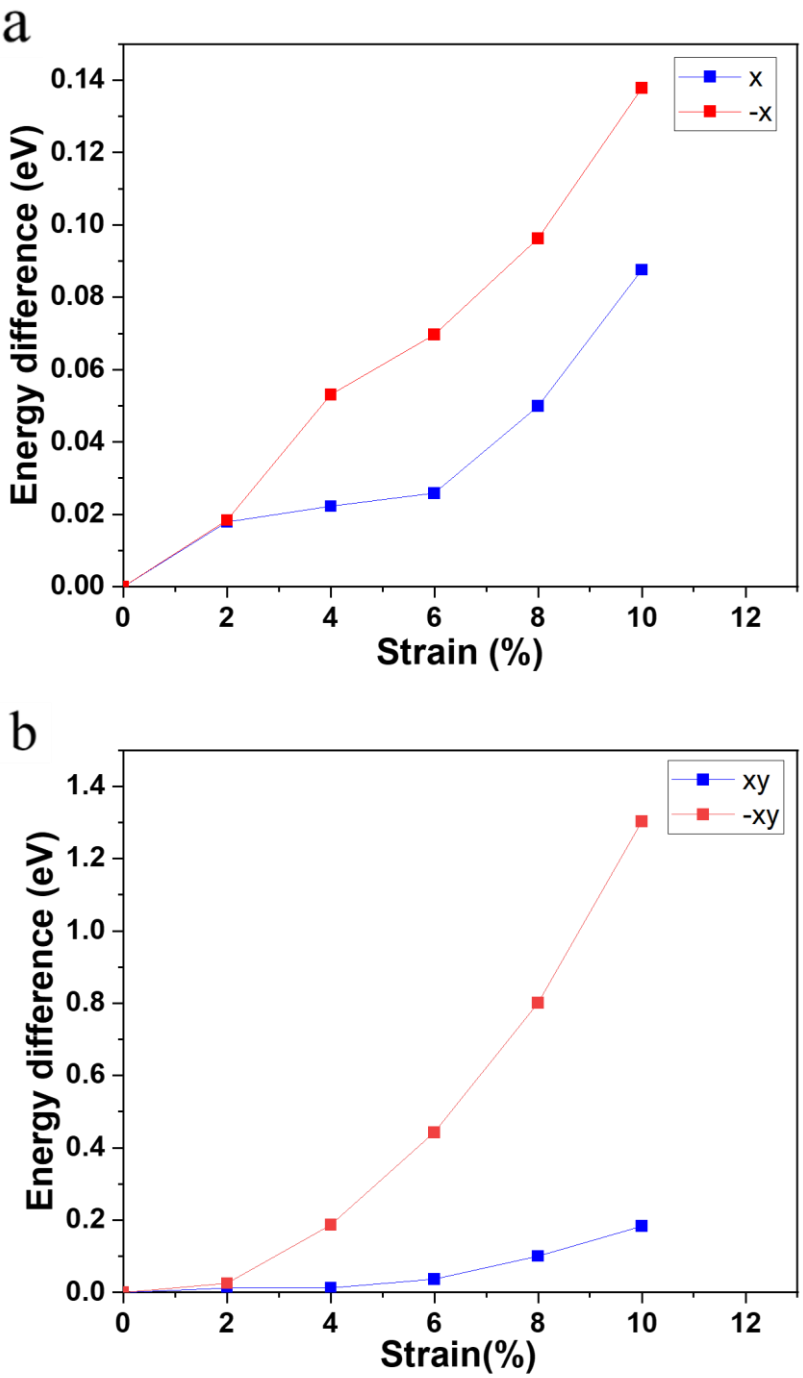

Figure 12. The energy differences of Pt with (a) the uniaxial tensile and compressive strains, and (b) the biaxial tensile and compressive strains.

The induction of the uniaxial tensile strain causes the enhancement of the single–point

energy (**Figure 12a**). The 2% uniaxial tensile strain enhances the single–point energy by around 0.02 eV, and then the 4 and 6% uniaxial tensile strain cause a relatively linear increase of the single–point energy. After that, the 8% uniaxial tensile strain enhances the single–point energy around 0.02 eV. Finally, the 10% uniaxial tensile strain enhances the single–point energy around 0.04 eV.

In contrast, the uniaxial compressive strain results in a more noticeable enhancement in the single–point energy. With the 2% uniaxial compressive strain, the single–point energy increases to around 0.02 eV, which is close to the tensile strain–induced energy change. After the compressive strain up to 4%, the single–point energy difference increases to around 0.05 eV. The 6% compressive strain causes the single–point energy to increase to around 0.07 eV. Once the compressive strain increases to 8%, the single–point energy increases to around 0.1 eV. Finally, the 10% compressive strain increases the single–point energy to around 0.14 eV.

Compared to the single–point energy change induced by uniaxial tensile strain and compressive strain, the compressive strain causes a larger energy difference than the tensile strain. In other words, Pt is more unstable with compressive strain than tensile strain, where Pt demonstrates larger resistance to compressive strain than tensile strain. Tensile strain leads to the surface of Pt to elongate the atomic distance; in opposite, compressive strain compresses the atomic distance. The elongation and compression cause the morphology change, and then unstable the surface of Pt.

The biaxial tensile strain causes a larger increase in the single–point energy (**Figure 12b**). From the 2% to 10% biaxial tensile strain, the single–point energy increases from

around 0.02 eV to around 0.18 eV. In contrast, the biaxial compressive strain results in a more obvious enhancement of the single–point energy. The 2% compressive strain enhances the energy to 0.02 eV. After the strain increases to 4%, the single–point energy increases by around 0.2 eV. The 6% and 8% compressive strain cause the enhancement of around 0.3 eV. Finally, the 10% compressive strain increases the energy from around 0.5 eV to 1.3 eV. The biaxial strain causes a larger increase in the energy compared to uniaxial strain. The biaxial tensile strain elongation further expands the atomic and bond distances, damages the original structure, and then reduces the stability of Pt. In opposite, biaxial compressive strain further compresses the atomic distance, the electrons, orbitals become closer, and then repulse between the electrons. The repulsion causes a noticeable increase in the energy, which causes unstable between the orbitals and the space.

As mentioned above, the energy represents the stability and geometry of the materials, which is related to the morphology of the material. In addition, the single–point trend under the strain is related to the elastic property of Pt. Compared to the ripple effect, the strain effect causes less change in the morphology of Pt and leading to less enhancement of the energy. The relatively low strain causes the relatively low increase of energy, and the slope of energy is more deeply affected by the high strain. The single–point energy represents the geometry and stability of the material. Through the analysis of **Figure 12**, the uniaxial strain gradually reduces the stability of Pt under elongation and compression. Compared to the increase in the energy caused by the ripple effect, the increase in the energy caused by the strain effect can be considered negligible. The trend and the results demonstrate that the strained Pt is more stable than the rippled Pt. Based on the results of **Figure 12**, the discussions and the investigations will focus on

the biaxial tensile and compressive strain.

3.3.1.2 The work function of strained Pt

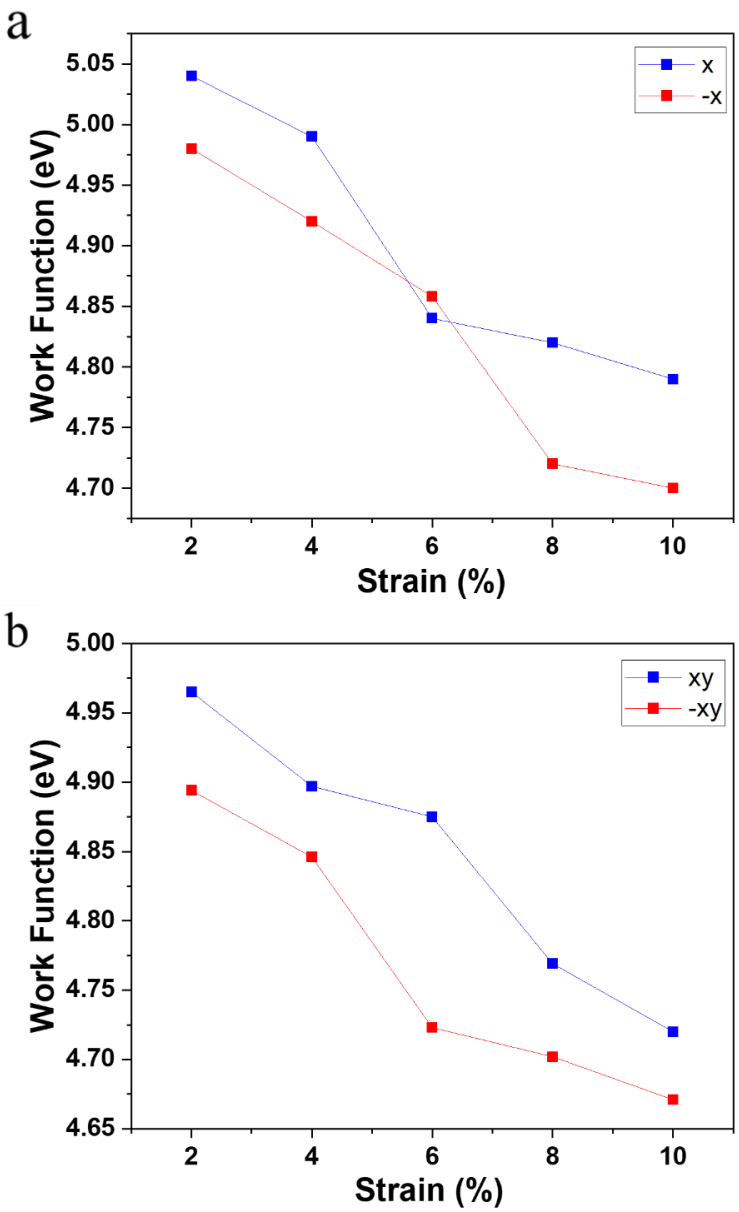

Figure 13. The work functions of Pt with (a) the uniaxial tensile and compressive strains, and (b) the biaxial tensile and compressive strains.

With the uniaxial tensile and compressive strain, the WF of Pt is effectively reduced

(**Figure 13**). With 2% uniaxial tensile strain, WF of Pt is around 5.05 eV. The 4% uniaxial tensile strain reduces the WF of Pt to around 5 eV. After the tensile strain up to 6%, the WF of Pt reduces to around 4.85 eV. After that, the reduction of WF is relatively linear, which ranges from around 4.85 eV to around 4.8 eV. For the uniaxial, compressive strain is more useful than tensile strain to reduce the WF of Pt. The 2% to 6% causes the relative linear reduction of WF of Pt, which reduces from around 4.975 eV to around 4.85 eV. The 8% compressive strain reduces the WF of Pt to around 4.725 eV, and the WF of Pt finally reaches 4.7 eV with 10% uniaxial compressive strain.

On the contrary, biaxial strain causes a more remarkable reduction of WF. The 2% to 10% biaxial tensile strain reduces the WF to 4.975, 4.9, 4.875, 4.775, and 4,725 eV, respectively. And the biaxial tensile strain causes the overall 0.25 eV reduction in the WF of Pt. In contrast, 2% to 10% biaxial compressive strain reduces WF to 4.9, 4.85, 4.725, 4.7, and 4.675 eV, respectively. In this case, the biaxial compressive strain causes the overall 0.225 eV reduction in the WF of Pt. Similar to the uniaxial strain, the WF of Pt also shows a larger reduction between the 4% to 8% strain.

Compared to tensile strain, compressive strain is more useful in tuning the WF, and the biaxial compressive strain is the most effective in reducing the WF of Pt. Compared to the ripple–induced Pt, the strain–induced Pt is less effective in reducing the WF, but the relative linear slope shows the controllability of tuning the WF of Pt.

3.3.1.3 The PDOS of the d orbital of strained Pt

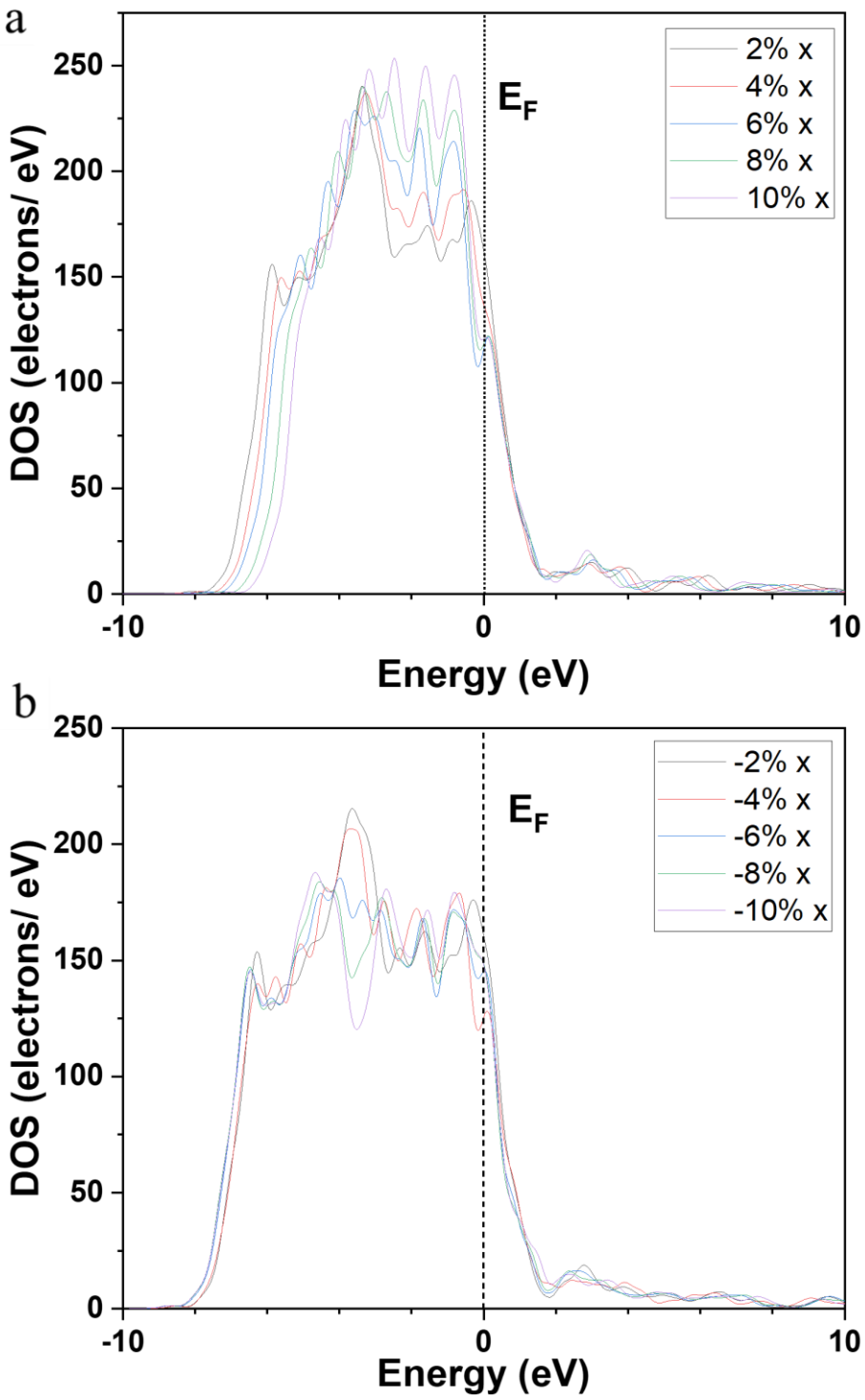

Figure 14. (a) The PDOS of Pt-5d orbitals with 2 to 10% uniaxial tensile strains, and (b) with 2% to 10% uniaxial compressive strains.

In these cases, different strains cause different effects and change the DOS of the d orbital. From **Figure 14**, the tensile strain causes the left side of the PDOS of Pt to shift toward 0 eV. When tensile strain is gradually increased from 2% to 10 %, the left side of DOS is closer to the Fermi level. Besides, the peaks near the Fermi level also change with the increasing tensile strain. When the tensile strain increases, the several peaks near the Fermi level are gradually increased. Moreover, the change of the left side of the DOS and the strengthening of the peak intensity near the Fermi level will change the structure of the DOS and then change the d–band structure and the d–band center. The modifications of the d–band change the electrocatalytic activity of Pt.

On the other hand, the uniaxial compressive strain causes the obvious change of the peaks located around –5 eV. Along with the increase of the compressive strain, the peak intensity demonstrates a reduction tendency. These strains cause the opposite change in the Pt. Tensile strain increases the DOS to a maximum of around 250 electrons/eV, whereas the compressive strain reduces the DOS to a maximum of around 225 electrons/eV.

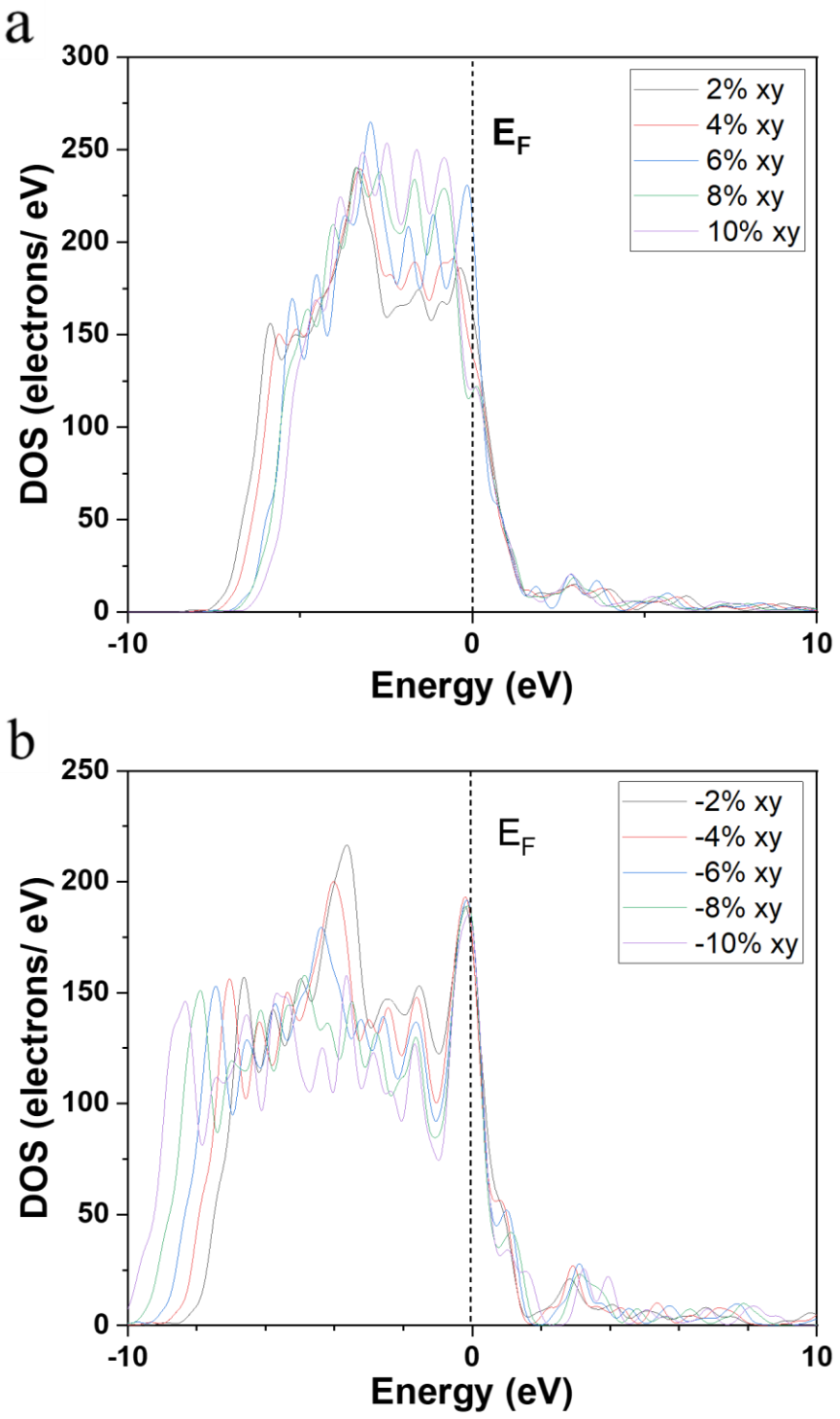

Figure 15. The PDOS of Pt-5d orbitals with 2 to 10% biaxial (a) tensile and (b) compressive strains.

The distribution and the structure of the PDOS of Pt with the induction of biaxial tensile

strain are like the PDOS with uniaxial tensile strain (**Figure 15**). The peak change of biaxial tensile strain is identical to uniaxial tensile strain, where the peak intensity is slightly higher than uniaxial tensile strain. Moreover, the left side of DOS is also slightly different than the uniaxial tensile strain, where the DOS under 6% and 8% tensile strain almost overlap. The induction of the biaxial tensile strain causes the DOS of Pt to demonstrate some changes compared to uniaxial tensile strain. The peak of DOS under biaxial tensile strain reaches a maximum of around 275 electrons/eV, where the maximum of uniaxial tensile strain is around 250 electrons/eV.

With biaxial compressive strain, the overall distribution of the DOS has an obvious change. First, the left side of the DOS demonstrates a trend moving away from the Fermi level. Second, the biaxial compressive cause the peaks appear located at the Fermi level, where the uniaxial compressive strain does not cause the peaks located at the Fermi level. Third, the peak located at around –5 eV is gradually reduced and moves away from the Fermi level. Finally, the maximum of the peak is around 200 electrons/eV, which is higher than the peak of uniaxial compressive strain.

Compared to uniaxial strain, biaxial strain changes the structure of the DOS. The shifting of the left side of the DOS significantly changes the structure and area of the DOS, where the electrocatalytic properties are further altered by tuning the d–band center.

3.3.1.4 The d–band center of strained Pt

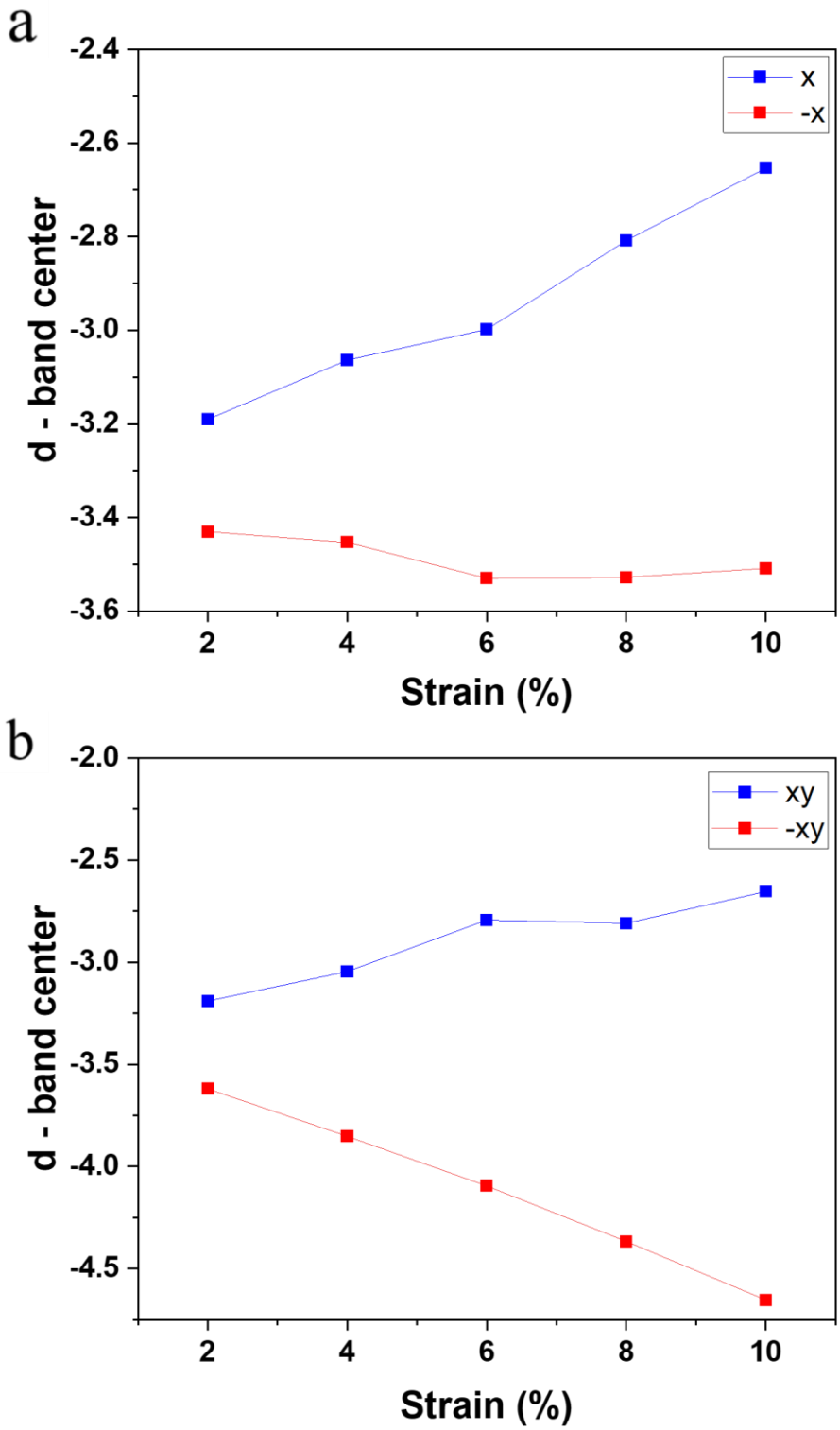

Figure 16. The d–band center trends of Pt changed with the (a) uniaxial tensile and compressive strains, and (b) biaxial tensile and compressive strains.

Under the uniaxial tensile strain, the d–band center demonstrates an increasing trend with the increase of tensile strain (**Figure 16a**). With 2% uniaxial tensile strain, the d–band center of Pt is around –3.2 eV. After tensile strain increases to 4%, the d–band center increases to around –3.05 eV. And then, the 6% tensile strain causes an increase of the d–band center of around 0.05 to –3 eV. Once the tensile strain reaches 8%, the d–band center increases to around –2.8 eV. Finally, when tensile strain reaches 10%, the d–band center further moves toward 0 eV and increases to around –2.6 eV. In contrast, uniaxial compressive strain causes the opposite result to the d–band center. Uniaxial compressive strain reduces the d–band center from around –3.4 to –3.5 eV. When the 6 % is induced to the surface of Pt, the d–band center of Pt reaches the minimum, and then the d–band center slightly increases to around –3.5 eV.

With the biaxial strain, the d–band center of Pt demonstrates more significant and obvious changes, which represent the effectiveness of biaxial strain to tune the d–band center of Pt (**Figure 16b**). Under the biaxial tensile strain, the increasing trend of the d–band center demonstrates an almost linear slope, which increases from around –3.25 to around –2.75 eV. In opposite, the biaxial compressive strain causes the linear reduction to the d–band center, where the d–band center reduces from around –3.5 eV to around –4.75 eV.

As mentioned above, the d–band center is an indicator that can represent the electrocatalytic activity of a metal. The increasing trend of the d–band center indicates that the electrocatalytic rate of Pt changes under the tensile strain effect. The tensile and compressive strain result in the opposite trend to the d–band center. In this case, tensile

strain enhances the electrocatalytic activity, and the electrocatalytic activity reaches a maximum with 10% uniaxial tensile strain. In opposite, uniaxial compressive strain weakens the electrocatalytic activity, and the electrocatalytic activity reaches a minimum with 6% uniaxial compressive strain. The larger strain slightly increases the electrocatalytic activity of Pt.

Although uniaxial tensile and compressive strains cause the opposite result to the d–band center, the slope of the two trends demonstrates that the sensitivity of the two strains to Pt is different. The 2% to 10% uniaxial tensile strain causes the overall increase of the d–band center of 0.6, whereas the 2% to 10% uniaxial compressive strain causes the overall reduction of the d–band center of 0.1 eV. The difference between these strains indicates that the d–band center of Pt is more sensitive to the uniaxial tensile strain than the uniaxial compressive strain. The trend of biaxial strain is opposite to the uniaxial strain. The biaxial tensile strain results in an overall 0.5 eV increase of the d–band center, whereas the biaxial compressive strain causes the overall 1.25 eV reduction of the d–band center.

Compared to ripple–induced d–band center change, strain–induced d–band center change is relatively stable. The ripple causes an uneven and unpredictable change in the bond length and angle. When the adsorbent reacts with the surface of rippled Pt, the adsorbent randomly adsorbs on the surface of the Pt. The uncertain adsorption will cause the unpredictable reaction, where the reaction rate will be different.

The strain–induced d–band center modification is evenly distributed on the surface of Pt. Theoretically, the d–band center of each point on the surface of strained Pt is the

same. The reaction rate should be almost the same at each point. In this case, the reaction rate and efficiency will be controllable under strain engineering.

3.3.2 The strain effect on the surface of Pd

As mentioned above, Pd possesses a specific electronic structure, for example, the partially filled d–band. Benefitting from the specific electronic structure, Pd is generally applied for catalysis, energy storage, and different industrial processes. Through the analysis of single–point energy, DOS, d–band center, and WF, it is proven that the strain is useful in modifying the properties of Pt.

Pd possesses the same column as Pt in the periodic table, which implies that the strain effect leads to a similar result to Pt. The electronic, optoelectronic, and other properties of Pd should be able to be tuned by the strain effect. To understand the effect of strain and expand the application of Pd, the investigation of Pd under different strains is necessary. The investigations provide the information for further investigation, development, and the determination of the optimized condition.

3.3.2.1 The single–point energy of strained Pd

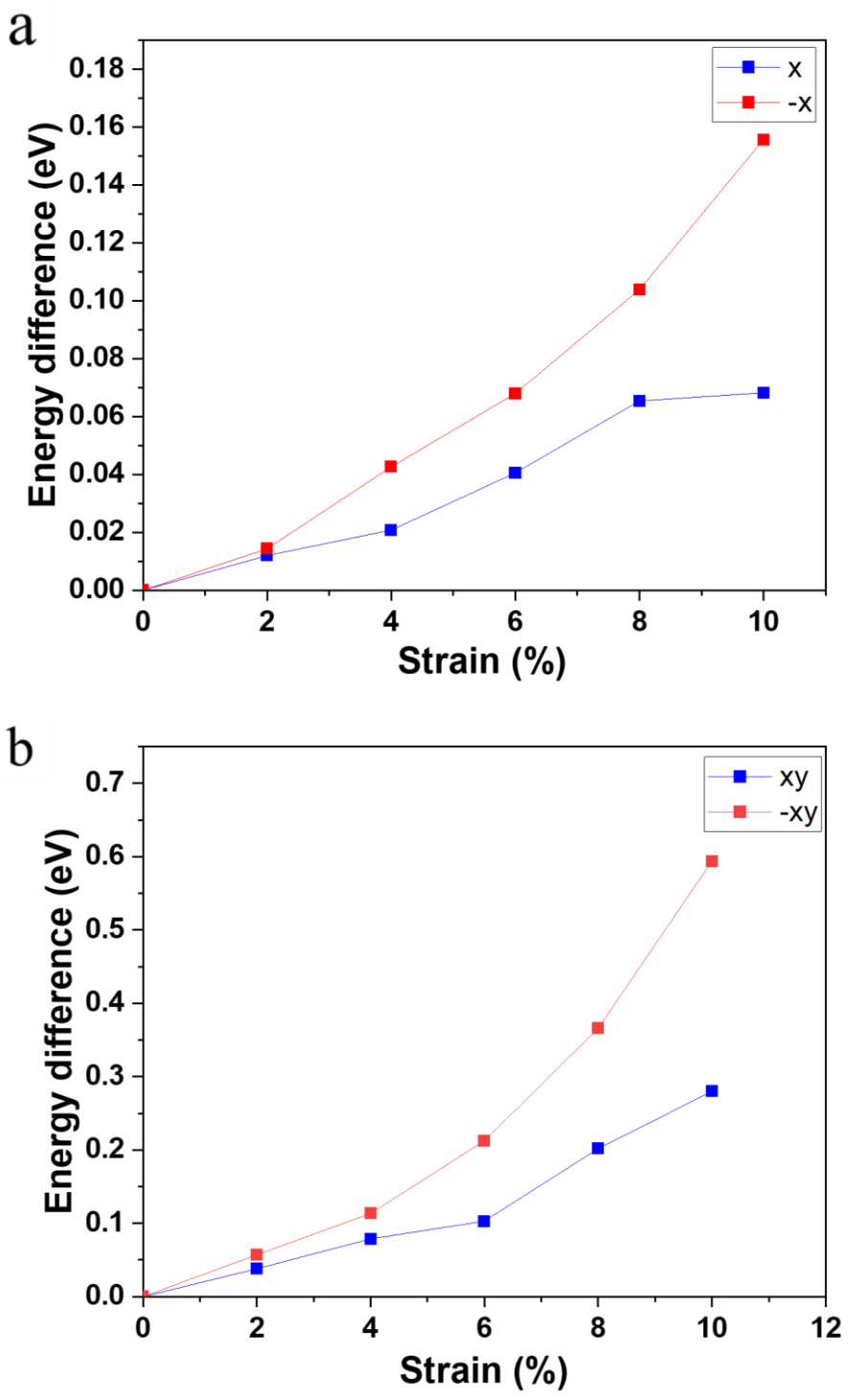

Figure 17. The single–point energies of Pd with (a) uniaxial tensile and compressive strains, and (b) biaxial tensile and compressive strains.

Under the uniaxial tensile strain, the single–point energy of Pd demonstrates an increasing trend, which is the same of the strained Pt (**Figure 17**). The 2% to 10% uniaxial tensile strain causes the energy of Pd to increase from 0 to around 0.07 eV. As mentioned above, the enhancement of energy represents the instability of the material under the structural and geometric conditions. In contrast, the uniaxial compressive strain also results in a more significant enhancement in single–point energy. Under uniaxial compressive strain, the energy of Pd increases from 0 to around 0.16 eV.

Compared to the ripple–induced Pd, the strain–induced Pd is more stable. The 10% uniaxial tensile strain causes an overall increase of around 0.7 eV to the single–point energy, which is significantly lower than the enhancement in energy by ripple induction. The lower enhancement of energy represents stability of strained Pd than that of rippled Pd.

The enhancement in energy of Pd with biaxial tensile strain is higher than the Pd with uniaxial tensile strain. The 2% biaxial tensile strain enhances the single–point energy of around 0.05 eV, and then the 4% biaxial tensile strain enhances the single–point energy of around 0.075 eV. After the strain reach 6%, the single–point energy increases to around 0.1 eV. The 8% biaxial tensile strain causes a more obvious increase in single–point energy, which causes the increase of around 0.1 eV from the 6% biaxial tensile strain. Once the tensile strain up to 10%, single–point energy reaches a maximum of around 0.275 eV. Compared to Pt, the single–point energy of Pd is more sensitive to tensile strain.

Meanwhile, biaxial compressive strain causes a more remarkable increase in single–

point energy. Under the 2% to 10% biaxial compressive strain, the single–point energy difference is 0.05, 0.1, 0.2, 0.35, and 0.6 eV, respectively. The increasing trend of the single–point energy caused by biaxial compressive strain is the same of Pt, where the single–point energy of Pd is less sensitive to the compressive strain than that of Pt.

Compared to uniaxial tensile strain, biaxial tensile strain causes a higher enhancement of single–point energy than the enhancement of the single–point energy caused by uniaxial tensile strain. Biaxial tensile strain causes a more significant deformation to the surface of Pd, resulting in a larger elongation of the bond length, and further reducing the stability of the structure of Pd. Additionally, the biaxial tensile strain also causes a lower increase in the single–point energy compared to the ripple effect.

3.3.2.2 The work function of strained Pd

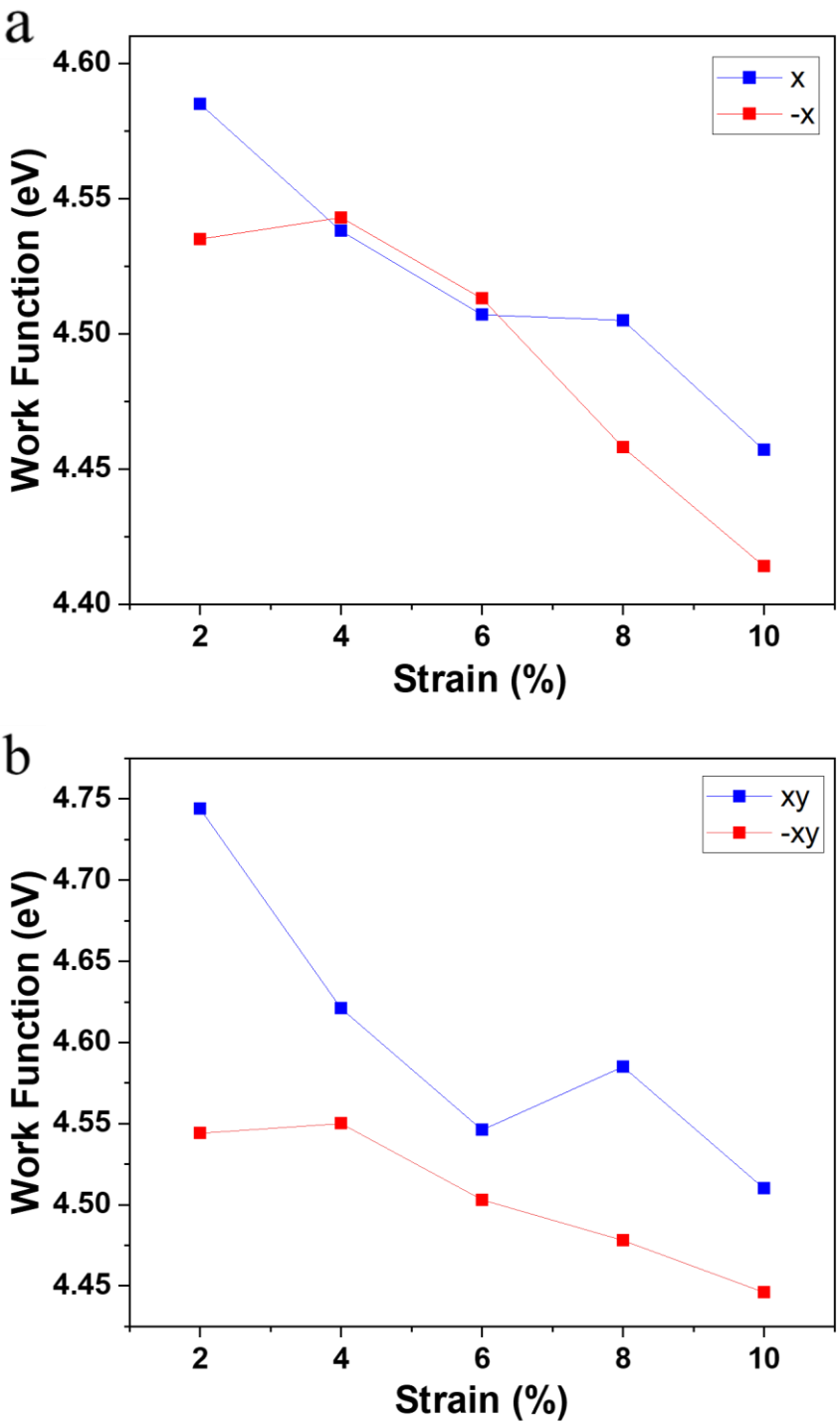

Figure 18. The work functions of strained Pd with (a) uniaxial and (b) biaxial tensile and compressive strains.

The WF change of Pd under uniaxial strain and biaxial strain shows an overall reducing trend. Under the 2% to 10% uniaxial tensile strain, the WF of Pd reduces from around 4.58 eV to 4.45 eV (**Figure 18a**). The reduction of WF almost remains linear, except for the 8% uniaxial tensile strain, where the WF of Pd slightly increases and deviates from the predicted range. Under the uniaxial compressive strain, some points of the WF of Pd also deviate from the predicted range. The induction of 4% uniaxial compressive strain causes a slight increase in the WF, which is higher than that 2% uniaxial compressive strain by around 0.01 eV. After that, the WF demonstrates a reducing trend, which reduces from 4.54 eV to 4.51 eV.

The induction of biaxial strain also leads to a similar result of uniaxial strain on the WF of Pd (**Figure 18b**). The 2% to 6% biaxial tensile strain causes the WF of Pd to reduce to around 4.75, 4.625, and 4.55 eV, respectively. However, the biaxial tensile strain increases the WF from around 0.05 eV to 4.6 eV, which deviates from the reducing trend. On the other hand, the 4% biaxial compressive strain also results in a slight enhancement in the WF. From the 4% biaxial compressive strain, the 6% to 10% biaxial compressive strain causes the overall 0.01 eV reduction of WF of Pd.

Compared to the difference between uniaxial and biaxial strain, these strains result in the same reduction in WF. The result of the 8% tensile strain deviates from the expected range, whereas the 4% compressive strain deviates from the predicted range. Although some points deviate from the expected range, other points show that the strain is useful in modifying the WF of Pd. Compared to the overall reduction of WF, the ripple is more effective in tuning the WF of Pd; however, the strain is more flexible than the ripple in tuning the WF. These strains can be chosen according to the demand and desire.

3.3.2.3 The PDOS of the d orbital of strained Pd

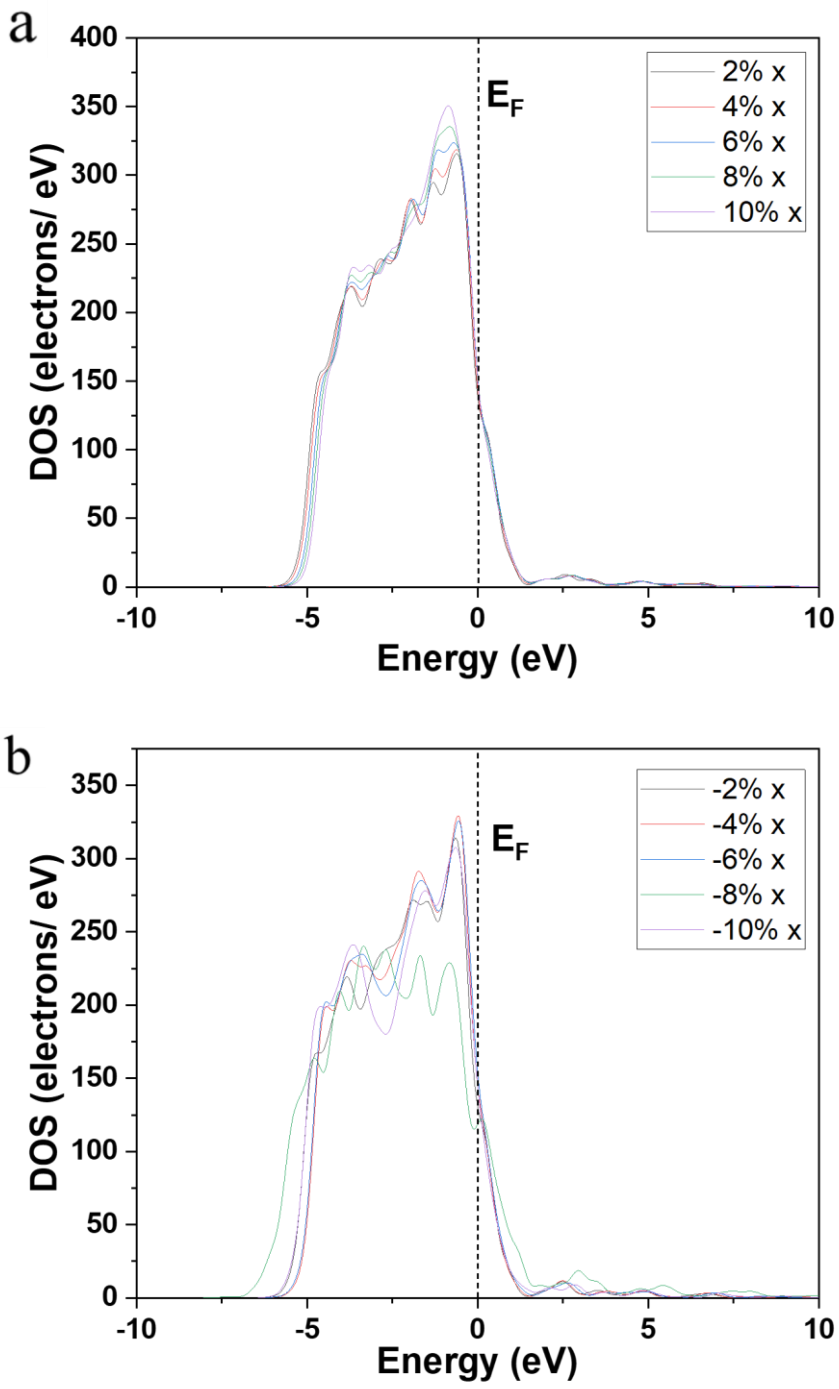

Figure 19. The PDOS of the d orbital of Pd with 2 to 10% uniaxial (a) tensile strain, and (b) compressive strain.

With uniaxial tensile strain, the PDOS of the d orbital of Pd shows two changes, where these changes are located at around –1 eV and –4 eV (**Figure 19a**). At these locations, the peak intensity demonstrates the increasing trend along with the increase in uniaxial tensile strain. Compared to the peaks located at –4 eV, the peaks located at –1 eV show more obvious changes with the tensile strain, where the peaks are located near 0 eV. The peak located at around –1 eV increases with the increase in tensile strain, which increases from around 275 electrons/eV to the highest of around 350 electrons/eV with the 10% uniaxial tensile strain.

In contrast, the DOS of uniaxial compressive strain is unpredictable than uniaxial tensile strain (**Figure 19b**). The peak located at around –2.5 eV is the major change of whole structure. Along with the increase of uniaxial compressive strain, the peak intensity gradually reduces, except for the 8% uniaxial compressive strain. Moreover, the maximum of DOS under uniaxial compressive strain is around 325 electrons/eV.

In addition, the left side of the PDOS slightly moves towards the Fermi level with the increase of uniaxial tensile strain. The change of peak intensity, peak height, and the left side of the PDOS affect the electronic structure of the strained Pd and change the area of the PDOS. For the compressive strain, the unpredictable structural changes cause the uncontrollable electrocatalytic properties of Pd.

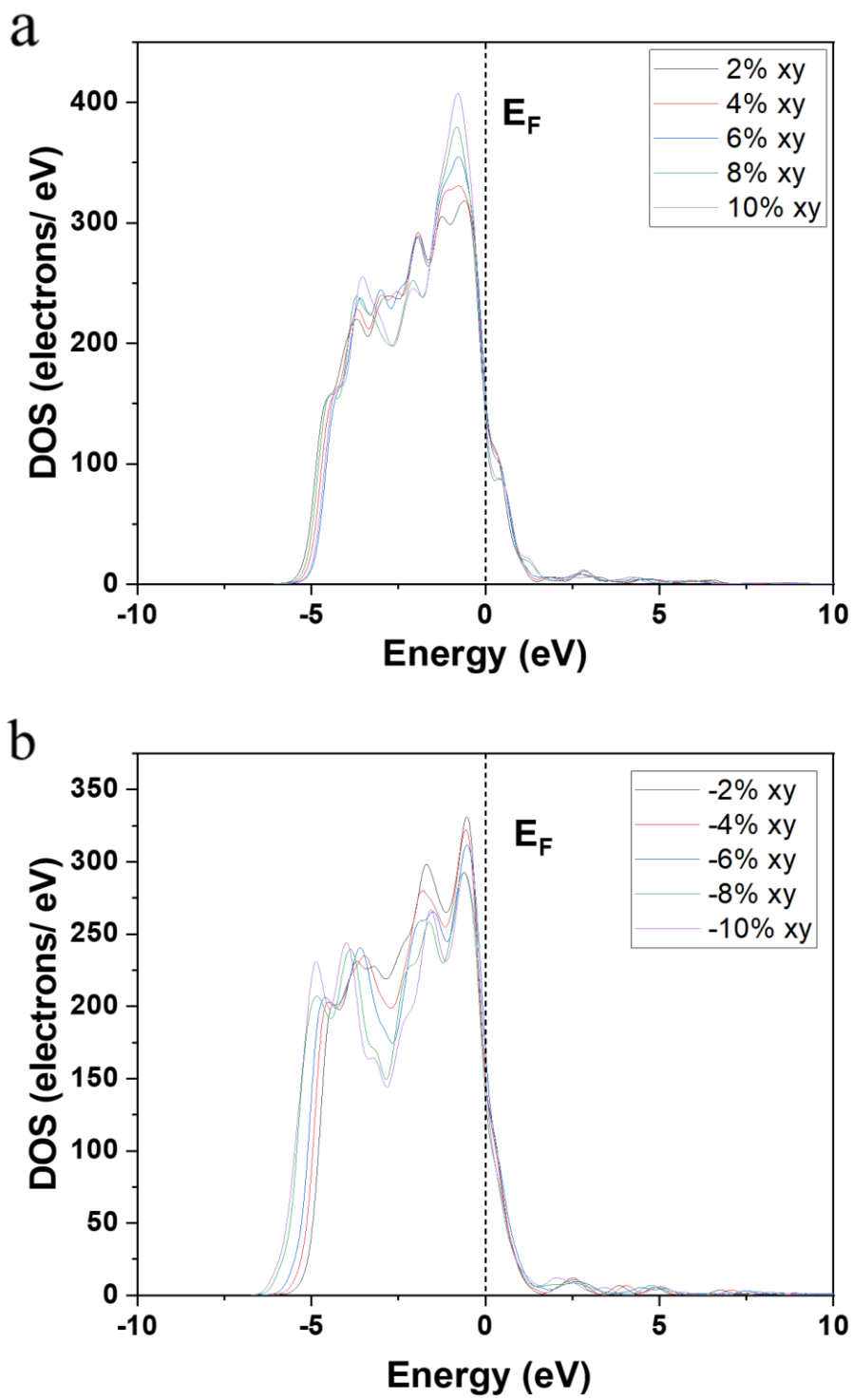

Figure 20. The PDOS of the Pd-4d orbitals with 2 to 10% biaxial (a) tensile strains, and (b) compressive strains.

The changes of PDOS in d–orbitals of Pd with 2% to 10% biaxial tensile strain are

similar to Pd with 2% to 10% uniaxial tensile strain, where the peak intensity change is more obvious (**Figure 20**). The major changes are located between –5 to –2.5 eV and near the Fermi level. For the peak located at around 0 eV, the peak intensity enhances with the enhancement of biaxial tensile strain, where the maximum of the DOS peak reaches around 400 electrons/eV with 10% tensile strain. For the peak located between 5 to –2.5 eV, the peak intensity is disproportionate to the strength of strain, where the minimum of the peak reaches around 200 electrons/eV with 10% tensile strain.

On the other hand, the DOS shows a reasonable structure and obvious change with biaxial compressive strain. The enhancement of biaxial compressive strain causes the left side of the whole DOS to shift away from the Fermi level. The peak near the Fermi level demonstrates a slight change, where the enhancement of compressive strain causes the reduction of peak intensity. The peak height reduces from around 325 electrons/eV to around 275 electrons /eV under the 2% to 10% biaxial compressive strain. In addition, the "concave" is located at around –2.5 eV, where the "concave" becomes obvious when biaxial compressive strain is increased.

The structural change of DOS under uniaxial strain is less obvious than biaxial strain, and the change pattern is reasonable. In addition, the reduction of the peak height and the shifting of the left side of DOS gradually lower the probability of electrons located near the Fermi level, which influences the d–band center and then affects the electrocatalytic property of Pd under the biaxial strain.

3.3.2.4 The d–band center of strained Pd

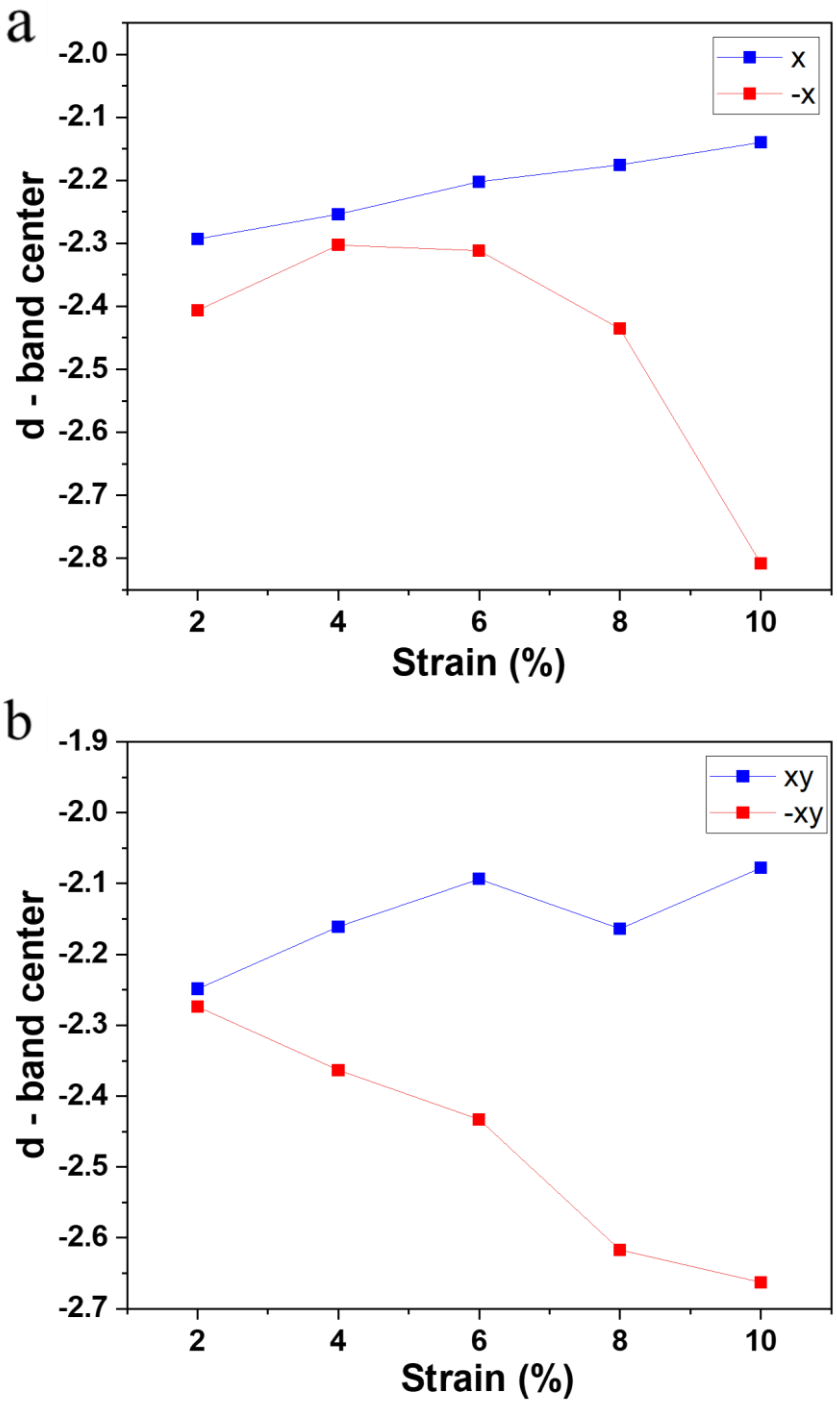

Figure 21. The d–band center trends of Pd changed with the (a) uniaxial tensile and compressive strains, and (b) biaxial tensile and compressive strains.

The uniaxial tensile strain is effective in changing the structure of Pd and then improving the d–band center (**Figure 21**). Under the 2% to 10% uniaxial tensile strain, the d–band center of Pd enhances from –2.29 to –2.14 eV. The enhancement of d–band center is relatively linear, which implies that the improvement of d–band center is stable. However, uniaxial compressive strain causes the unreasonable trend, where the 4% strain enhances the d–band center, and then the d–band center is gradually shifted away from the Fermi level by the higher compressive strain. The uniaxial compressive strain causes the overall reduction of the d–band center of around 0.4.

The biaxial tensile strain transfers the d–band center toward the Fermi level, whereas the biaxial compressive strain transfers the d–band center away from the Fermi level. The 2% to 10% biaxial tensile strain transfers the d–band center from around –2.35 to around –2.05, where the 2% to 10% biaxial compressive strain transfers the d–band center from around –2.35 to around –2.7 eV. For the biaxial strain, only the point of 8% strain deviates from the reasonable range.

Compared to the ripple–induced Pd, the relatively increasing d–band center shows the stability of strain engineering over ripple engineering. Same with Pt, the d–band center on the surface of strained Pd is identical. The random collisions of the reactant with the surface of strained Pd cause the same result, and then avoid the uncertainty caused by the ripple effect.

Chapter 4

The surface strain and ripple effect on the surface of transition metal chalcogenide

4. The surface strain and ripple effect on the surface of transition metal chalcogenide

4.1 The brief introduction and background of MoS_2 and $MoSe_2$

Transition metal chalcogenide (TMC) is a type of standard raw material for the electronic, optoelectronic counterparts. The surface strain effect uniformly changes the interatomic distance and the surface area. The previous studies and research proved that the strain effect effectively changes the properties of LD TMC and other semiconductors, including electrical conductivity, piezoelectric properties, optoelectrical properties, magnetic properties, and other properties.

Besides the surface strain effect, the ripple effect also change the properties of the LD TMC and other LD semiconductors. The ripple effect partially changes the thickness of LD TMC and other materials, causing the partial 2D and partial 3D thickness on the surface of the LD materials. Compared to TM, the property change of TMC caused by the strain and ripple effect is determined by countless efforts. The calculated results of TMC are compared to TM, and then this thesis will attempt to explain the difference between TMC and TM.

In the Chapter 4, MoS_2 and $MoSe_2$ are chosen as the target to investigate the ripple and the strain effect on the TMC. MoS_2 and $MoSe_2$ are the common TMCs with a sandwich–like structure in each layer: one TM atom located between two chalcogenide atoms. Besides, the combination of metal atom (conductor) and chalcogenide atom (insulator) brings the semiconducting property to them. Both are important materials with specific

properties and applications in different fields.

MoS_2 possesses the hexagonal layer structure, which is like that of graphite. The number of layers influences the electricity, which directly affects the electronic and optoelectronic applications. Moreover, MoS_2 possesses high thermal and chemical stability. It can retain its lubricating properties and avoid degradation under high temperatures. The chemical inert property and oxidation resistance bring high durability to MoS_2. Furthermore, the mechanical strength expands the application of MoS_2 for preparing robust materials. Besides, the catalytic property of MoS_2 involves lots of reactions in the chemical industry, such as HER, hydrodesulfurization. In addition, MoS_2 possesses biocompatibility and specific surface properties, which can be used for biomedical applications, such as biosensors and drug delivery. Owing to the direct band gap, MoS_2 is commonly used as a photoluminescent material, such as the LEDs and solar cells. For energy storage, MoS_2 is being studied for batteries and supercapacitors.

$MoSe_2$ is another common TMC that is generally applied for the energy storage, optoelectronics, and electronics. As one of the common types of TMC, $MoSe_2$ also possesses the layer structure, semiconducting properties, and excellent chemical stability. Owing to these advantages, $MoSe_2$ is generally applied in batteries, supercapacitors, catalysts, solar cells, and other relevant applications. The studies of MoS_2 and $MoSe_2$ benefit the development of nanotechnology, renewable energy, and flexible electronics. The further development of TMC facilitates the miniaturization and improvement of the nanoelectronics component. Moreover, TMC plays a critical role of the renewable energy technology, which can assist in improving the efficiency of these techniques. Furthermore, the unique mechanical properties bring a large potential

of TMC to create flexible electronic components.

These TMCs possess numerous potentials in different fields, and it is believed that more and more applications of these materials have not been explored in now. The ripple and strain effect will assist in exploring the potential and expanding the applications of TMCs.

4.2 The ripple effect on the surface of transition metal chalcogenide

The 2D semiconductors, such as TMC, graphene, MXenes, and other semiconductors, are unstable due to out–of–plane strain. [120] The strain includes the thermal change from the CVD, the mechanical stretching and bending, doping, defects, and other possible sources. These sources induce stress and then modify the crystal structure of the 2D semiconductor. To stabilize the crystal structure after the strain induction, the ripple is formed to release the extra energy induced by the strain.

In case the strain formation is unpredictable, the ripple formation is also unpredictable due to the unknown source of strain. As a result, investigating the ripple effect of the TMC is essential for an in–depth understanding of how the TMC's properties change and to study the relationship between the ripple and property for tuning properties through ripple induction.

4.2.1 The single–point energy of MoS_2 and $MoSe_2$

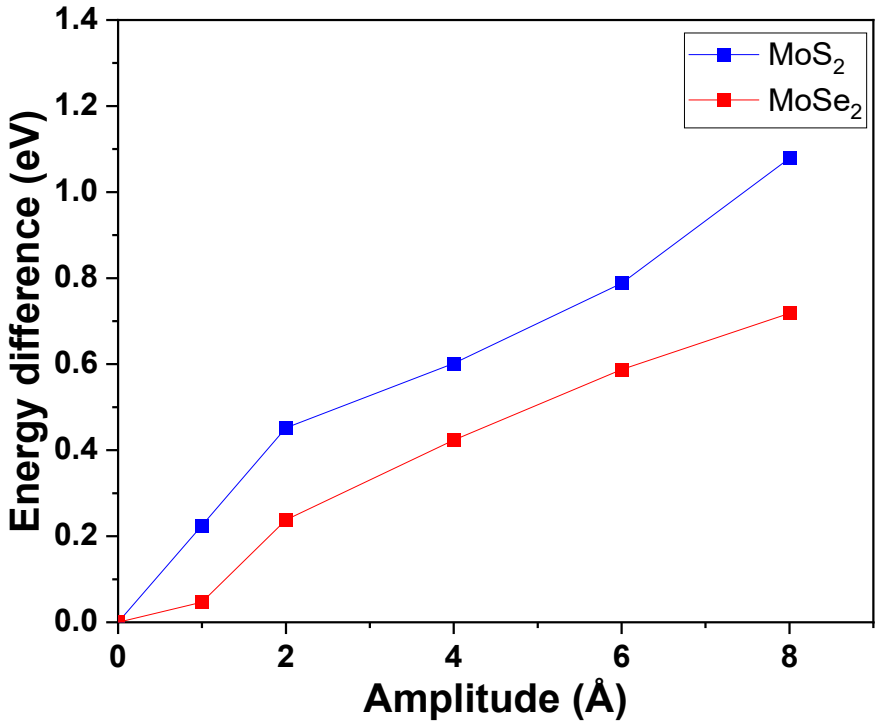

Figure 22. The single–point energy changes of MoS_2 and $MoSe_2$ with different amplitudes of ripple.

The single–point energy of MoS_2 increases with the increase in the amplitude of the ripple (**Figure 22**). The 1 Å height of the ripple slightly increases the single–point energy of around 0.2 eV. The 2 Å height of ripple causes the single–point energy to increase by around 0.25 eV from the 1 Å height of ripple. Under the 4 Å height of ripple, the single–point energy reaches 0.6 eV. And then, the 6 Å height of ripple further increases the single–point energy of MoS_2 to around 0.8 eV. Finally, the single–point energy of MoS_2 is around 1.1 eV under the 8 Å height of the ripple.

Under the ripple effect, the single–point energy of $MoSe_2$ demonstrates the increasing

trend. The 1 Å of ripple increases the single–point energy of each $MoSe_2$ atom by around 0.05 eV. The 2 and 4 Å of ripples cause the more significant increase, which increases the single–point energy by around 0.2 eV. The 6 Å of ripple increases the energy difference from the no–rippled $MoSe_2$ of around 0.6 eV. Finally, the 8 Å of ripple causes the overall increase of single–point energy of around 0.7 eV.

The overall increase of single–point energy of MoS_2 is higher than $MoSe_2$, which implies that the stability of MoS_2 is lower than $MoSe_2$ with the ripple induction. The single–point energy depends on different factors, including geometry and elasticity. In this case, MoS_2 is more against the deformation from the ripple induction than $MoSe_2$. The more unstable of MoS_2 implies that the ripple is more effective in tuning the properties of MoS_2 than $MoSe_2$. In addition, the overall increase in the single–point energy of TMC is less than the increase in the single–point energy of TM. The stability of rippled TMC is higher than that of rippled TM, which implies that TMC is less sensitive to the ripple than TM.

4.2.2 The work function of MoS_2 and $MoSe_2$

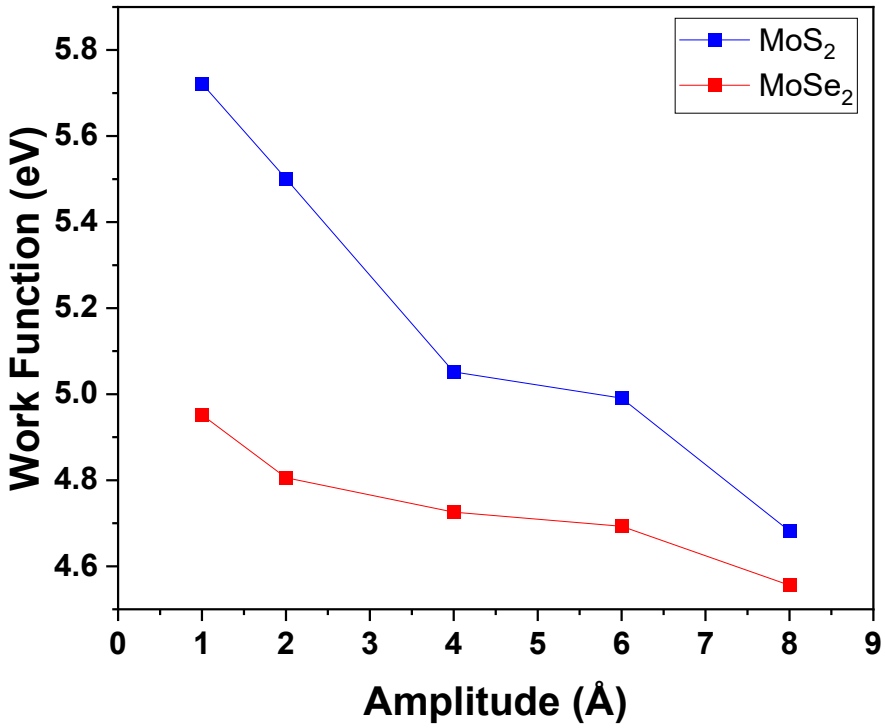

Figure 23. The work functions of MoS_2 and $MoSe_2$ with different amplitudes of ripple.

With the induction of 1 Å to 8 Å of ripple, the WF of MoS_2 and $MoSe_2$ demonstrates a reduction trend (**Figure 23**). Under the 1 Å of ripple, the WF of MoS_2 is around 5.7 eV. The 2 Å of ripple cause the WF of MoS_2 to reduce to around 5.5 eV. The 1 to 4 Å height of ripple causes a relatively linear reduction of WF, and the WF reaches around 5.05 eV with 4 Å height of ripple. However, the 6 Å height of the ripple only reduces the WF to around 5 eV. Finally, the 8 Å height of ripple reduced the WF of MoS_2 to around 4.7 eV.

Compared to the reduction of WF of MoS_2, the reduction of WF of $MoSe_2$ is relatively gentle. Under the 1Å to 8Å of ripple, the WF of $MoSe_2$ reduces to around 4.95, 4.8,

4.71, 4.7, and 4.55 eV, respectively. The ripple causes the overall reduction of the WF of around 0.4 eV.

WF induction of ripple reduces the WF of MoS_2 and $MoSe_2$, effectively reduces the WF, and then improves the ability of electrons to move on their surface of. The reduction trend indicates that the ripple enables tuning the ability of the movement of electrons during the electrocatalytic activity. The lower WF represents that the electrons can move more easily to move away from the surface of the TMC. In other words, besides the electrocatalysis, the rippled TMC can be applied to different fields, such as an electron emitter.

For the single-point energy and work function trends under the ripple, the TM has higher sensitivity than the TMC. The difference results from several factors, including the structural differences, the bonding nature, and the electronic structure sensitivity. TMC is a layered, van der Waals–bonded material. In each layer, the in–plane covalent bonding is strong, whereas the out–of–plane van der Waals interaction is weak. Therefore, the TMC is more flexible, which can accommodate ripples without a noticeable break to the in–plane bonding structure. On the other hand, TM possesses a metallic and close–packed structure, which results in strong metallic bonding in all directions. As a result, TM is less tolerant to out–of–plane deformation, and the ripple can relatively easily alter the metallic bonding structure. Besides, the electronic property difference between TMC and TM also leads to the sensitivity difference. The electronic properties of TMC is mainly determined by the in–plane atomic arrangement while the out–of–plane ripples have a relatively minor effect. In contrast, owing to the delocalized nature of metallic bonding, the electronic property of TM is susceptible to

atomic positions. The introduction of ripples significantly changes the atomic positions, which alter various electronic properties. Thus, even a small out–of–plane distortion strongly influences the surface state and catalytic activity of TM.

4.2.3 The band structures of MoS_2 and $MoSe_2$

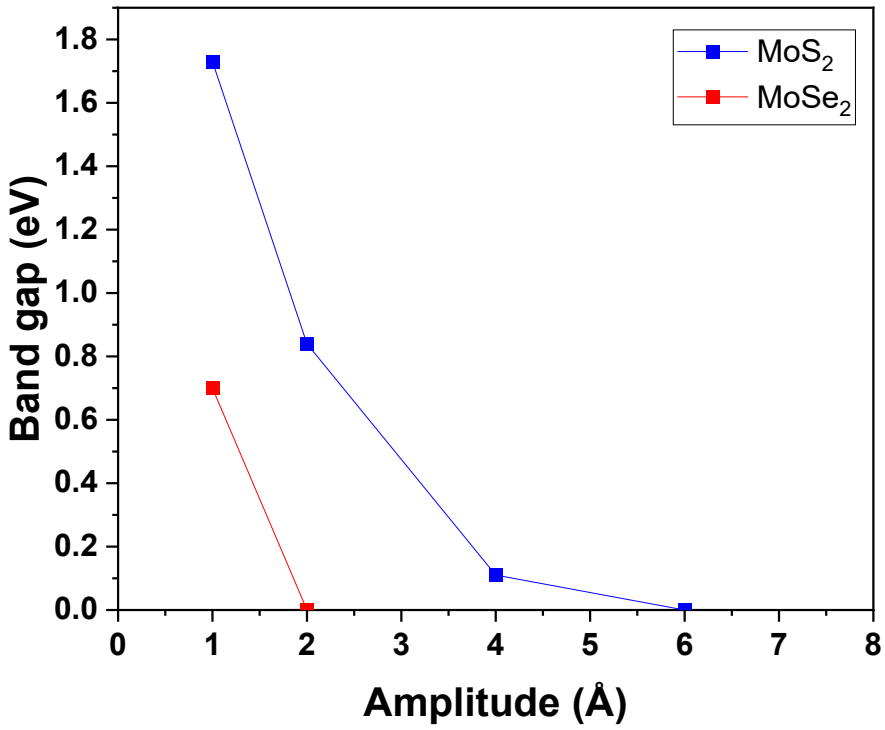

Figure 24. The band gaps of MoS_2 and $MoSe_2$ under the 1 Å to 8 Å height of ripple.

The band gap of MoS_2 shows a reduction trend with the increase of the amplitude of the ripple (**Figure 24**). Under the 1 Å height of ripple, the band gap of MoS_2 is around 1.75 eV. The 2 Å height of ripple greatly reduces the band gap of MoS_2 to around 0.8 eV. Moreover, the 4 Å height of the ripple further lowers the band gap to around 0.1 eV. Finally, the 6 Å height of ripple completely lowers the band gap of MoS_2 to 0 eV.

Under the 1 Å height of ripple, the band gap of $MoSe_2$ is around 0.7 eV. The ripple induction significantly tunes the band gap of $MoSe_2$, where the 2 Å and higher height of ripple directly reduces the band gap of $MoSe_2$ to zero. The zero–band gap implies that the electric conductivity of $MoSe_2$ is equal to that of a metal, where it can be applied for the electric component according to the electrical conductivity demand.

The result from the graph shows different sensitivities to the ripple. The reduction of the band gap demonstrates the effectiveness of ripple to modify the band gap of MoS_2 and $MoSe_2$. Considering the results of single–point energy, WF, and the band gap, MoS_2 demonstrates a higher sensitivity to the ripple effect than $MoSe_2$. Compared the bond length of Mo–S and Mo–Se, the MoS_2 has a shorter Mo–S bond (~2.4 Å) than the Mo–Se bond in $MoSe_2$ (~2.5 Å). In general, the shorter bond length implies that the bonding is stronger, and the crystal lattice is stiffer. In this case, MoS_2 is more rigid than $MoSe_2$, and it is less able to accommodate the distortions without obvious changes in electronic structures. When a ripple is introduced onto the surface, the bond lengths and angles of MoS_2 undergo a more significant perturbation, which causes the more obvious change in the single–point energy, WF, and the band gap. Besides the bond lengths, the interlayer van der Waals force strengths, atomic masses, and the electronic structure differences are also causes the difference in sensitivity to the ripple of MoS_2 and $MoSe_2$.

Owing to the smaller size and higher polarizability of sulfur atoms, the interlayer van der Waals interactions of MoS_2 are stronger than those of $MoSe_2$. As a result, the out–of–plane deformation from the ripple more easily induce strain across multiple layers. On the other hand, the weaker van der Waals interactions in $MoSe_2$ cause the easy deformation of each layer, which distributes the strain and weakens the ripple effect in

$MoSe_2$. Moreover, the sulfur atom is lighter than the selenium atom, which affects the lattice dynamics during the ripple introduction. The lighter atom implies that the whole lattice will be more sharply affected by the ripple, resulting in greater changes in electronic structure than in $MoSe_2$. Furthermore, the shorter Mo–S bond causes a larger orbital overlap and band gap in MoS_2 than in $MoSe_2$. The electronic structure of MoS_2 is more sensitive to the changes in bond length and angle; therefore, the rippling leads to greater shifts in band edge positions and WF. The bond length difference leads to the sensitivity difference of MoS_2 and $MoSe_2$. The result between MoS_2 and $MoSe_2$ can be applied as a reference for studying different TMC and other semiconductors.

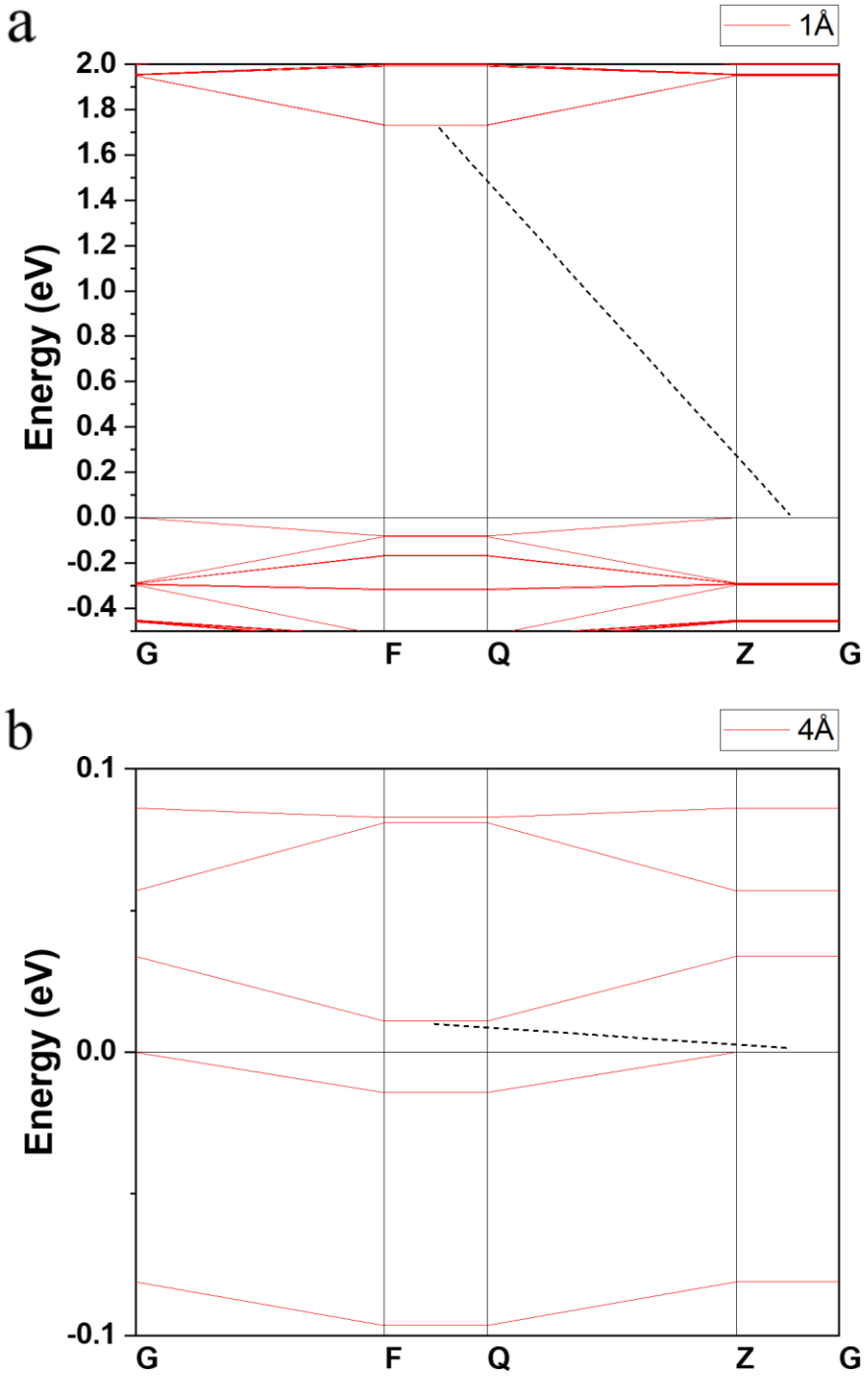

Figure 25. The band structures of MoS_2 under the (a) 1 Å and (b) 4 Å height of ripple.

In this case, the band gap of MoS_2 with 6 Å height of ripple reaches 0 eV. As a result, the analysis of the band structures focuses on the MoS_2 with 1 Å and 4 Å ripples.

Under the 1 Å of ripple, the top of the valence band locates at the region between Z and G, whereas the bottom of the conduction band locates at the region between F and Q (**Figure 25a**). The top of the valence band and bottom of the conduction band are located at different regions, which implies that the MoS_2 possesses an indirect band gap under 1 Å of ripple. Once the ripple increases to 4 Å, the band gap is closed to 0 eV, and the top of the valence band and the bottom of the conduction band are located in the same region (**Figure 25b**). Under the 4 Å of ripple, MoS_2 still retains the indirect band gap.

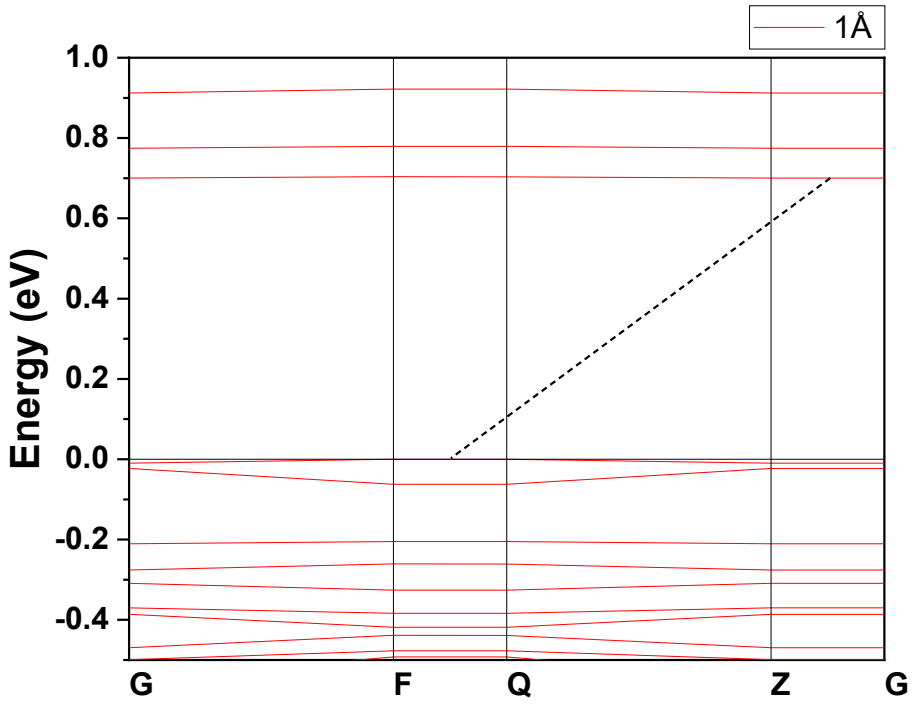

Figure 26. The band structure of $MoSe_2$ under 1 Å of ripple.

As the band gap of $MoSe_2$ becomes zero under the 2 Å and the higher height of ripple,

only the band structure under the 1 Å of ripple is analysed (**Figure 26**). Under the ripple induction, the top of the valence band is located between the F and Q regions, where the bottom of the conduction band is located between the Z and G regions. In other words, the band structure of $MoSe_2$ under the ripple induction is an indirect band gap.

Although the ripple induction successfully tunes the band gap of $MoSe_2$, the $MoSe_2$ undergoes a direct–to–indirect transition, and then the band shifts away from the original location. The indirect band gap causes the difficulty of the luminescence application for the rippled MoS_2 and $MoSe_2$, unless the extra crystal momentum is supplemented from another source.

4.2.4 The DOS change of MoS_2 and $MoSe_2$

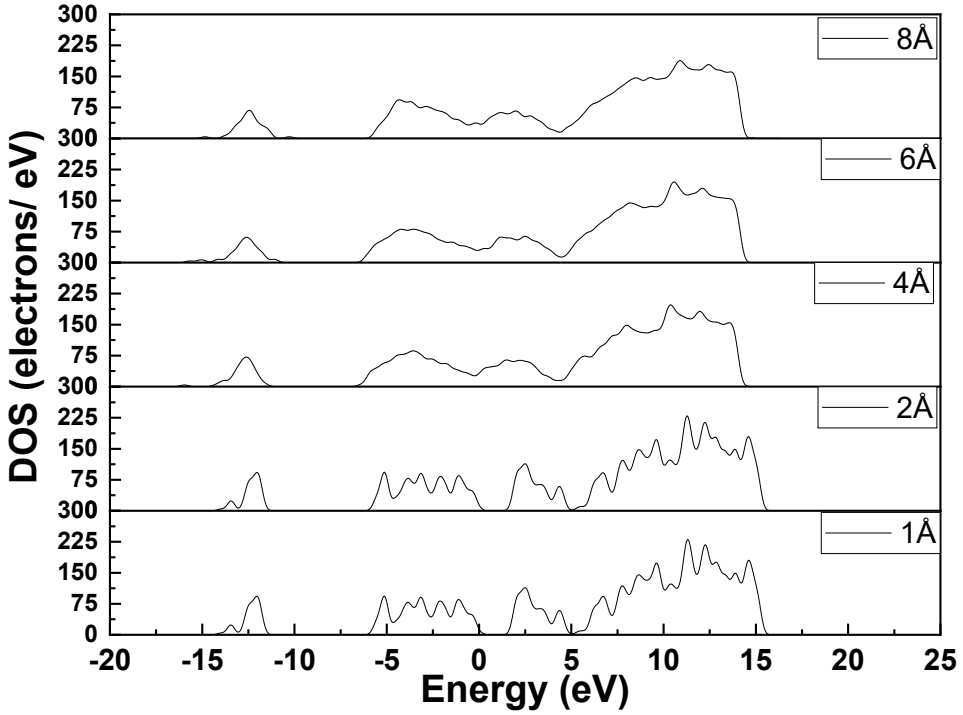

Figure 27. The DOS changes of MoS_2 under the 1 Å to 8 Å height of ripple.

The ripple induction changes the structure of the DOS of MoS_2, where the peak distribution, intensity, and structure show different variations (**Figure 27**). At the location between –15 to –10 eV, the peak intensity gradually reduces with an increase in the amplitude of the ripple. In addition, the peak between –5 to 0 eV, the ripple causes the dispersed distribution of the peak and then reduces the peak intensity. The same condition also appears at the location between 0–15 eV.

The peak change implies that the electrons at lower energy level transfer to higher energy level. The electron distributions affect the binding between the surface of TMC and the reactant intermediate.

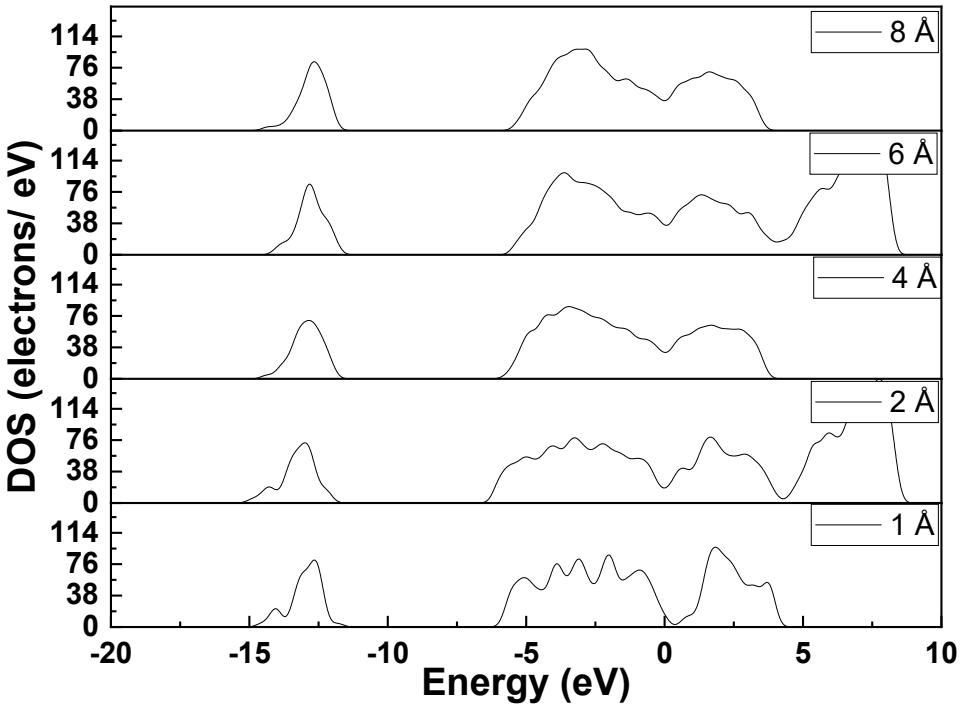

Figure 28. The DOS changes of $MoSe_2$ under the 1 Å to 8 Å height of ripple.

The ripple induction obviously changes the distribution, structure, and intensity of the

DOS (**Figure 28**). The change of the DOS is located in different regions, which focus on the energy between the energy of –15 to –10 eV, –5 to 0 eV, and 0 to 5 eV.

For the peak located at the energy of –15 to –10 eV, the increase in the height of the ripple gradually enhances the peak intensity, and the peak becomes more concentrated. Besides, the higher height of the ripple leads to the concentration of the peak located at the energy of –5 to 0, and then increases the peak intensity. For peaks higher than the Fermi level, the peak intensity gradually reduces, and the distribution of the peaks becomes dispersed. For the 2 Å and 6 Å height ripples, the extra peak appears at the energy of 5 to 10 eV.

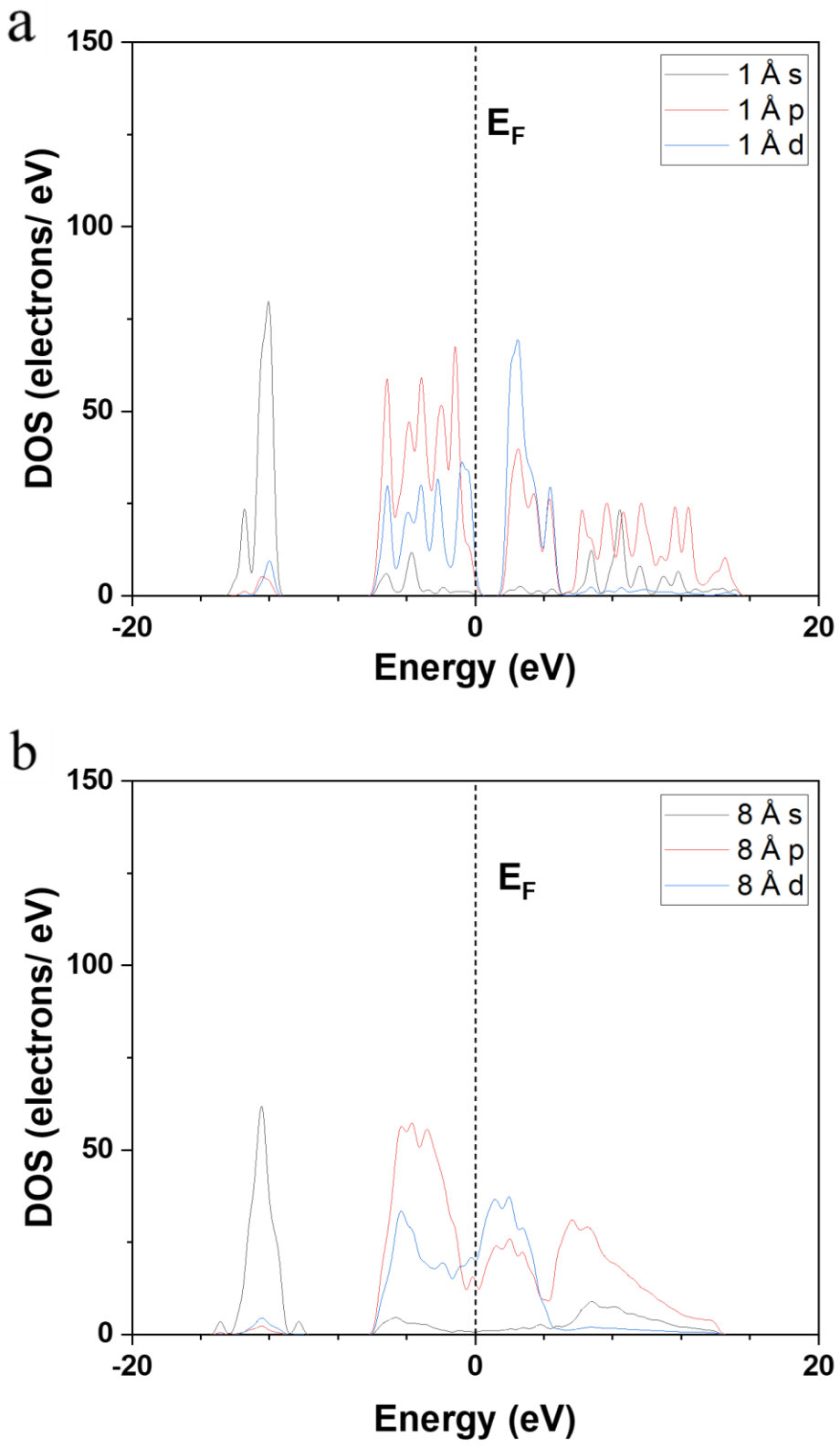

Figure 29. The PDOS of s, p, and d orbitals of MoS_2 with (a) 1Å of ripple, and (b) 8 Å of ripple.

The peak located at around –15 eV is mainly contributed by the s orbital (**Figure 29**). Under the ripple effect, the electron transfers away from the s orbital, and the peak height of this peak reduces by around 20 electrons/eV. Under the ripple induction, the peaks can be classified as different regions, including the peaks between –5 eV to 0 eV, the region between 0 eV to 5 eV, and the region after 5 eV. For the region between –5 eV to 0 eV, the peaks are mainly affected by p orbital, and d orbitals only slightly contribute to the peak changes. The condition of the region between 0 eV to 5 eV is opposite to the region between –5 eV to 0 eV. Finally, the peak changes of the region after 5 eV also contributed to the p orbital.

Under the 1 Å height of ripple, the dispersive peak distribution implies that the electrons are highly concentrated in different regions, where these regions are not continuous. Under the 8 Å height of ripple, the peak intensity reduces, and the peak becomes continuous. The structures and distributions of electrons certainly changes the electron movement and the bonding with other reactants.

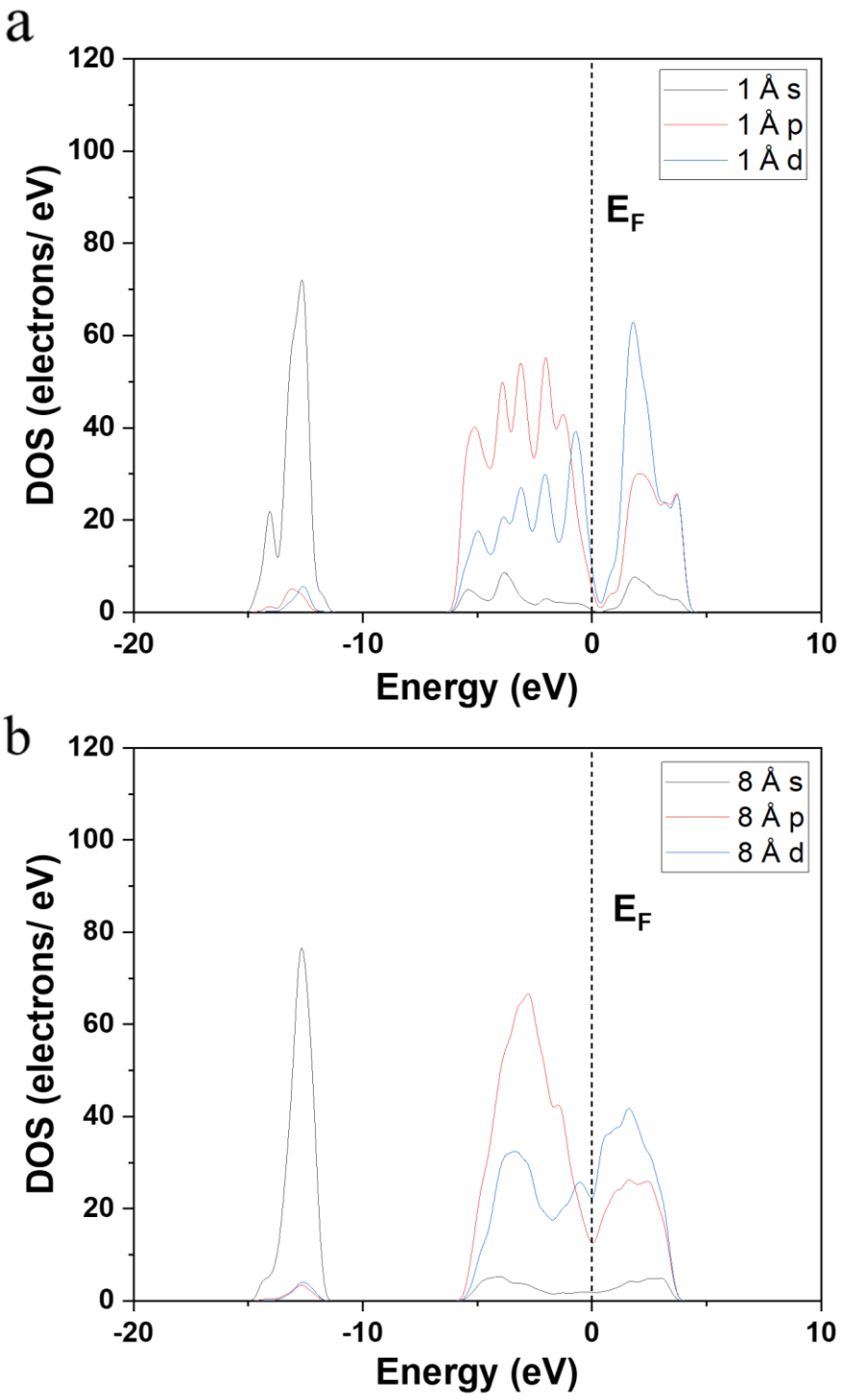

Figure 30. The PDOS of s, p, and d orbitals of $MoSe_2$ with (a) 1Å of ripple, and (b) 8 Å of ripple.

The s, p, and the d orbitals contribute to different peak changes of $MoSe_2$ under the

ripple induction (**Figure 30**). The peak located at the energy of –15 to –10 eV is attributed to the s orbital, where the ripple induction causes the electron of the s orbital to concentrate and enhance the peak intensity. For the peak located at the energy of –5 to 0 eV, the p orbital contributes to the peak change, and then the d orbital contributes to the change upper the Fermi level.

The peak alternation implies that the electron of a different orbital moves to a different space and then changes the electronic structure. The result of $MoSe_2$ is like MoS_2, where the peak intensity and distribution also show the same changes. These changes imply that the ripple induction led to similar changes to the properties of MoS_2 and $MoSe_2$.

4.3 The strain effect on the surface of transition metal chalcogenide

The out of the ordinary structural, mechanical, and physical properties of the 2D TMC and other materials have attracted the attention of different scientists. Besides, because of the enchanting electrical and thermal transport performance, these materials possess great thermal management and thermoelectric energy generation. Moreover, the high stretchability of these materials ensures that the electronic and thermal properties of 2D materials can be modified.

The strain effect is possible to be caused by uncontrollable factors, such as the thermal expansion from the temperature change, the internal stress from the lattice defect, and the undesired doping of different atoms. These uncontrollable factors induce the strain effect on the surface of TMC and thus change the property. The uncontrollable strain

induction brings about the unknown property change of the TMC.

As a result, the relationship between the strain and the property of TMC should be constructed to further understand the strain effect. The in–depth understanding will help to control the strain effect and then modulate the properties of TMC according to the demand.

4.3.1 The single–point energy difference of MoS_2 and $MoSe_2$

The energy differences and the work functions provide reliable data to indicate the stability and how easily the electron moves through the TMC. These calculation results facilitate determining the stability, the change of the morphology, and the sensitivity to the strain effect. These properties are closely related to the electronic and other properties of TMC, where they can be applied as a reference for further investigation.

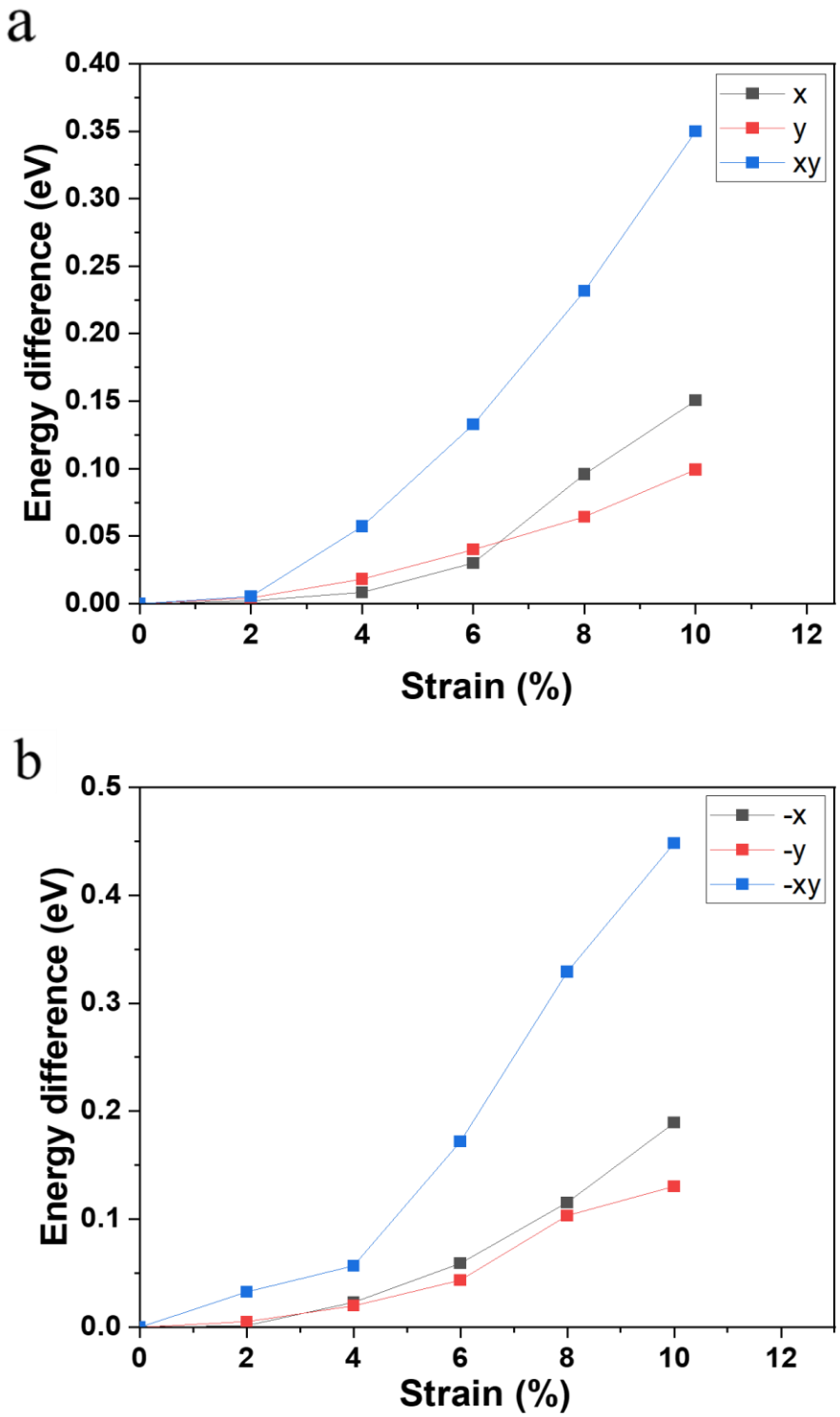

Figure 31. (a) The single–point energy difference of MoS_2 under the uniaxial tensile strain through the x–, the y–axis, and biaxial tensile strain through the x– and y–axis. (b) The single–point energy difference of MoS_2 under the uniaxial compressive strain through x–, y–axis, and the biaxial compressive strain through the x– and y–axis.

Under uniaxial tensile strain through the x– and y– axial, the single–point energy increases around 0.15 and 0.1 eV, respectively. Compared to the uniaxial tensile strain, the biaxial tensile strain increases the single–point energy of around 0.35 eV.

The uniaxial tensile strain from the x–axis is slightly effective than the uniaxial tensile strain from the y–axis to increase the single–point energy of MoS_2. Under the 2% to 6% of uniaxial tensile strain, the single–point energy increases do not have a significant change from the x– or y–axis. However, when the induced tensile strain is up to 8%, the single–point energy increases show a relatively obvious difference between x– and y–axis. After the strain up to 10%, the single–point energy with uniaxial tensile strain on x–axis is higher than the energy with uniaxial tensile strain on y–axis by around 0.05 eV. The result indicates that MoS_2 is more sensitive to the tensile strain from the x–axis than the y–axis.

On the contrast, the compressive strain causes a larger increase in the single–point energy, which implies that the compressive–strained MoS_2 is unstable than the tensile–strained MoS_2. Under the uniaxial compressive strain on the x– and y–axis, the increasing trend of single–point energy is similar. With the induction of 2% to 4% uniaxial strains, the single–point energy of MoS_2 is almost the same. Once the strain increases to 6%, the single–point energy shows a slight difference under the compressive strain on x and the y–axis. When the strain reaches 10%, the compressive strain on the x–axis causes a more obvious increase in single–point energy than the increase from the compressive strain on the y–axis. The single–point energy of MoS_2 under 10% uniaxial compressive strain on the x–axis is higher than that of MoS_2 under

10% uniaxial compressive strain on the y–axis by around 0.05 eV. Compared to the uniaxial compressive strain, the biaxial compressive strain overall increases the single–point energy of around 0.45 eV, which is higher than the combination of the uniaxial compressive strain on the x– and y–axis.

Compared to the uniaxial tensile strain from x– or the y–axis, the biaxial tensile strain increases the single–point energy of MoS_2 (**Figure 31a**). The biaxial tensile strain is more effective than the uniaxial tensile strain to increase the single–point energy of MoS_2. The interaction between x– and y–axis tensile strain causes a significant effect on the stability and geometry change of MoS_2, which is greater than the results of the direct combination of x– and y–axis. The increasing trend of the single–point energy of the biaxially compressed–strained MoS_2 is similar to the trend of the biaxially tensile–strained MoS_2. In addition, the biaxial compressive strain results in higher single–point energy, increasing due to the increase from the biaxial tensile strain. In other words, the biaxially compressed MoS_2 is more unstable than the MoS_2 with other types of strain.

From the comparison between the uniaxial tensile and compressive strain of x–, y–axis, and the biaxial tensile strain of x– and y–axis, the biaxial tensile strain is more effective in changing the structure of MoS_2, and then further modifying the property of MoS_2 (**Figure 31b**). Moreover, the biaxial compressive strain also causes an obvious increase in single–point energy, and the increase is higher than the increase caused by biaxial tensile strain. The elongation and compression from 2D further aggravate the instability of MoS_2, and the following studies of MoS_2 will be focused on the biaxial strain.

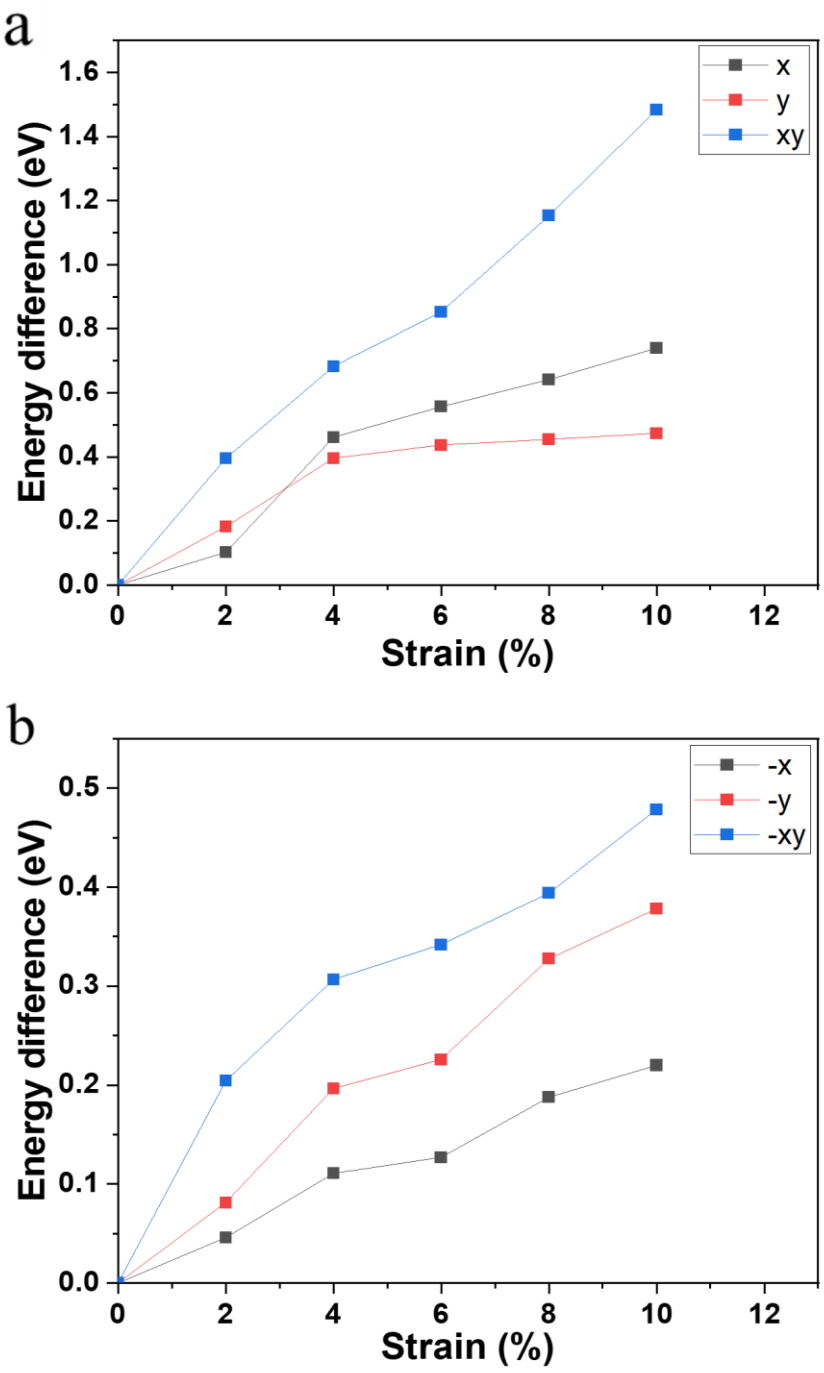

Figure 32. The single–point energy difference of $MoSe_2$ under the uniaxial tensile strain through x–, the y–axis, and the biaxial tensile strain through x– and the y–axis. (b) The single–point energy difference of $MoSe_2$ under the uniaxial compressive strain through x–, the y–axis, and the biaxial compressive strain through x– and the y–axis.

With the 2% uniaxial tensile strain on the x– and y–axis, the single–point energy has an increase by around 0.1 eV (**Figure 32a**). After the uniaxial tensile strain up to 4%, the single–point energy increases to around 0.4 eV, where the strain from the x–axis causes a slightly higher increase in single–point energy. Along with the increase in uniaxial tensile strain, the difference in single–point energy between the x and y–axis becomes more significant, where the x–axis causes a larger increase in single–point energy. The biaxial tensile strain further increases the single–point energy, which is larger than the combination of the uniaxial strain from x– and the y–axis. The 2% to 10% biaxial tensile strain causes the increase of single–point energy of 0.4, 0.7, 0.8, 1.2, and 1.5 eV, respectively.

In contrast, the uniaxial compressive strain causes less increase in single–point energy compared to the tensile strain (**Figure 32b**). Different from the tensile strain, the single–point energy demonstrates a higher sensitivity to the compressive strain from the y–axis than the compressive strain from the x–axis. The 10% uniaxial compressive strain on the x–axis causes an increase in the single–point energy of around 0.2 eV, whereas the 10% uniaxial compressive strain on the y–axis causes an increase in the single–point energy of around 0.35 eV. The biaxial compressive strain also causes a larger increase in single–point energy than the uniaxial compressive strain. The 2% to 10% biaxial compressive strain causes the increase of single–point energy of around 0.2, 0.3, 0.35, 0.4, 0.45 eV, respectively.

Although the tensile and compressive strains also increase the single–point energy of $MoSe_2$, there are some differences between MoS_2 and $MoSe_2$ under different types of strain. For the tensile strain, the uniaxial and biaxial tensile strain cause a more

significant and obvious increase in the single–point energy, which implies that the single–point energy of $MoSe_2$ is more sensitive to the tensile strain than that of MoS_2. For the compressive strain, the single–point energy of MoS_2 is more sensitive to the tensile strain on the x–axis, where $MoSe_2$ shows the opposite result. Same with MoS_2, the induction of biaxial tensile and compressive strain significantly changes the structure of $MoSe_2$ and then causes the instability of the strained $MoSe_2$. However, the instability brings more and more property changes to MoS_2 and $MoSe_2$. As a result, the following investigation of the property changes of MoS_2 and $MoSe_2$ will focus on the biaxial strain.

4.3.2 The work function of MoS_2 and $MoSe_2$

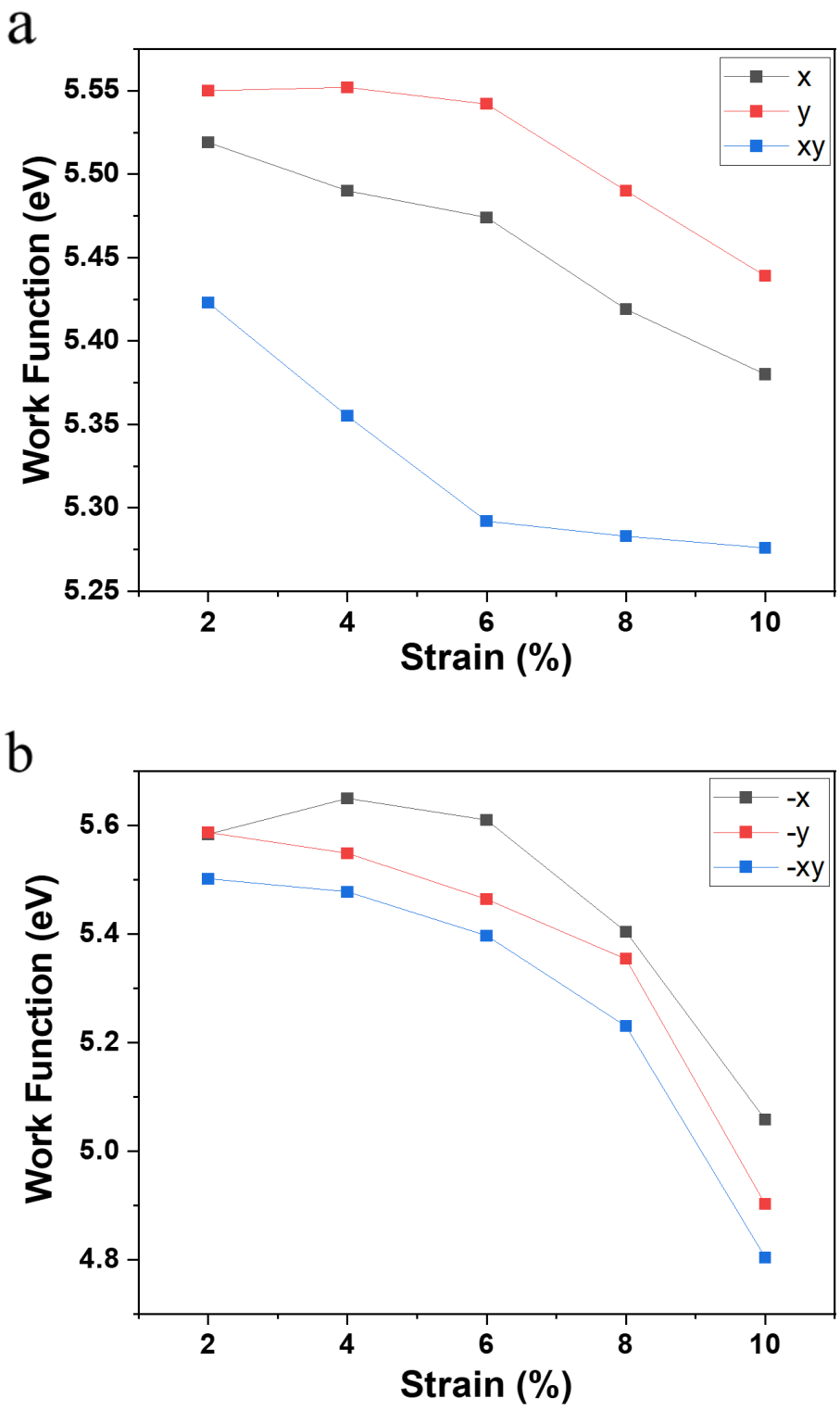

Figure 33. (a) The work function trends of MoS_2 under the uniaxial tensile strain through x, y axis, and biaxial tensile strain through the x– and y–axis. (b) The work

function trends of MoS_2 under the uniaxial tensile strain through the x–, the y–axis, and the biaxial tensile strain through the x– and the y–axis.

The uniaxial tensile strain from x– and the y–axis, and the biaxial tensile strain from the x– and the y–axis, cause the obvious reduction of the WF (**Figure 33**). Under the uniaxial strain from the x–axis, the WF reduces from around 5.525 eV to around 5.4 eV. Under the uniaxial strain from the y–axis, the WF reduces from around 5.55 eV to 5.45 eV. In contrast, the WF reduces from around 5.425 eV to around 5.375 eV. The biaxial tensile strain is more effective in reducing the WF. When the MoS_2 is applied for electrocatalysis, the lower WF implies that the electrons will be easily removed from the MoS_2 and then move toward the target.

Under the uniaxial compressive strain, the WF of MoS_2 demonstrates an overall decreasing trend, where the trend indicates that the compressive strain is more efficient than the tensile strain to reduce the WF of MoS_2. When the 2% to 4% uniaxial compressive strain on the x–axis is induced on the surface of MoS_2, the WF slightly increases. Along with the increase in compressive strain on the x–axis, the WF of MoS_2 is gradually reduced. The 10% uniaxial compressive strain finally reduces the WF of MoS_2 to around 5.1 eV. The uniaxial compressive strain from the y–axis causes a more effective reduction of WF. Under the 2% to 8% uniaxial compressive strain from the y–axis, the reduction of WF demonstrates a relative linear trend. Once the compressive strain on the y–axis increases to 10%, the WF of MoS_2 will be reduced to around 4.9 eV. The biaxial compressive strain is the most effective way to reduce the WF of MoS_2, which ranges from around 5.5 eV to 4.8 eV.

As we mentioned above, the WF is an important parameter to determine the ability to remove electrons from the surface of the material. The lower WF represents that the electrons from the surface of the material are more easily removed. Compared to the tensile and compressive strain, the compressive strain is more effective in reducing the WF of MoS_2. The compressive strain can be used to tune the WF of MoS_2 and then change the ability of electrons to move on the surface of MoS_2. The electrocatalytic activity of MoS_2 will be improved because of the reduction of WF. The efficiency of the MoS_2–based electrocatalysis will be enhanced and then improving the relevant production of the industry.

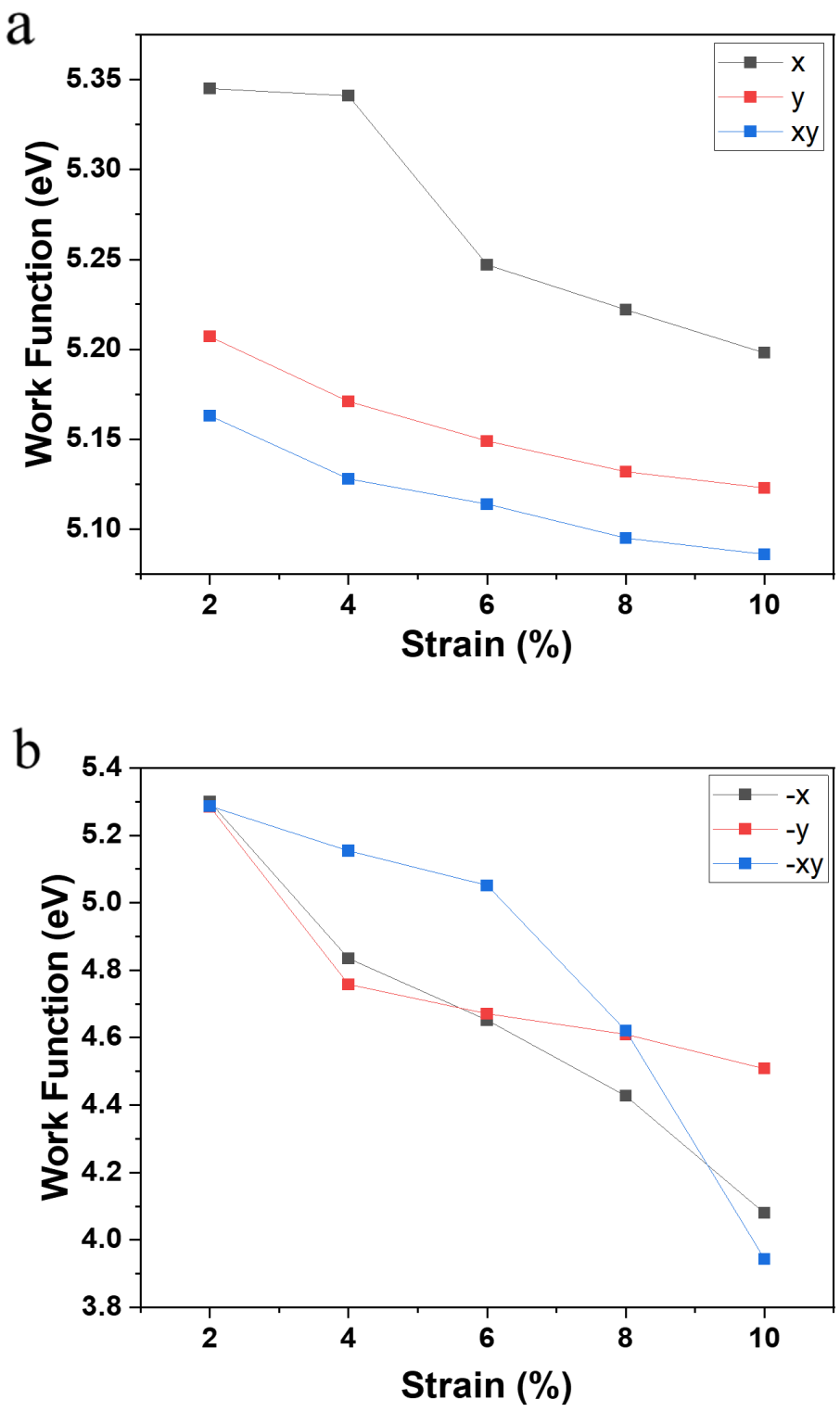

Figure 34. The work function trends of $MoSe_2$ under the uniaxial tensile strain through the x–, y–axis, and the biaxial tensile strain through the x– and the y–axis.

Similar to MoS_2, the WF demonstrates a decreasing trend under the uniaxial and biaxial tensile strain (**Figure 34**). However, the uniaxial tensile strain from the y–axis is more effective than the tensile strain from the x–axis to reduce the WF of $MoSe_2$.

Under the 2% and 4% uniaxial tensile strain from the x–axis, the WF does not show an obvious reduction. Once the tensile strain increases to 6%, the WF shows a significant reduction, which reduces from around 5.35 eV to 5.25 eV. With the 6% to 10% tensile strain, the WF shows a relatively stable and linear reduction, which reduces from 5.25 eV to 5.2 eV.

Different from the uniaxial tensile strain from the x–axis, the uniaxial tensile strain from the y–axis, and the biaxial tensile strain result in the relatively stable reduction of WF. The 2% to 10% uniaxial tensile strain from the y–axis reduces the WF of $MoSe_2$ from around 5.2 eV to around 5.125 eV. Meanwhile, the 2% to 10% biaxial tensile strain causes a similar reduction to the WF, where the WF reduces from around 5.15 eV to around 5.075 eV.

The uniaxial compressive strain also leads to the overall reduction trend of the WF of $MoSe_2$. The 2% uniaxial compressive strain on the x–axis reduces the WF of $MoSe_2$ from around 5.3 eV to around 4.8 eV. And then, the gradually increasing compressive strain causes a relatively linear reduction of WF, which ranges from 4.8 eV to 4.1 eV. The 2% uniaxial compressive strain on the y–axis reduces the WF of $MoSe_2$ from around 5.3 eV to around 4.8 eV. When the larger compressive strain on the y–axis is induced, the slope of the reduction is relatively constant, which ranges from 4.8 eV to

4.5 eV. The biaxial compressive strain is the most effective way to reduce the WF of $MoSe_2$. The 2% to 6% biaxial compressive strain reduces the WF from around 5.3 eV to around 5.0 eV. And then, the 8% biaxial compressive strain reduces the WF of $MoSe_2$ to 4.6 eV. Finally, the 10% biaxial compressive strain further reduces the WF of $MoSe_2$ to around 3.9 eV.

Compared to the WF change of MoS_2 under the uniaxial and biaxial tensile strain, the WF of $MoSe_2$ demonstrates higher sensitivity to the uniaxial and biaxial tensile strain. In addition, the uniaxial tensile strain from the x–axis is more effective in reducing the WF of MoS_2, whereas the uniaxial tensile strain from the y–axis is more effective in reducing the WF of $MoSe_2$. The biaxial tensile strain is the most effective method to reduce the WF of MoS_2 and $MoSe_2$. The compressive test demonstrates the same result as tensile strain. The compressive strain causes the WF reduction to a minimum of 3.9 eV, whereas the tensile strain causes the WF reduction to a minimum of 5.0 eV. The results showed that compressive strain is more effective than tensile strain to reduce the WF. However, the compressive strain causes the relatively uncontrollable reduction of WF, where it is difficult to control the WF of MoS_2 and $MoSe_2$ to the desired range. Although the tensile strain cannot significantly reduce the WF of MoS_2 and $MoSe_2$, it is relatively stable to control the WF and then tune the ability to enhance the performance of these materials. In addition, the results cannot be applied as a reference to estimate the effectiveness of the strain effect for other materials with similar structures.

4.3.3 The band structure of the MoS_2 and $MoSe_2$

The band structure is one of the essential properties of TMC that influences its electronic, optoelectronic, and other properties. The band gap is one of the properties to determine the electronic and electrical properties of TMC. As we mentioned in Chapter 1.2, the TMC commonly possesses a band gap of around 1–3 eV. Metal does not have a band gap, and the electric insulator commonly possesses a band gap above 9 eV.

Besides the magnitude of band gap, the location of valence and conduction bands are important, which controls the optoelectronic property of TMC. When the crystal momentum of the electron and hole contains the same value at the bottom of the conduction band and the top of the valence band, then the band gap is called a direct band gap. In contrast, when the crystal momentum of the electron and the hole are not the same, the band gap is indirect. The direct and indirect band gaps represent the optical and optoelectronic properties of TMC. Generally, the direct band gap emits a photon when electrons transition between the conduction band and the valence band. The indirect band gap commonly does not emit a photon during the electron transmission except the phonon is involved in the transmission. Since the photon possesses almost zero momentum, the energy should be supplemented from another source. According to the energy conservation law, the crystal momentum must be supplemented by the phonon for the photon emission. As a result, the light–emitting material commonly consists of a material with a direct band gap.

The calculated results will provide valuable information as a reference to determine the actual change of band structures and adjust the desired optical and electrical properties.

In some cases, the luminescence property may not be the desired demand, then the modulations of the band structure are necessary to realize the luminescence property of the target.

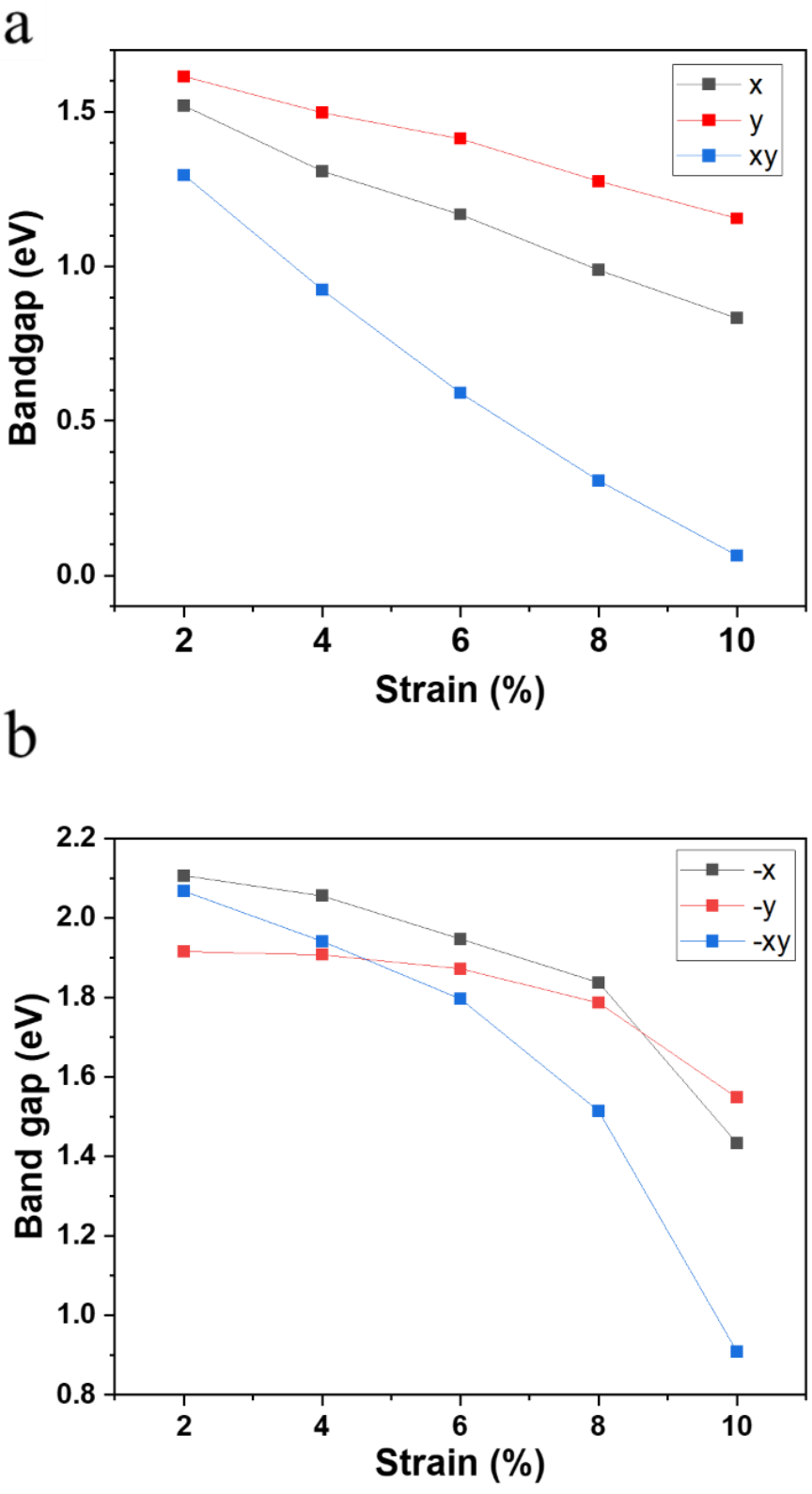

Figure 35. The bandgap trend of MoS_2 with different types of (a) tensile strain, and (b) compressive strain.

The bandgap of MoS_2 changes in different degrees with different types of strain (**Figure 35**). The tensile strain along the x–axis reduces the bandgap of MoS_2 more effectively than the tensile strain along the y–axis. The tensile strain along the y–axis reduces the bandgap of MoS_2 from around 1.6 eV to around 1.2 eV, whereas the tensile strain reduces the bandgap of MoS_2 from around 1.5 eV to around 0.9 eV. Compared to the tensile strain along the x– or y–axis, the biaxial tensile strain significantly reduces the bandgap of MoS_2. Under the biaxial tensile strain, the bandgap of MoS_2 reduces from around 1.3 eV to around 0 eV.

Compared to the tensile strain, the compressive strain is less effective in changing the band gap of the MoS_2. The 2% to 10 % compressive strain of the x– and y–axis reduces the band gap of MoS_2 from around 2.1 eV to around 1.4 eV, and from around 1.9 eV to around 1.5 eV, respectively. The 2% to 10% biaxial compressive strain from the x– and y–axis reduces the band gap of MoS_2 from around 2.1 eV to around 0.9 eV. The result of the compressive strain is similar to the tensile strain, where the biaxial strain is more effective in reducing the band gap of MoS_2.

On one hand, the valence band maximum (VBM) of MoS_2 is primarily composed of 3p orbitals from S atoms, with some 4d characters from Mo atoms. On the other hand, the conduction band minimum (CBM) primarily comes from the 4d orbitals of Mo atoms. The reduction of the band gap originated from the increase in the interatomic distance of MoS_2. The biaxial tensile strain elongates the MoS_2 along the x– and y–axis, stretching the MoS_2 in all in–plane directions. In other words, the Mo–S bond length increases, and the S–Mo–S bond angles are altered slightly.

Under the biaxial tensile strain, the elongation of Mo–S bonds reduces the spatial overlap between 4d and 3p orbitals and then weakens the hybridization. Moreover, due to the reduced orbital overlapping, the CBM and VBM become less stabilized and shift toward each other. The bond elongation weakens the Mo–S interaction, which raises the energy of VBM and reduces the energy of CBM. The shifting of VBM and CBM causes less stabilization and less anti–bonding character of MoS_2. However, the shifting rate of VBM and CBM is not identical, resulting in a progressive narrowing of the band gap.

The value of the bandgap is related to the electrical conductivity of the semiconductor. The reduction of the bandgap implies that the electrical conductivity of MoS_2 is improved. Once the bandgap of MoS_2 reaches around 0 eV, the electrical conductivity of MoS_2 will be similar to that of a metal. The bandgap of MoS_2 and the strain effect show a near–linear relationship, which implies that the bandgap of MoS_2 can be accurately modified through the controllable strain engineering. In some cases, the strained semiconductors replace the metal components and provide better performance than the metal components. The trend from different figures shows the relationship between the band gap and different types of strain. Although the compressive strain is less effective in reducing the band gap of MoS_2, the lower degree of reduction easily controls the band gap according to the condition and the desired command.

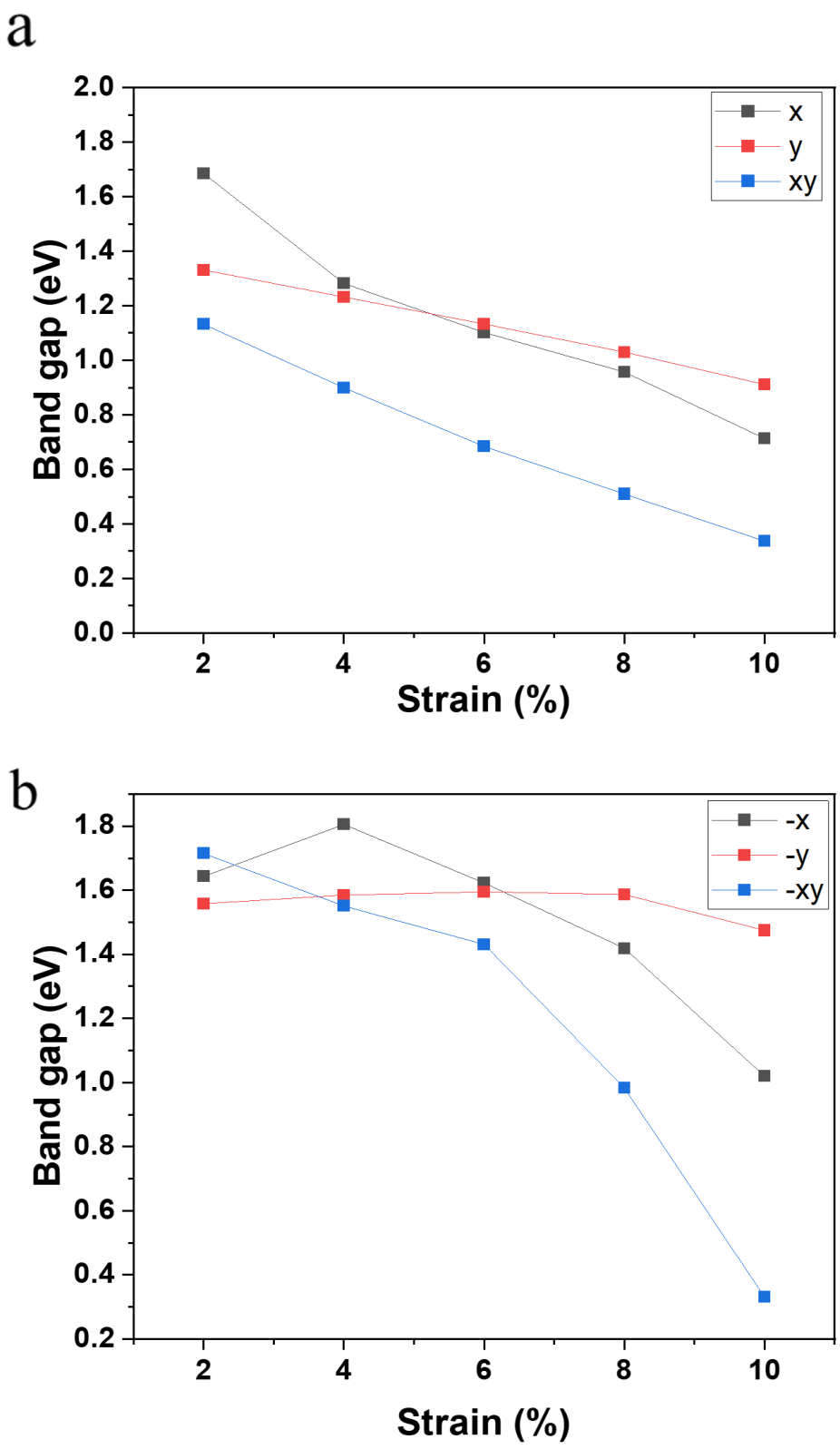

Figure 36. The band gap of $MoSe_2$ with different types of (a) tensile strains, and (b) compressive strains.

The induction of uniaxial and biaxial tensile strain results in the band gap reduction of $MoSe_2$ (**Figure 36**). Along with the gradually increasing tensile strain, the band gap of $MoSe_2$ is continuously reduced. Under the 2% tensile strain on the x–axis, the band gap of $MoSe_2$ is around 1.7 eV. When the tensile strain increases to 4%, the band gap reduces to around 1.3 eV. The 6% tensile strain causes a reduction of the band gap of 0.1 eV. After the tensile strain reaches 8%, the band gap reaches around 1 eV. Once the tensile strain reaches 10%, the band gap reduces to around 0.7 eV.

Compared to the tensile strain on the x–axis, the tensile strain on the y–axis causes the reduction of the band gap with a relative linear slope. The 2% to 10% uniaxial tensile strain on the y–axis causes the reduction from around 1.3 eV to around 1 eV. Meanwhile, the biaxial tensile strain is the most effective method to reduce the band gap of $MoSe_2$. The 2% to 10% biaxial tensile strain can reduce the band gap of $MoSe_2$ from around 1.1 eV to around 0.3 eV.

Although the compressive strain shows the ability to reduce the band gap of $MoSe_2$, the reduction in band gap is not stable and linear. Under the 2% to 4% uniaxial compressive strain on the x–axis, the band gap of $MoSe_2$ shows an increasing trend, where the band gap increases from 1.6 eV to 1.8 eV. Then, the higher compressive strain continuously reduces the band gap of $MoSe_2$, which ranges from 1.8 eV to 1.0 eV. In contrast, the uniaxial compressive strain on the y–axis has almost no effect on improving the band gap of $MoSe_2$. Under the 2% to 8% compressive strain, the band gap of $MoSe_2$ slightly increases, and then the 10% compressive strain reduces the band gap to the level of 2% compressive–strained $MoSe_2$. The biaxial compressive strain completely reduces the band gap of $MoSe_2$ to around 0.3 eV.

The band gap reduction demonstrates a different sensitivity to the uniaxial tensile strain on the x– and y–axis. Although the low tensile strain from the y–axis causes a more effective reduction of the band gap of $MoSe_2$. However, along with the increasing tensile strain, the band gap reduction indicates that $MoSe_2$ is more sensitive to the relatively high tensile strain on the x–axis. For the compressive strain, $MoSe_2$ also shows the sensitivity to the strain on the x–axis than the strain on the y–axis. However, the effectiveness of the compressive strain is not the same as tensile strain. The compressive strain on the y–axis is almost useless to improve the band gap of $MoSe_2$.

The biaxial tensile strain can effectively reduce the band gap of $MoSe_2$, which implies that strain engineering is a possible method to tune the electrical conductivity of $MoSe_2$. In addition, the relatively linear slope of the band gap reduction implies that the band gap can be stably reduced through the biaxial tensile strain. Although the 10% biaxial tensile strain cannot completely reduce the band gap of $MoSe_2$ close to 0 eV, which implies that the electric conductivity of the $MoSe_2$ is close to metal. Meanwhile, the biaxial compressive strain significantly reduces the band gap of $MoSe_2$, which ranges from around 1.7 eV to around 0.3 eV. However, the slope of the reduction indicates that the biaxial compressive strain is not suitable for controlling the band gap of $MoSe_2$ stably. Considering this fact, the tensile strain is more suitable for tuning the electrical properties of MoS_2 and $MoSe_2$ by reducing the band gap.

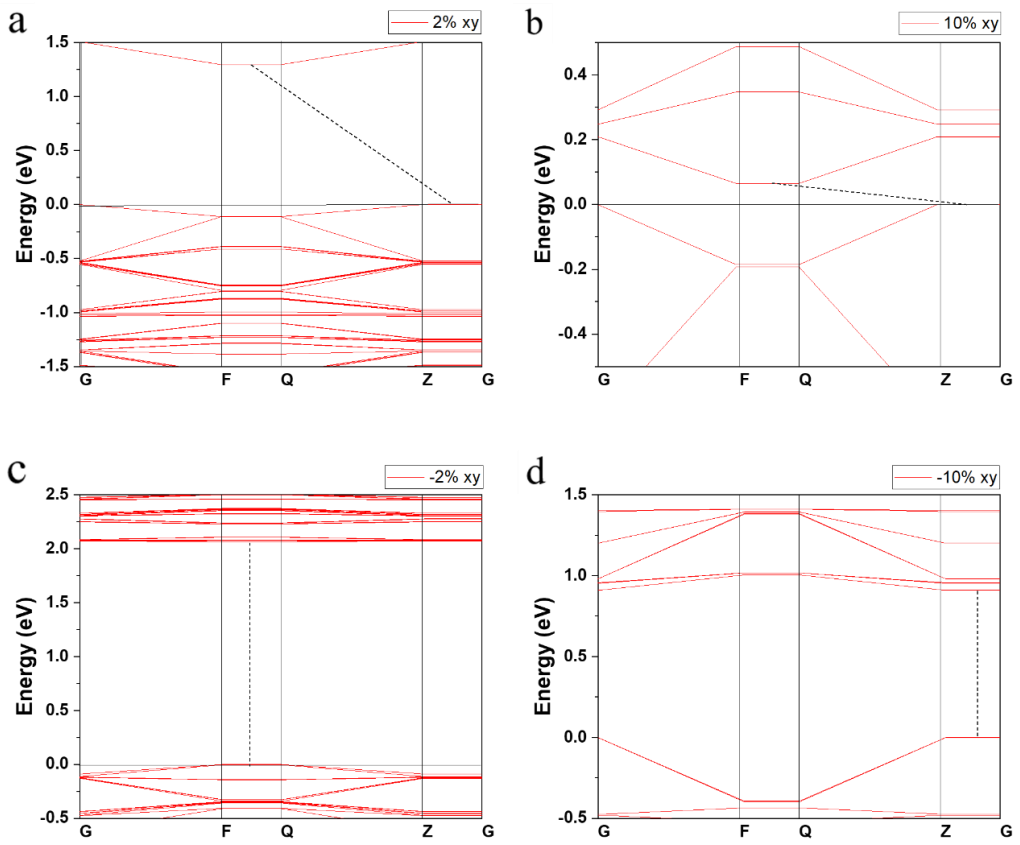

Figure 37. The band structure of MoS_2 of (a) 2%, and (b) 10% of biaxial tensile strain. The band structure of MoS_2 of (c) 2%, and (d) 10% of biaxial compressive strain.

The unstrained MoS_2 possesses a direct band gap, where it undergoes a direct–to–indirect transition under the biaxial tensile and compressive strain (**Figure 37**). The indirect band gap implies that the strained MoS_2 cannot be directly applied as a luminescent material. In this case, the extra energy, i.e., high temperature, is required to provide the phonons for the crystal momentum.

Through the analysis of the single–point energy, work function, band gap, and the DOS, the biaxial strain changes the location of CBM and VBM. Under the 2% and 10% biaxial tensile strain (**Figure 37a-b**), the bottom of the conduction band is located at the position between the F and Q region, where the top of the valence band is located

at the position between the Z and G region. In this case, the top of the valence band and the bottom of the conduction band are not located in the same region. As a result, the biaxial tensile strain causes a direct–to–indirect transition and then causes the indirect band gap in the MoS_2.

Meanwhile, under the 2% biaxial compressive strain (**Figure 37c-d**), the top of the valence band and the bottom of the conduction band are located at the position between the F and Q regions. In addition, under the 10% biaxial compressive strain, the top of valence band and the bottom of the conduction band shift to the region between the Z and G region. Different from the biaxial tensile strain, the biaxial compressive strain shifts the top of valence band and the bottom of conduction band to the same position. The biaxial compressive strain shifts the position of the valence band and conduction band, but the band gap remains as the direct band gap.

The indirect band gap implies that the MoS_2 cannot be directly applied as a photoluminescent material without any handling. MoS_2 with the tensile strain possesses an indirect band gap, which implies that the tensile–strained MoS_2 cannot be applied as a luminescent material. On the other hand, MoS_2 retains the direct band gap under compressive strain, which implies that it can be directly applied as a luminescent material without extra handling.

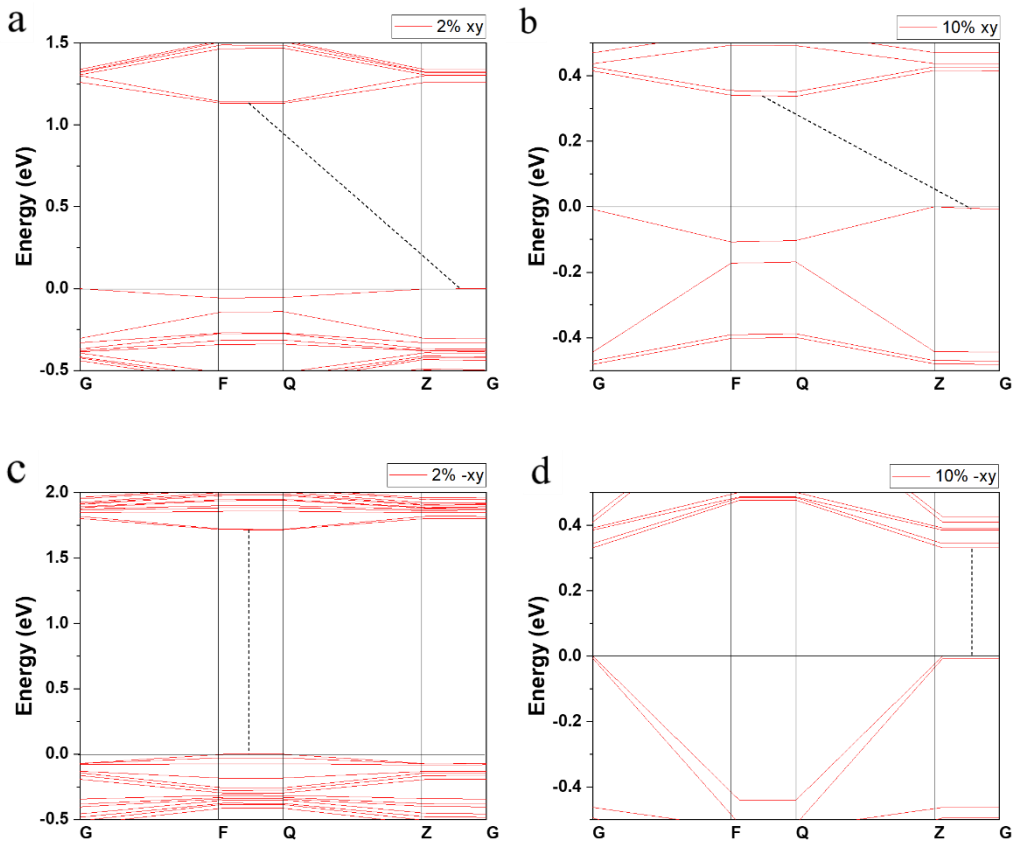

Figure 38. The band structures of $MoSe_2$ with (a) 2%, and (b) 10% of biaxial tensile strain. The band structures of $MoSe_2$ with (c) 2%, and (d) 10% of biaxial compressive strain.

Under the biaxial tensile and compressive strain, the band structure of $MoSe_2$ also demonstrates the shifting of the bottom of conduction band and the top of valence band. With the 2% and 10% biaxial tensile strain (**Figure 38a-b**), the top of the valence band locates between the F and G region, where the bottom of the valence band is located between the Z and G region. Same with MoS_2, the biaxial tensile strain also causes the direct–to–indirect transition and induces the indirect band gap of $MoSe_2$.

On the other hand, under the biaxial compressive strain (**Figure 38c-d**), the location of

the top of the valence band and the bottom of the conduction band are shifted to another region. With the 2% biaxial compressive strain, the top of valence band and the bottom of conduction band locate at the region between F and G. When the 10% biaxial compressive strain is induced to $MoSe_2$, the top of valence band and the bottom of conduction band shift to the region between Z and G. Although the location of the top of valence band and the bottom of conduction band is shifted under compressive strain, the location of two bands is the same, where it remains the direct band gap.

The band structure of MoS_2 and $MoSe_2$ shows the same change under the biaxial tensile and compressive strain. With the biaxial tensile strain, the band structure of MoS_2 and $MoSe_2$ undergoes a direct–to–indirect transition and then forms an indirect band gap. In contrast, the biaxial compressive strain immediately shifts the location of the top of the valence band and the bottom of the conduction band. After the shifting resulting from the compressive strain, the top of the valence band and the bottom of the conduction band are located at the same region, which forms the direct band gap.

With the tensile strain, MoS_2 and $MoSe_2$ possess the indirect band gap, which implies that the tensile–strained MoS_2 and $MoSe_2$ cannot be directly applied as luminescent material without any handling. In contrast, the compressive strain results in the direct band gap, which can be directly applied for luminescence without any modifications.

On one hand, the compressive strain causes the relatively uncontrollable change in the WF and the band gap, which causes the difficulty for accurately tuning the electronic property of MoS_2 and $MoSe_2$. On the other hand, the compressive strain shifts the location of the band structure and then maintains the direct band gap of MoS_2 and

$MoSe_2$, which maintains the optoelectronic properties of MoS_2 and $MoSe_2$.

4.3.4 The DOS change of MoS_2 and $MoSe_2$

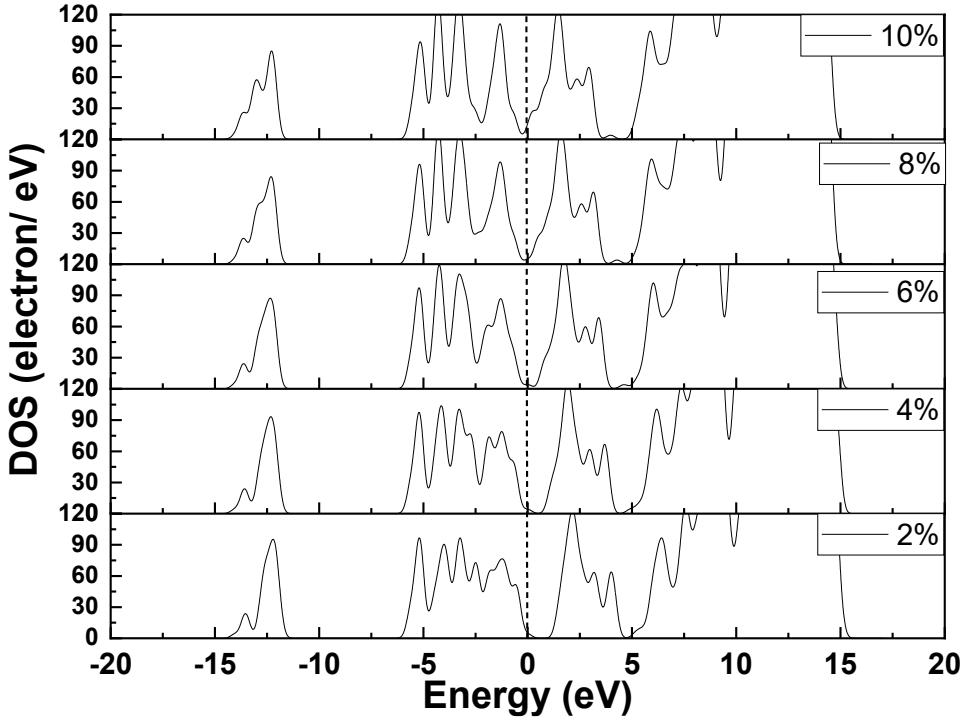

Figure 39. The DOS of MoS_2 with different biaxial tensile strains on the x– and y–axis.

The result of the band gap shows that the biaxial tensile strain is the most effective way. As a result, the DOS and PDOS analysis of MoS_2 and $MoSe_2$ focuses on the biaxial tensile strain (**Figure 39**).

The changes of the PDOS of the MoS_2 mainly focus on the range of − 6 eV to 0 eV, and the range of –14 to –12 eV. The peak is located around –2 eV, showing the changes throughout the 2% to 10 % strain. From 2% to 10 % tensile strain, the peak intensity gradually increases and becomes more concentrated.

The peaks correspond to the different orbitals, including the s, p, d, and f orbitals of the

Mo and S atoms. The peak is mainly affected by the s and p orbitals from the S atom, and the d orbitals from the Mo atom. The changes of full DOS are mainly focused on the region between the energies of –15 to 10 eV, –5 to 0 eV, and 0 to 5 eV. The further investigation of the DOS of MoS_2 will be continuous through the analysis of the separated s, p, and d orbitals.

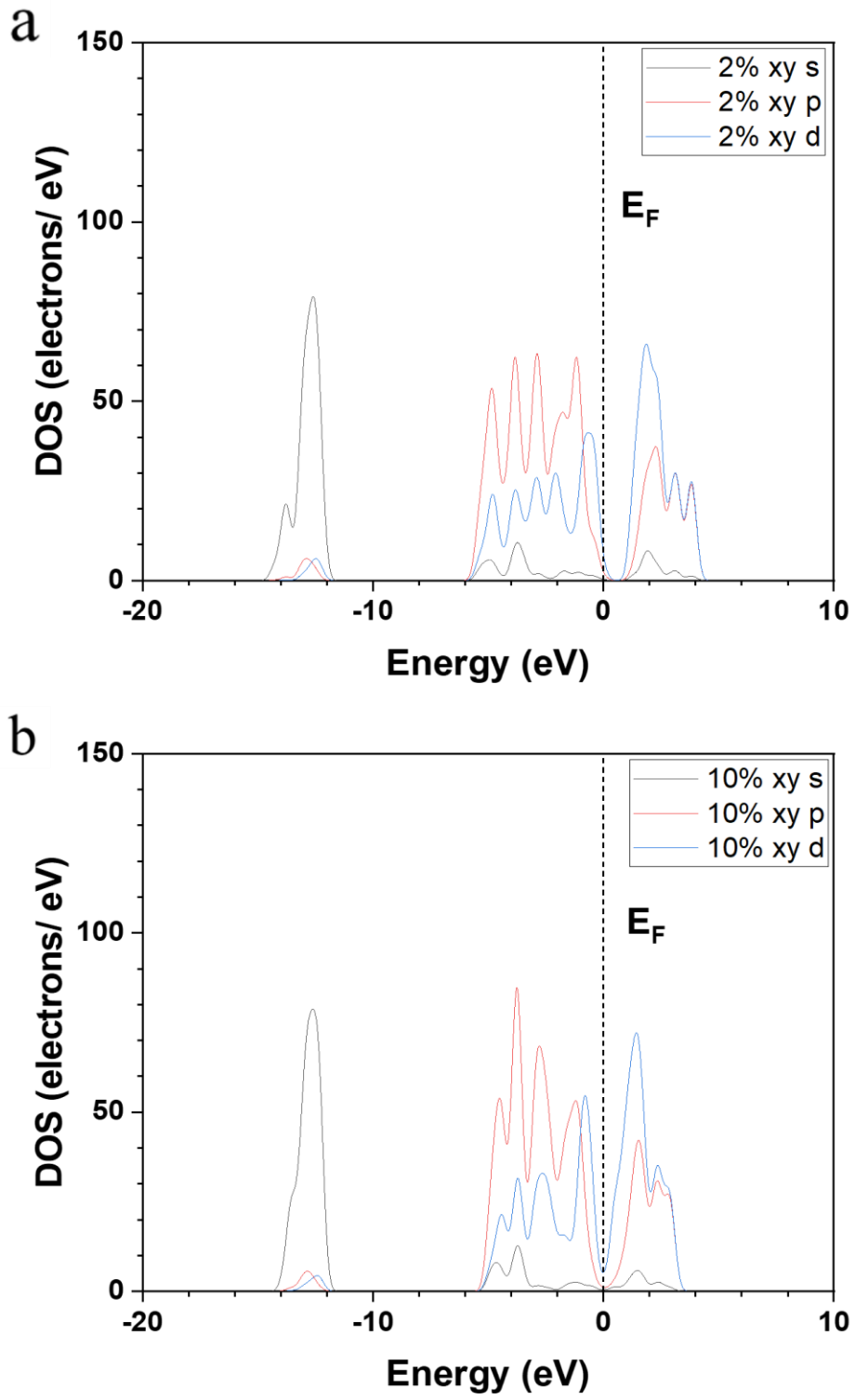

Figure 40. The PDOS of s, p, and d orbitals of MoS_2 with 2% biaxial tensile strain.

Through the analysis of the separated s, p, and d orbitals, the role of these orbitals is

investigated (**Figure 40**). The change of the peak located between –15 and –10 eV is mainly affected by the s orbital. For the peak located between –5 and 0 eV, the p orbital mainly influences the peak until the Fermi level. Near the Fermi level, the d orbital from the Mo atom contributes to the change of the DOS and the band gap. For the location higher than the Fermi level, the change is mainly contributed to the d orbital and the p orbital. The s orbital is almost ineffective for the change of the location higher than the Fermi level.

The 3p orbital from the S atom contributes to the VBM, and the 4d orbital from the Mo atom contributes to the CBM. The shifting of VBM and CBM is proportional to strain, which corresponds to the hybridization reduction. As the strain increases, the band gap between the 3p and 4p orbitals gradually becomes narrower. Moreover, the shifting of VBM and CBM is not equal, which proves the difference in the shifting rate. Finally, the CBM and VBM almost converge, resulting in an almost zero band gap (semimetallic state). When the critical strain is achieved, MoS_2 also demonstrates a zero–band gap.

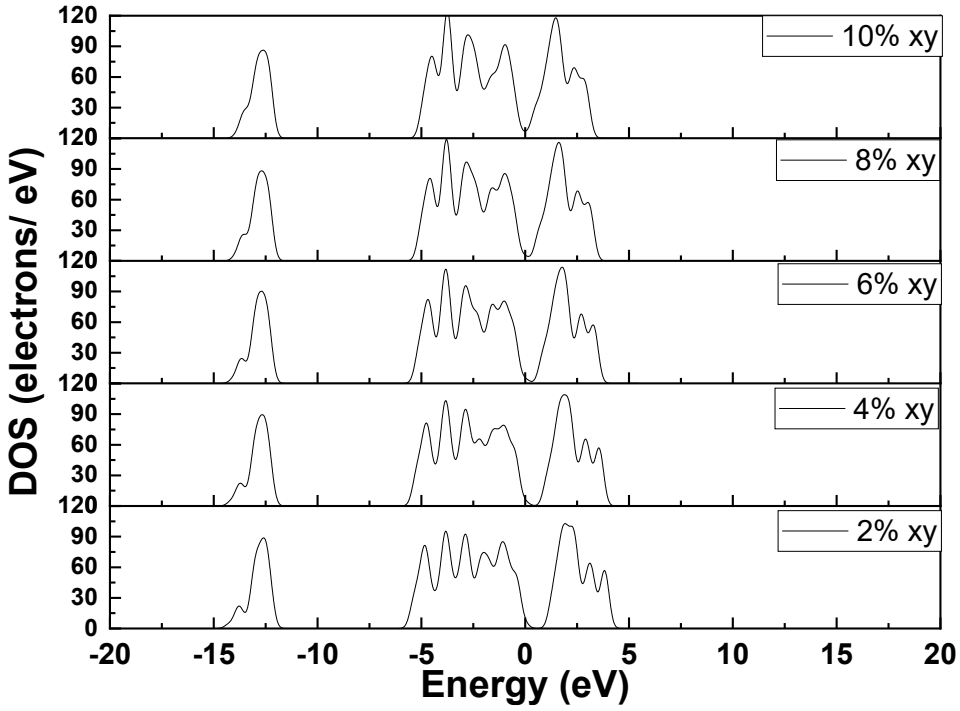

Figure 41. DOS of $MoSe_2$ with different biaxial tensile strains on the x– and y–axis.

Different from the MoS_2, the contribution of the DOS of $MoSe_2$ is concentrated on the location between –15 to –10 eV, and –5 to 5 eV. The peak changes of the DOS of $MoSe_2$ mainly focus on the locations around –12 eV, 0 eV, and 5 eV. Along with the increase of the tensile strain, the peaks of these locations become more intense and concentrated gradually. The changes in the peak distribution and intensity are contributing to different orbitals.

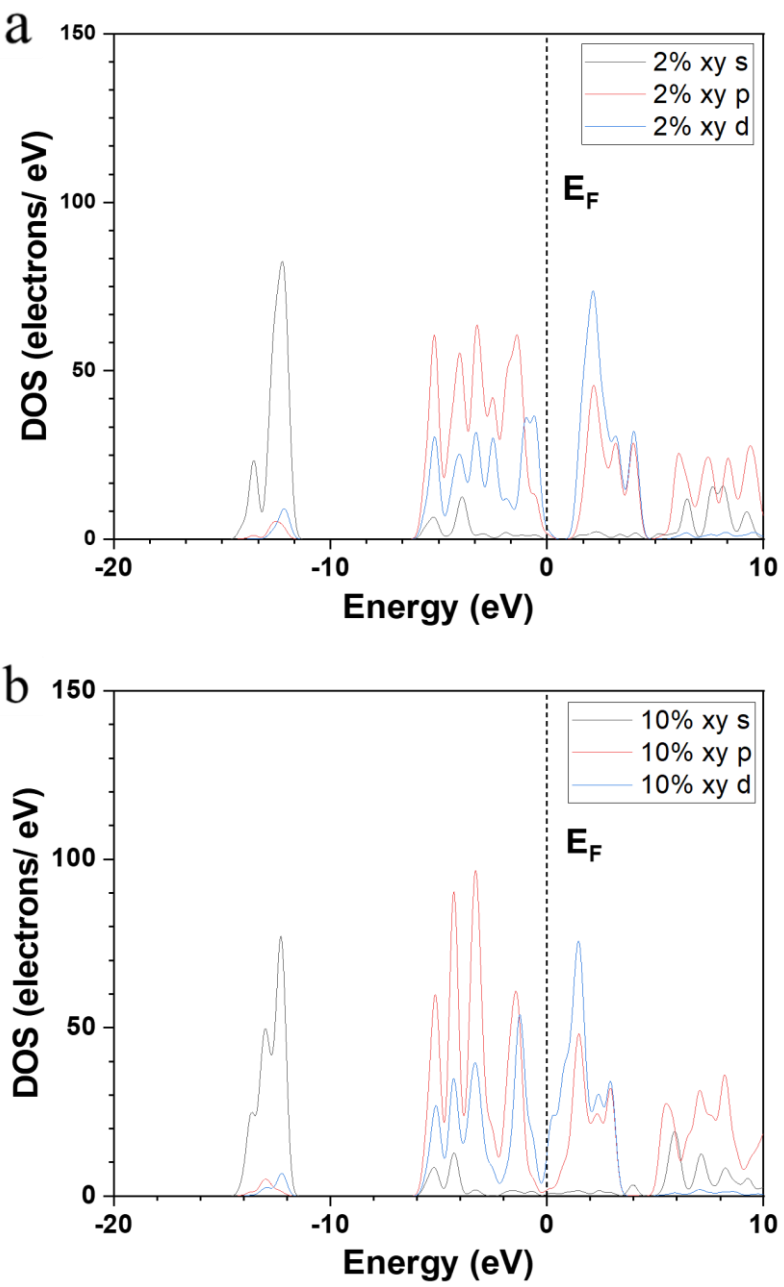

Figure 42. The PDOS of s, p, and d orbitals of $MoSe_2$ with (a) 2% tensile strain, and (b) 10% tensile strain.

Similar to the DOS of MoS_2, the s, p, and d orbital of $MoSe_2$ are corresponded to the peak changes located at different coordination. For the peak located at around –14 to –12 eV, the peak change is mainly contributed to the change of s orbital, where the p and

d orbitals are almost unchanged under the tensile strain. The enhancement of the tensile strain results in a more intense and concentrated peak.

For the location between the –6 to 0 eV, the p orbital is mainly contributed to the change of the peak intensity and contribution. The increasing of the tensile strain causes the more intense p orbital and then enhance the peak intensity of this location. The d orbital contributes to the change near the Fermi level and then reduces the value of the band gap.

Chapter 5

Conclusion and Outline

5. Conclusion and Outline

In conclusion, the strain and ripple effect on the TM and the TMC are investigated in the thesis. For the TM, Pt and Pd are chosen as the target, whereas MoS_2 and $MoSe_2$ are chosen as the target for the TMC. These targets are the common samples and candidates that are applied to different fields, including the new–typed energy, energy storage, energy device, electrocatalysis, and other energy–related applications.

In this thesis, the investigation is conducted by the DFT calculator, where the software Atomsk and MS are chosen. For the geometric modification, Atomsk is chosen to change the arrangement of each target with a simple command. After the modification, the modified models are calculated by the MS. For the calculations of geometry optimization, the CASTEP is chosen to determine the property change of strain and ripple effect. The calculated data includes the single–point energy, the work function (WF), density–of–state (DOS), partial density–of–state (PDOS), d–band center, and the band gap. Through the analysis of these properties, the ripple and strain effect on the TM and TMC can be qualified and then investigated, which can assist in further understanding the effect and mechanism of strain and ripple on the TM and TMC.

Under the ripple effect, the single–point energy, WF, and the d–band center of Pt and Pd are significantly modified. Along with the increase of ripple, the single–point energy of each atom increases due to the instability of the rippled structure. The WF is also effectively reduced by and ripple effect, where the ripple effect causes an overall around 0.5 eV WF reduction of Pt and Pd. Through the analysis of the PDOS, the peaks intensity at the center of the convex side and the edge of the concave side, are enhanced

and concentrated near the Fermi level. On the other hand, the peak intensity and distribution at the edge of the convex side and the center of the concave side, show the opposite results compared to the center of the convex side and the edge of the concave side. The ripple induction causes the unpredictable change in the bond distance, which causes the uneven strain distribution on the surface of Pt and Pd. Due to the uneven strain distribution, the d–band center of the surface of Pt and Pd demonstrates an unpredictable results.

Compared to the ripple effect, the strain effect lead to a relatively stable modification to the properties of Pt and Pd. The strain effect causes the same trend as the ripple effect, but the increasing trend is less than the ripple effect. For the WF, the compressive strain, including the uniaxial strain through the x– and y–axis, and the biaxial strain through the x– and y–axis, is more effective than the tensile strain to reduce the WF. The results from PDOS indicates that the tensile strain causes the electrons to move towards the Fermi level, and the peak intensity increases with the larger strain effect. In contrast, the compressive strain led to peak intensity reduction, and more electrons moved away from the Fermi level. Because of the change of d orbital in PDOS, the d–band center of Pt and Pd demonstrates an overall increasing and reduction trend under tensile strain and compressive strain, respectively.

Compare the ripple and strain effect; the ripple effect is more effective in tuning the properties of Pt and Pd. However, the unpredictable and uncontrollable deformation causes the bond length and angle without a pattern. Therefore, the interactions of reactants with the surface of Pt and Pd cause different reaction rates, resulting in the uncertainty of different reactions. In contrast, the strain effect is less effective than the

ripple effect to tune the properties of Pt and Pd. However, the uniaxial and biaxial strain evenly and uniformly induce the strain to the surface of Pt and Pd. In other words, the interaction of reactant with all positions on the surface of Pt and Pd will be the same, which is more stable than the ripple effect.

The single–point energy of TMC under the strain and ripple effect indicates that the TMC is less against to the deformation from strain and ripple. The relatively high elasticity of TMC is the potential reason for the difference. In most cases, the single–point energy increase of TMC from the ripple induction is higher than the increase caused by the strain effect. Under the ripple effect, the WF of MoS_2 and $MoSe_2$ reduces by around 1.1 and 0.5 eV, respectively. For the band gap, MoS_2 and $MoSe_2$ show different sensitivity to the ripple, where the 6 Å and 2 Å height of the ripple completely reduce the band gap to 0 eV. In addition, the band structure of MoS_2 and $MoSe_2$ under a direct–to–indirect transition and then become an indirect band gap. The peak intensity of DOS totally reduces, and the distribution becomes more even along with the increase of the ripple.

Under the strain effect, the WF of MoS_2 and $MoSe_2$ is also reduced. In general, tensile strain is less effective than compressive strain to reduce the WF of MoS_2 and $MoSe_2$. In contrast, the tensile strain causes the more linear reduction in WF than the compressive strain, which implies that tensile strain enables to stably tune the WF. In addition, the biaxial strain is effective than uniaxial tensile strain to reduce WF. Moreover, tensile strain is more effective and linearly to reduce the band gap, whereas biaxial tensile strain is the most effective way to tune the band gap of TMC. Under the tensile strain, the band structure of MoS_2 and $MoSe_2$ has an indirect band gap, whereas

compressive strain causes a direct band gap. Under the tensile strain, the peak of DOS is more concentrated, which influences the binding of reactant with MoS_2 and $MoSe_2$ during the process of catalysis.

Ripple demonstrates the effectiveness of WF and band gap reduction, but the reduction slopes are not linear, which represents the uncontrollable. The strain induction shows the flexibility to tune the properties of MoS_2 and $MoSe_2$, in particular for the biaxial tensile strain. In addition, tensile and compressive strain are chosen to tune the types of band gap.

Strain effect is more common than ripple effect to modify the properties of LD materials, including TM, TMC, and other semiconductors. The relatively linear slope represents the stability and controllability of this method. In addition, the flexibility of the strain effect provides multiple ways to solve different problems. For now, the strain effect is the best method to tune the properties of LD TM and TMC. Although the ripple induction is uncontrollable and leads to difficulty in tuning the properties of TM and TMC, the results reveal the potential of the ripple effect to change the properties of the LD material. The following studies further supply insights into understanding the ripple effect and then improving the applications. In the future, the relevant study, including the actual influence of strain and ripple effect on different catalytic reactions, and the mechanical properties, will be performed to develop a better version of strained and rippled LD materials. The results in this thesis and the following study should be useful for future work. It is believed that the relevant technique can be used as the common way to change and modify the properties of LD materials.

Publications

1. **Chan, C. H.**, Wong, H. H., Liang, S., Sun, M., Wu, T., Lu, Q., ... & Huang, B. (2024). Electrolyte Developments for All-Solid-State Lithium Batteries: Classifications, Recent Advances and Synthesis Methods. *Batteries & Supercaps*, *7*(12), e202400432.
2. **Chan, C. H.**, Sun, M., & Huang, B. (2022). Application of machine learning for advanced material prediction and design. *EcoMat*, *4*(4), e12194.
3. Yu, H., Sun, M., Wu, X., **Chan, C. H.**, Huang, B., & Wang, Z. L. (2024). Atomscopic of ripple origins for two–dimensional monolayer transition metal dichalcogenides. *Nano Research*, *17*(3), 2136–2144.
4. Sun, M., Wong, H. H., Wu, T., Lu, Q., Lu, L., **Chan, C.** H., ... & Huang, B. (2023). Double-Dependence Correlations in Graphdiyne-Supported Atomic Catalysts to Promote CO_2RR toward the Generation of C_2 Products. *Advanced Energy Materials*, *13*(7), 2203858.
5. Wu, T., Sun, M., Wong, H. H., **Chan, C. H.**, Lu, L., Lu, Q., ... & Huang, B. (2023). Recent advances and strategies of electrocatalysts for large current density industrial hydrogen evolution reaction. *Inorganic Chemistry Frontiers*, *10*(16), 4632–4649.
6. Lu, L., Sun, M., Wu, T., Lu, Q., Chen, B., **Chan, C. H.**, ... & Huang, B. (2024). Screening of red phosphorus supported transition metal single–atom catalysts for efficient photocatalytic water splitting H_2 generation. *Inorganic Chemistry Frontiers*, *11*(20), 6853–6861.

Reference

1. Feng, S., et al., *Doping two-dimensional materials: ultra-sensitive sensors, band gap tuning and ferromagnetic monolayers.* Nanoscale Horizons, 2017. **2**(2): p. 72-80.
2. Liu, Y., et al., *Synthesis of low-symmetry 2D Ge (1− x) Sn x Se 2 alloy flakes with anisotropic optical response and birefringence.* Nanoscale, 2019. **11**(48): p. 23116-23125.
3. Yang, S., et al., *Defect-modulated transistors and gas-enhanced photodetectors on ReS2 nanosheets.* Advanced Materials Interfaces, 2016. **3**(6): p. 1500707.
4. Novoselov, K., et al., *2D materials and van der Waals heterostructures.* Science, 2016. **353**(6298): p. aac9439.
5. Naumis, G.G., et al., *Electronic and optical properties of strained graphene and other strained 2D materials: a review.* Reports on Progress in Physics, 2017. **80**(9): p. 096501.
6. Dresselhaus, M., et al., *Low-dimensional thermoelectric materials.* Physics of the Solid State, 1999. **41**(5): p. 679-682.
7. Takagahara, T. and K. Takeda, *Theory of the quantum confinement effect on excitons in quantum dots of indirect-gap materials.* Physical Review B, 1992. **46**(23): p. 15578.
8. Bagheri, M. and H.P. Komsa, *Screening 0D materials for 2D nanoelectronics applications.* Advanced Electronic Materials, 2023. **9**(1): p. 2200393.
9. Noy, A., A.B. Artyukhin, and N. Misra, *Bionanoelectronics with 1D materials.* Materials today, 2009. **12**(9): p. 22-31.
10. He, B., et al., *Multidimensional (0D-3D) functional nanocarbon: Promising material to strengthen the photocatalytic activity of graphitic carbon nitride.* Green Energy & Environment, 2021. **6**(6): p. 823-845.
11. Shaw, Z., et al., *Antipathogenic properties and applications of low-dimensional materials.* Nature communications, 2021. **12**(1): p. 3897.
12. Roy, D., et al., *0D, 1D, 2D & 3D Nano materials: synthesis and applications*, in *Novel Defence Functional and Engineering Materials (NDFEM) Volume 1: Functional Materials for Defence Applications*. 2024, Springer. p. 73-91.
13. Liu, G., et al., *0D to 2D carbon-based materials in flexible strain sensors: recent advances and perspectives.* 2D Materials, 2023. **10**(2): p. 022002.
14. Li, S.-L., et al., *Charge transport and mobility engineering in two-dimensional transition metal chalcogenide semiconductors.* Chemical Society Reviews, 2016. **45**(1): p. 118-151.
15. Li, Y., et al., *MoS2 nanoparticles grown on graphene: an advanced catalyst for the hydrogen evolution reaction.* Journal of the American Chemical Society, 2011. **133**(19): p. 7296-7299.
16. Benediktsdóttir, B.E., Ó. Baldursson, and M. Másson, *Challenges in evaluation of chitosan and trimethylated chitosan (TMC) as mucosal permeation enhancers: From synthesis to in vitro application.* Journal of Controlled Release, 2014. **173**: p. 18-31.
17. Miró, P., M. Ghorbani-Asl, and T. Heine, *Two dimensional materials beyond MoS2: noble-transition-metal dichalcogenides.* Angewandte Chemie International Edition, 2014. **53**(11): p. 3015-3018.
18. Han, G.H., et al., *van der Waals metallic transition metal dichalcogenides.*

Chemical reviews, 2018. **118**(13): p. 6297-6336.
19. Das, C., N. Sinha, and P. Roy, *Transition metal non-oxides as electrocatalysts: advantages and challenges.* Small, 2022. **18**(28): p. 2202033.
20. Warra, A., *Transition metal complexes and their application in drugs and cosmetics-a Review.* J. Chem. Pharm. Res, 2011. **3**(4): p. 951-958.
21. Jana, A., E. Scheer, and S. Polarz, *Synthesis of graphene–transition metal oxide hybrid nanoparticles and their application in various fields.* Beilstein journal of nanotechnology, 2017. **8**(1): p. 688-714.
22. Yang, J. and H.S. Shin, *Recent advances in layered transition metal dichalcogenides for hydrogen evolution reaction.* Journal of Materials Chemistry A, 2014. **2**(17): p. 5979-5985.
23. Goswami, C., K.K. Hazarika, and P. Bharali, *Transition metal oxide nanocatalysts for oxygen reduction reaction.* Materials Science for Energy Technologies, 2018. **1**(2): p. 117-128.
24. Royer, S. and D. Duprez, *Catalytic oxidation of carbon monoxide over transition metal oxides.* ChemCatChem, 2011. **3**(1): p. 24-65.
25. You, B. and Y. Sun, *Innovative strategies for electrocatalytic water splitting.* Accounts of chemical research, 2018. **51**(7): p. 1571-1580.
26. Dai, Z., L. Liu, and Z. Zhang, *Strain engineering of 2D materials: issues and opportunities at the interface.* Advanced Materials, 2019. **31**(45): p. 1805417.
27. Ahn, G.H., et al., *Strain-engineered growth of two-dimensional materials.* Nature communications, 2017. **8**(1): p. 608.
28. Yang, S., et al., *Tuning the optical, magnetic, and electrical properties of ReSe2 by nanoscale strain engineering.* Nano letters, 2015. **15**(3): p. 1660-1666.
29. Aslan, B., et al., *Probing the optical properties and strain-tuning of ultrathin Mo1–x W x Te2.* Nano letters, 2018. **18**(4): p. 2485-2491.
30. Li, M.-Y., et al., *Epitaxial growth of a monolayer WSe2-MoS2 lateral pn junction with an atomically sharp interface.* Science, 2015. **349**(6247): p. 524-528.
31. Wang, M.C., et al., *Heterogeneous, three-dimensional texturing of graphene.* Nano letters, 2015. **15**(3): p. 1829-1835.
32. Qi, J., et al., *Piezoelectric effect in chemical vapour deposition-grown atomic-monolayer triangular molybdenum disulfide piezotronics.* Nature communications, 2015. **6**(1): p. 1-8.
33. Mohiuddin, T., et al., *Uniaxial strain in graphene by Raman spectroscopy: G peak splitting, Grüneisen parameters, and sample orientation.* Physical Review B, 2009. **79**(20): p. 205433.
34. Huang, J., et al., *Increasing the active sites and intrinsic activity of transition metal chalcogenide electrocatalysts for enhanced water splitting.* Journal of Materials Chemistry A, 2020. **8**(48): p. 25465-25498.
35. Kumar, S., et al., *A review on 2D transition metal di-chalcogenides and metal oxide nanostructures based NO2 gas sensors.* Materials Science in Semiconductor Processing, 2020. **107**: p. 104865.
36. Johari, P. and V.B. Shenoy, *Tuning the electronic properties of semiconducting transition metal dichalcogenides by applying mechanical strains.* ACS nano, 2012. **6**(6): p. 5449-5456.
37. Chittari, B.L., et al., *Carrier-and strain-tunable intrinsic magnetism in two-dimensional MAX 3 transition metal chalcogenides.* Physical Review B, 2020. **101**(8): p. 085415.
38. Lu, Y. and S.B. Sinnott, *Density functional theory study of epitaxially strained*

monolayer transition metal chalcogenides for piezoelectricity generation. ACS Applied Nano Materials, 2019. **3**(1): p. 384-390.
39. Friedel, J. and C. Sayers, *On the role of dd electron correlations in the cohesion and ferromagnetism of transition metals.* Journal de Physique, 1977. **38**(6): p. 697-705.
40. Zhong, Z., et al., *Surface Strain Effect on Electrocatalytic Hydrogen Evolution Reaction of Pt-Based Intermetallics.* ACS Catalysis, 2024. **14**(5): p. 2917-2923.
41. Huang, H., et al., *Understanding of strain effects in the electrochemical reduction of CO2: using Pd nanostructures as an ideal platform.* Angewandte Chemie, 2017. **129**(13): p. 3648-3652.
42. Butler, K.T., et al., *Machine learning for molecular and materials science.* Nature, 2018. **559**(7715): p. 547-555.
43. Bullnheimer, B., R.F. Hartl, and C. Strauss, *A new rank based version of the Ant System. A computational study.* 1997.
44. Al Hasan, N. *Prediction of mechanical properties of EPON 862 (DGEBF) cross-linked with curing agent (TETA) and SiO2 nanoparticle based on materials studio*. in *IOP Conference Series: Materials Science and Engineering*. 2018. IOP Publishing.
45. Hirel, P., *Atomsk: A tool for manipulating and converting atomic data files.* Computer Physics Communications, 2015. **197**: p. 212-219.
46. Meunier, M. *Introduction to materials studio*. in *EPJ Web of Conferences*. 2012. EDP Sciences.
47. Sharma, S., P. Kumar, and R. Chandra, *Applications of BIOVIA materials studio, LAMMPS, and GROMACS in various fields of science and engineering.* Molecular dynamics simulation of nanocomposites using BIOVIA materials studio, Lammps and Gromacs, 2019: p. 329-341.
48. Grillo, M., et al., *Computational materials science with materials studio: Applications in catalysis*, in *Computational Materials Science: From Basic Principles to Material Properties*. 2004, Springer. p. 207-221.
49. Shankar, U., et al., *Introduction to materials studio software for the atomistic-scale simulations*, in *Forcefields for atomistic-scale simulations: materials and applications*. 2022, Springer. p. 299-313.
50. Sharma, S., *Molecular dynamics simulation of nanocomposites using BIOVIA materials studio, lammps and gromacs*. 2019: Elsevier.
51. Clark, S.J., et al., *First principles methods using CASTEP.* Zeitschrift für kristallographie-crystalline materials, 2005. **220**(5-6): p. 567-570.
52. Hasnip, P.J., et al., *Density functional theory in the solid state.* Philosophical Transactions of the Royal Society A: Mathematical, Physical and Engineering Sciences, 2014. **372**(2011): p. 20130270.
53. Lejaeghere, K., et al., *Reproducibility in density functional theory calculations of solids.* Science, 2016. **351**(6280): p. aad3000.
54. Sholl, D.S. and J.A. Steckel, *Density functional theory: a practical introduction*. 2022: John Wiley & Sons.
55. Mattsson, A.E., et al., *Designing meaningful density functional theory calculations in materials science—a primer.* Modelling and Simulation in Materials Science and Engineering, 2004. **13**(1): p. R1.
56. Bartolotti, L.J. and K. Flurchick, *An introduction to density functional theory.* Reviews in computational chemistry, 1996: p. 187-216.
57. Kohn, W., A.D. Becke, and R.G. Parr, *Density functional theory of electronic structure.* The journal of physical chemistry, 1996. **100**(31): p. 12974-12980.

58. Berezin, F.A. and M. Shubin, *The Schrödinger Equation*. Vol. 66. 2012: Springer Science & Business Media.
59. Feit, M., J. Fleck Jr, and A. Steiger, *Solution of the Schrödinger equation by a spectral method.* Journal of Computational Physics, 1982. **47**(3): p. 412-433.
60. Leforestier, C., et al., *A comparison of different propagation schemes for the time dependent Schrödinger equation.* Journal of Computational Physics, 1991. **94**(1): p. 59-80.
61. Dong, J. and M. Xu, *Space–time fractional Schrödinger equation with time-independent potentials.* Journal of Mathematical Analysis and Applications, 2008. **344**(2): p. 1005-1017.
62. Parwani, R.R., *Why is Schrödinger's equation linear?* Brazilian Journal of Physics, 2005. **35**: p. 494-496.
63. Schleich, W.P., et al., *Schrödinger equation revisited.* Proceedings of the National Academy of Sciences, 2013. **110**(14): p. 5374-5379.
64. Adhikari, S.K. and L. Salasnich, *Nonlinear Schrödinger equation for a superfluid Bose gas from weak coupling to unitarity: Study of vortices.* Physical Review A—Atomic, Molecular, and Optical Physics, 2008. **77**(3): p. 033618.
65. Cetto, A., L.d. la Peña, and A. Valdés-Hernández, *Specificity of the Schrödinger equation.* Quantum Studies: Mathematics and Foundations, 2015. **2**(3): p. 275-287.
66. Górka, P., H. Prado, and J. Trujillo, *The time fractional Schrödinger equation on Hilbert space.* Integral Equations and Operator Theory, 2017. **87**: p. 1-14.
67. Bourgain, J., *Quasi-periodic solutions of Hamiltonian perturbations of 2D linear Schrödinger equations.* Annals of Mathematics, 1998: p. 363-439.
68. Hodge, W., S. Migirditch, and W.C. Kerr, *Electron spin and probability current density in quantum mechanics.* American Journal of Physics, 2014. **82**(7): p. 681-690.
69. Slater, J.C., *A simplification of the Hartree-Fock method.* Physical review, 1951. **81**(3): p. 385.
70. Valatin, J., *Generalized hartree-fock method.* Physical Review, 1961. **122**(4): p. 1012.
71. Bartlett, R.J. and J.F. Stanton, *Applications of Post-Hartree—Fock Methods: A Tutorial.* Reviews in computational chemistry, 1994: p. 65-169.
72. Cremer, D., *Møller–Plesset perturbation theory: from small molecule methods to methods for thousands of atoms.* Wiley Interdisciplinary Reviews: Computational Molecular Science, 2011. **1**(4): p. 509-530.
73. Olsen, J., *The CASSCF method: A perspective and commentary.* International Journal of Quantum Chemistry, 2011. **111**(13): p. 3267-3272.
74. Stoll, H., *On the coupling of multi-configuration self-consistent-field and density-functional information.* Chemical physics letters, 2003. **376**(1-2): p. 141-147.
75. Shavitt, I., *The method of configuration interaction*, in *Methods of electronic structure theory*. 1977, Springer. p. 189-275.
76. Görling, A., *Density-functional theory beyond the Hohenberg-Kohn theorem.* Physical Review A, 1999. **59**(5): p. 3359.
77. Sahni, V. and V. Sahni, *The Hohenberg-Kohn theorems and kohn-sham density functional theory.* Quantal Density Functional Theory, 2004: p. 99-123.
78. Gilbert, T.L., *Hohenberg-Kohn theorem for nonlocal external potentials.* Physical Review B, 1975. **12**(6): p. 2111.
79. Kryachko, E.S., *On the original proof by reductio ad absurdum of the*

Hohenberg–Kohn theorem for many-electron Coulomb systems. International journal of quantum chemistry, 2005. **103**(6): p. 818-823.
80. Bylaska, E.J., M. Holst, and J.H. Weare, *Adaptive Finite Element Method for Solving the Exact Kohn− Sham Equation of Density Functional Theory.* Journal of Chemical Theory and Computation, 2009. **5**(4): p. 937-948.
81. Wesolowski, T.A. and J. Weber, *Kohn-Sham equations with constrained electron density: an iterative evaluation of the ground-state electron density of interacting molecules.* Chemical physics letters, 1996. **248**(1-2): p. 71-76.
82. King, R.A. and N.C. Handy, *Kinetic energy functionals from the Kohn–Sham potential.* Physical Chemistry Chemical Physics, 2000. **2**(22): p. 5049-5056.
83. Norman, M. and D. Koelling, *Towards a Kohn-Sham potential via the optimized effective-potential method.* Physical Review B, 1984. **30**(10): p. 5530.
84. Fuks, J.I., et al., *Time-dependent density functional theory beyond Kohn–Sham Slater determinants.* Physical Chemistry Chemical Physics, 2016. **18**(31): p. 20976-20985.
85. Hamel, S., et al., *Kohn–Sham orbitals and orbital energies: fictitious constructs but good approximations all the same.* Journal of electron spectroscopy and related phenomena, 2002. **123**(2-3): p. 345-363.
86. Schwerdtfeger, P., *The pseudopotential approximation in electronic structure theory.* ChemPhysChem, 2011. **12**(17): p. 3143-3155.
87. Rappe, A.M., et al., *Optimized pseudopotentials.* Physical Review B, 1990. **41**(2): p. 1227.
88. Franceschetti, A. and A. Zunger, *Direct pseudopotential calculation of exciton coulomb and exchange energies in semiconductor quantum dots.* Physical review letters, 1997. **78**(5): p. 915.
89. Briley, A., et al., *Vibrational frequencies and intensities of small molecules: All-electron, pseudopotential, and mixed-potential methodologies.* Physical Review B, 1998. **58**(4): p. 1786.
90. Dal Corso, A., *Pseudopotentials periodic table: From H to Pu.* Computational Materials Science, 2014. **95**: p. 337-350.
91. Teter, M., *Additional condition for transferability in pseudopotentials.* Physical Review B, 1993. **48**(8): p. 5031.
92. Louie, S.G., S. Froyen, and M.L. Cohen, *Nonlinear ionic pseudopotentials in spin-density-functional calculations.* Physical Review B, 1982. **26**(4): p. 1738.
93. Reis, C.L., J. Pacheco, and J.L. Martins, *First-principles norm-conserving pseudopotential with explicit incorporation of semicore states.* Physical Review B, 2003. **68**(15): p. 155111.
94. Cohen, M.L. and J.R. Chelikowsky, *Electronic structure and optical properties of semiconductors*. Vol. 75. 2012: Springer Science & Business Media.
95. Yabana, K. and G. Bertsch, *Time-dependent local-density approximation in real time.* Physical Review B, 1996. **54**(7): p. 4484.
96. Cioslowski, J. and K. Pernal, *Local-density-matrix approximation: Exact asymptotic results for a high-density homogeneous electron gas.* Physical Review B—Condensed Matter and Materials Physics, 2005. **71**(11): p. 113103.
97. Winkler, B., V. Milman, and M.C. Payne, *Ab initio total energy studies of minerals using density functional theory and the local density approximation.* Mineralogical Magazine, 1995. **59**(397): p. 589-596.
98. Zhao, G., D. Bagayoko, and T. Williams, *Local-density-approximation prediction of electronic properties of GaN, Si, C, and RuO 2.* Physical Review B, 1999. **60**(3): p. 1563.

99. Perdew, J.P., K. Burke, and M. Ernzerhof, *Generalized gradient approximation made simple.* Physical review letters, 1996. **77**(18): p. 3865.
100. Wu, Z. and R.E. Cohen, *More accurate generalized gradient approximation for solids.* Physical Review B—Condensed Matter and Materials Physics, 2006. **73**(23): p. 235116.
101. Simón, L. and J.M. Goodman, *How reliable are DFT transition structures? Comparison of GGA, hybrid-meta-GGA and meta-GGA functionals.* Organic & biomolecular chemistry, 2011. **9**(3): p. 689-700.
102. Peverati, R. and D.G. Truhlar, *Improving the accuracy of hybrid meta-GGA density functionals by range separation.* The Journal of Physical Chemistry Letters, 2011. **2**(21): p. 2810-2817.
103. Perdew, J.P., K. Burke, and M. Ernzerhof, *Perdew, burke, and ernzerhof reply.* Physical Review Letters, 1998. **80**(4): p. 891.
104. Ernzerhof, M., K. Burke, and J.P. Perdew, *Density functional theory, the exchange hole, and the molecular bond*, in *Theoretical and Computational Chemistry*. 1996, Elsevier. p. 207-238.
105. Ernzerhof, M. and G.E. Scuseria, *Assessment of the Perdew–Burke–Ernzerhof exchange-correlation functional.* The Journal of chemical physics, 1999. **110**(11): p. 5029-5036.
106. Fletcher, R., *Practical methods of optimization*. 2000: John Wiley & Sons.
107. Broyden, C.G., *The convergence of a class of double-rank minimization algorithms 1. general considerations.* IMA Journal of Applied Mathematics, 1970. **6**(1): p. 76-90.
108. Fletcher, R., *A new approach to variable metric algorithms.* The computer journal, 1970. **13**(3): p. 317-322.
109. Goldfarb, D., *A family of variable-metric methods derived by variational means.* Mathematics of computation, 1970. **24**(109): p. 23-26.
110. Shanno, D.F., *Conditioning of quasi-Newton methods for function minimization.* Mathematics of computation, 1970. **24**(111): p. 647-656.
111. Schnabel, R.B., *Conic methods for unconstrained minimization and tensor methods for nonlinear equations.* Mathematical Programming The State of the Art: Bonn 1982, 1983: p. 417-438.
112. Morales, J.L., *A numerical study of limited memory BFGS methods.* Applied Mathematics Letters, 2002. **15**(4): p. 481-487.
113. Dai, Y.-H., *Convergence properties of the BFGS algoritm.* SIAM Journal on Optimization, 2002. **13**(3): p. 693-701.
114. Merget, R. and G. Rosner, *Evaluation of the health risk of platinum group metals emitted from automotive catalytic converters.* Science of the Total Environment, 2001. **270**(1-3): p. 165-173.
115. Alia, S.M., B.S. Pivovar, and Y. Yan, *Platinum-coated copper nanowires with high activity for hydrogen oxidation reaction in base.* Journal of the American Chemical Society, 2013. **135**(36): p. 13473-13478.
116. Shviro, M., et al., *Bifunctional electrocatalysis on Pd-Ni core–shell nanoparticles for hydrogen oxidation reaction in alkaline medium.* Advanced Materials Interfaces, 2018. **5**(9): p. 1701666.
117. Narayanan, R., *Recent advances in noble metal nanocatalysts for Suzuki and Heck cross-coupling reactions.* Molecules, 2010. **15**(4): p. 2124-2138.
118. Hölzl, J. and F.K. Schulte, *Work function of metals.* Solid surface physics, 2006: p. 1-150.
119. Lin, L., et al., *Work function: Fundamentals, measurement, calculation,*

engineering, and applications. Physical Review Applied, 2023. **19**(3): p. 037001.
120. Deng, S. and V. Berry, *Wrinkled, rippled and crumpled graphene: an overview of formation mechanism, electronic properties, and applications.* Materials Today, 2016. **19**(4): p. 197-212.